INTEGRATED DIELECTRICS FOR PROTECTION AND GATING OF EPITAXIAL GRAPHENE DEVICES

A Dissertation
Presented to
The Academic Faculty

By

James Gigliotti Jr.

In Partial Fulfillment
of the Requirements for the Degree
Doctor of Philosophy in the
School of Materials Science and Engineering

Georgia Institute of Technology

December 2017

INTEGRATED DIELECTRICS FOR PROTECTION AND GATING OF EPITAXIAL GRAPHENE DEVICES

Approved by:

Dr. Walt de Heer
School of Physics
Georgia Institute of Technology

Dr. Eric Vogel
School of Materials Science and Engineering
Georgia Institute of Technology

Dr. Abdallah Ougazzaden
School of Electrical and Computer Engineering
Georgia Tech Lorraine

Dr. Mark D. Losego
School of Materials Science and Engineering
Georgia Institute of Technology

Dr. Faisal Alamgir
School of Materials Science and Engineering
Georgia Institute of Technology

Date Approved: October 23, 2017

Nothing has such power to broaden the mind as the ability to investigate systematically and truly all that comes under thy observation in life.

Marcus Aurelius

ACKNOWLEDGEMENTS

The work presented in this thesis is the culmination of years of research dating well before I joined the Epitaxial Graphene Lab. For this, I owe a great gratitude to the past members of the group who laid the tedious groundwork. Most notably, I would like to thank James Palmer and John Hankinson for their generous transfer of knowledge. James deserves special recognition for his extensive work developing the tooling which enabled much of my research.

For endless discussions, both related to graphene and everything else that has occurred in our lives over the last few years, Jean-Phillipe Turmaud, Dogukan Deniz, Yiran Hu, and Yue Hu will forever be friends. This work would never have gotten off the ground without your ideas and support.

Thank you, Claire Berger, for always standing by with a voice of reason and motivation.

I also must thank Abdallah Ougazzaden for opening his lab to me and sharing his group's expertise in epitaxial growth. In particular, Suresh Sundaram, Xin Li, and Renaud Puybaret deserve recognition for their insight and help, both while I was in France and from across the Atlantic.

Walt de Heer deserves a special thanks for his endless insights and creative vision that pushed this project off the ground and will continue to push into the future. In this game, small insights make all the difference, and his expansive knowledge and never tiring enthusiasm have ensured that avenues of great possibility are always available.

I would also like to thank the Materials Characterization Facility staff for their tireless efforts to support and push the boundaries of the capabilities offered on campus.

Finally, I need to thank my family and friends for maintaining my steadfast determination throughout my education and for always encouraging me to keep going. Your support has made this journey so much easier and more enjoyable!

TABLE OF CONTENTS

LIST OF TABLES

LIST OF FIGURES

SUMMARY

Epitaxial graphene is an exceptional platform for high performance carbon nanoelectronics and fundamental transport studies. Compared to exfoliated and CVD graphene, epitaxial graphene exhibits robust electronic transport and is best suited to wafer scale fabrication of high performance devices. However, due to its ultra-high crystalline quality, dielectric integration into epitaxial graphene systems is challenging. High-K metal oxides, such as Al_2O_3, have been widely investigated as a top gate; yet, despite innovative surface treatments and deposition techniques, current dielectric implementation reduces graphene transport performance and reliability. In this work, hexagonal boron nitride, a complementary 2D dielectric to graphene, is grown directly on epitaxial graphene surfaces via a novel lateral atomic deposition (LAD) technique for protection and gating. The hBN sp^2 hybridization and layered stacking are confirmed via HRTEM, XPS, and HRXRD. Selective growth of 2D hBN is observed on graphene surfaces, in contrast to traditional dielectric deposition techniques which exhibit significantly reduced film quality on graphene. Raman, LEED, and van der Pauw resistance measurements demonstrate good graphene properties after hBN deposition. A high speed LAD system is proposed.

CHAPTER 1
INTRODUCTION

For decades, the semiconductor industry has relied on the continual reduction in silicon feature size, known as Moore's Law, to advance computational capability. However, as silicon processing approaches single nanometer lengths, transistor performance no longer scales with channel length. Reducing channel length gives obvious performance benefits including faster operating speed and increased device density, but it also carries several caveats: unreliable ultra-thin dielectric layers, pronounced electromigration, increased leakage, reduced mobility, enormous thermal loads, and short channel effects. Short channel effects occur when the channel length is on the same length scale as the depletion-layer width and cause barrier lowering and punch through, surface scattering, velocity saturation, impact ionization, and hot electrons. To control short channel effects, the channel doping can be increased, but then mobility is reduced. It has become clear that silicon-based CMOS technology has intrinsic limitations which can only be overcome by a new material system which can accommodate higher operating frequencies, while supporting higher operating temperatures.

1.1 Electronic Transport

Electronic conduction in solids is classically described by the Drude model, which likens electronic transport to kinetic gas theory. In the presence of an electric field, E, an electron feels a force of $-qE$, where q is the electron charge. From $F = ma$, the velocity of an electron after a collision with random scattering direction is $v = -qEt/m$. By considering scattering time $t = \tau$, the drift velocity is shown to be

$$v_d = \frac{-qE\tau}{m}. \tag{1.1}$$

The current density, j, can be found by integrating the drift velocity, such that

$$j = \frac{nq^2\tau E}{m} = qn\mu E. \tag{1.2}$$

where n is the carrier density and the electron mobility, μ, is defined as

$$\mu = \frac{|v|}{E} = \frac{qE\tau}{mE} = \frac{q\tau}{m}. \tag{1.3}$$

Conductivity, σ, ($\sigma = 1/\rho$ where ρ is the resistivity) is then defined as

$$\sigma = nq\mu. \tag{1.4}$$

By considering the density of states, N, at the Fermi level, E_F, and the charge diffusivity, D, σ can be rewritten as

$$\sigma = q^2 N(E_F) D \tag{1.5}$$

which allows μ to be written as

$$\mu = \frac{ev_F\tau}{2\sqrt{\pi\hbar n}}, \tag{1.6}$$

allowing electron mobility to be related to charge density and scattering time. Further, Matthiessen's rule describes the mobility or scattering time as a sum of the contributing factors, such that

$$\frac{1}{\mu} = \frac{1}{\mu_{lattice}} + \frac{1}{\mu_{defects}} + \frac{1}{\mu_{impurities}} + \cdots. \tag{1.7}$$

The rule is limited in its quantitative application as it assumes that the factors are all independent, but it provides a sufficient description for the influence of many scattering sources on electronic transport, especially when considering the influence of adsorbed species and thin films.

While the Drude model describes metallic systems surprisingly well, it is suspected that more complex multi-particle interactions are required to describe the transport behavior

observed in graphene. Nonetheless, to a large degree, it will sufficiently describe transport phenomenon related to adsorbed species, amorphous dielectric over-layers, and epitaxial heterostructures. All of these interactions have a tendency to drastically reduce electronic transport in graphene devices.

1.2 Graphene

A leading candidate for future high frequency nanoelectronics is graphene [1]. Graphene is a two-dimensional carbon honeycomb lattice, as shown in Figure 1.1a, with ultra-high carrier mobility and Fermi velocity.[2] It also compares favorably to silicon for use in high temperature and harsh environments due to its exceptional thermal and chemical stability. Due to the high strength C-C sp^2 bonding, graphene is also immune to electromigration. Over the past decade, research has highlighted a breadth of synthesis methods and potential applications for graphene, as well as its use for fundamental transport studies, due to its unique linear band structure.

The noteworthy electronic transport properties of graphene are derived from the nearly linear bands that occur at the K and K' points in the Brillouin zone. The band structure of graphene, shown in Figure 1.1b, was derived by Wallace in 1947 with a simple tight binding model, yielding:

$$E(k) = \frac{\epsilon \pm tw(k_x, k_y)}{1 \pm sw(k_x, k_y)} \tag{1.8}$$

$$w(k_x, k_y) = \sqrt{1 + 4cos\left(\frac{\sqrt{3}k_x a}{2}\right) cos\left(\frac{k_y a}{2}\right) + 4cos^2\left(\frac{k_y a}{2}\right)} \tag{1.9}$$

where ϵ is the on-site energy, t is the π-bonding transfer integral, s is the overlap integral, a is the lattice parameter, and k_x and k_y are the momentum components [3]. These linear bands give rise to uniform density of states with increasing Fermi energy and photon-like dispersion near the K-point.

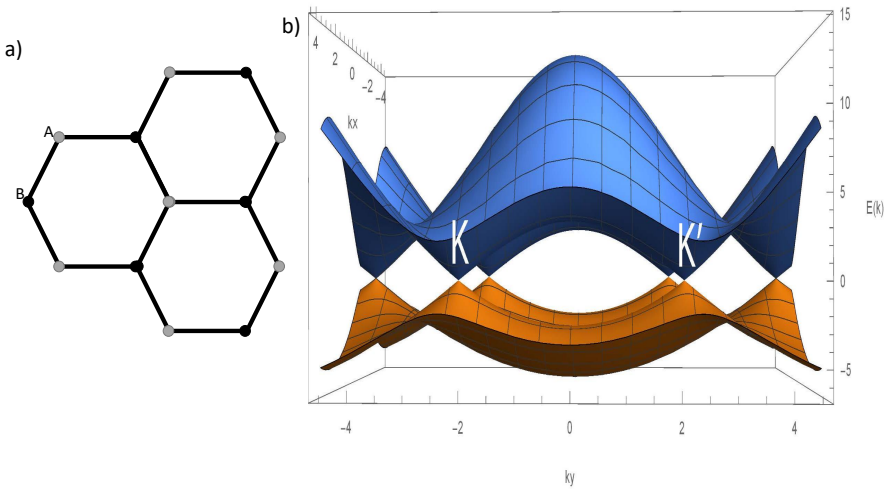

Figure 1.1: a) Graphene is a planar hexagonal carbon lattice with a basis of two carbon atoms, A and B. b) The band structure of graphene within the 1st Brillouin zone exhibits two Dirac cones at the K and K' points. Their linear intersection gives rise to the unique electronic transport properties of graphene.

1.2.1 Graphene Production Methods

Graphene production has been largely focused in four areas: mechanical exfoliation [4], chemical vapor deposition (CVD) [5, 6], reduced graphene oxide (rGO) [7], and epitaxial growth on hexagonal SiC [1]. Mechanical exfoliation of highly ordered pyrolytic graphite (HOPG) is not industry scalable and CVD on catalytic metal foils, to date, has not demonstrated necessary large scale transport properties for high performance nanoscale devices. Exfoliated graphene flakes are limited to a few micrometers in size and must be individually isolated prior to device fabrication. While CVD graphene can be produced at the wafer and panel scale, it must be transfered to an insulating substrate. This process introduces defects and contaminants [8], significantly reducing mobility. While the transport properties of CVD graphene are suitable for many low cost and flexible devices, high performance electronics demand a higher quality material. Reduced graphene oxide exhibits high defect concentrations and is ill-suited for nanoelectronic devices.[9]

Epitaxial graphene does not suffer from these problems. In 2004, epitaxial graphene,

produced via the known reorganization of the deconstructed SiC surface[10, 11], was demonstrated as an electronics material [1]. High quality epitaxial graphene has since been produced at the wafer scale [12, 13] and does not require transfer to an insulating substrate.[1] Further, SiC processing is a mature technology and is compatible with CMOS fabrication processes. Due to these advantages, epitaxial graphene devices are free from some of the challenges which plague exfoliated and CVD graphene, enabling devices with exceptional transport properties over unprecedented length scales. As such, epitaxial graphene is the leading graphene technology for high performance, high frequency electronics and will be the focus of this report.

Exceptional transport in epitaxial graphene is due to low defect densities and high quality nanostructures. Lithographically defined and plasma etched graphene devices exhibit reduced performance, likely due to etch damage of the graphene edges and surface contamination from resist residue. However, epitaxial graphene can self-assemble into nanoribbons on pre-patterned SiC, eliminating the need to directly pattern the graphene, preserving the pristine edge and surface quality.[14, 15] For this reason, and the observed exceptional ballistic conduction [15], much recent work has been focused on understanding graphene nanoribbon production and transport.

Over the past decade, epitaxial graphene devices have showcased the promise of graphene electronics. Large arrays of nanoribbon transistors were fabricated with a device density of 40,000 per cm^2 [14]. Wafer scale epitaxial graphene was demonstrated with arrays of field effect transistors (FETs) with f_{max} of 10 GHz for 240 nm gate lengths [12]. Ultra-high frequency transistors, exhibiting f_{max} of 70 GHz were produced on monolayer C-face graphene [16]. Ballistic conduction has been observed up to $16\,\mu\mathrm{m}$ and exhibits two length dependent carrier decay mechanisms [15]. This observation is key to understanding ballistic conduction in graphene and is currently undergoing much scrutiny. Spin transport has become an important area of study, following observation of spin diffusion lengths greater than $300\,\mu\mathrm{m}$[17]. Nanoselective area growth of GaN was achieved on SiC utilizing an epi-

taxial graphene mask [18] opening doors for integration into LEDs, photonic devices, and as a mask for patterned nanostructure growth.

1.2.2 Electronic Transport in Graphene

One striking disadvantage of graphene compared to silicon is the lack of band gap. All attempts to open a band gap in graphene are coupled to a distinct reduction in mobility.[19, 20, 21] Currently, instead of opening a band gap in the graphene, we are exploring alternative transistor architectures, such as tunneling field-effect transistors (TFET). Small gaps or nanoscale dielectric tunneling junctions between gated ballistic leads could be used to achieve digital functionality with graphene-based electronics [22]. Alternatively, other semiconducting 2D materials, such as the buffer layer, boron nitride, or transition metal dichalcogenides could be integrated into graphene circuits and gated. It is important to note that these novel devices all require integrated materials.

Graphene owes its photon-like electronic transport to the robust symmetry of the crystal, as described above. Unfortunately, freestanding graphene (not on a substrate), free of adsorbate and coatings is of little industrial interest. Devices require substrates to remove heat and integrate the device at the system level, dielectric and semiconducting materials to modulate the current, and films to provide environmental protection. All of these can sharply degrade electronic transport in graphene. As such, great efforts have been undertaken to preserve the unique electronic transport of graphene, and, in particular, the ballistic conduction observed in epitaxial graphene nanoribbons. Examples include vacuum wafer bonding[23], an exhaustive study of amorphous dielectric coatings, and transfered 2D materials. As will become clear, all past efforts have been unable to preserve graphene electronic transport, stalling further graphene study and impairing development of graphene-based industrial technologies.

Despite unique electronic transport and vast financial commitment, graphene has yet to be integrated into commercial electronics. This is partially due to exceptional chemi-

cal stability of graphene, which, while protecting the crystalline symmetry imperative to the transport phenomena, is a significant hurdle for the high quality dielectric interfaces necessary for reliable electronic devices. In order to be technologically relevant, FET gate materials must be sufficiently thin to modulate the density of states under moderate voltages, exhibit low leakage currents to reduce power demands and preserve signal integrity, and exhibit high quality interfaces to minimize scattering and protect the channel material from environmental contamination. Complicating this task is the fact that pristine graphene exhibits no dangling bonds and cannot easily be wetted by traditional semiconductor dielectric materials, such as high-K metal oxides, or metals. Dielectric layers that preserve graphene's high mobility, while being thin enough to function as a gate or tunneling barrier, are required for further graphene nanoelectronic development, as well as fundamental transport studies.

The conductivity, σ, of graphene can be describe as:

$$\sigma(n, n_K, T) = (\sigma_{pristine}(n)^{-1} + \rho_{ph}(T) + \rho_K(n, n_K, r_c(T))^{-1} \tag{1.10}$$

where $\sigma_{pristine}$ is the conductivity of a pristine graphene sheet with carrier density, n, ρ_{ph} is the resistivity due to phonon scattering at a given temperature, and ρ_K is the resistivity due to scattering of charged adsorbate atoms of density, n_K, r_c is the coherence length.[24]

A major contributer of adsorbate atoms is environmental contamination.[25] The immediate degradation in electronic transport upon exposure to air is demonstrated in Figure 1.2. Upon removal from the production furnace, the resistance of epitaxial graphene ribbons begins to increase in response to environmental contaminants [26, 27]. While the exact species have yet to be identified, water, oxygen, and organic molecules are likely candidates. These molecules, often polar, create charged scattering sites. While the performance drop is reversible upon vacuum annealing, there is an imperative need to protect the graphene in situ, before exposure to atmosphere. Similarly, non-stoichiometric amorphous oxide films, as is nearly always the case in very thin layers, also contribute scattering cen-

ters. It is then clear that films such as Al_2O_3 and HfO_2 are poor coating choices given the sensitivity of the electronic transport properties of graphene to adsorbed scattering centers and roughness.

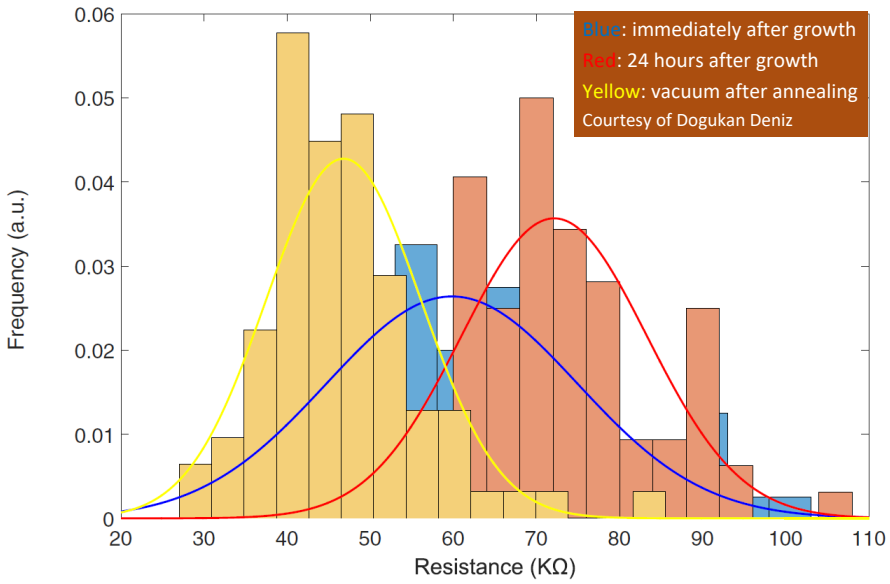

Figure 1.2: Environmental contamination causes degradation in graphene nanoribbon conductivity. The conductivity can be recovered through vacuum annealing. Data courtesy of Dogukan Deniz [28]

1.3 Thin-Film Nucleation and Growth

Thin films are layers of material ranging from a single atom (monolayer) up to a few micrometers thick. They are a major manufacturing technology to modify the mechanical, chemical, optical, and electronic properties of surfaces. In nanoelectronics, thin films have been implemented largely as dielectric layers, metal interconnects, and environmental protection. Over the past decade, the micromachined silicon surface, which was used as the channel material in transistors for logic applications, has been replaced with epitaxial strained silicon thin films. As silicon dimensions continue to fall, new material systems are being investigated which will demand highly controlled thin film growth.

For the sake of clarity, the following discussion will largely be based on a cubic, Kos-

sel crystal, as shown in Figure 1.3. While the crystal systems discussed in this thesis are hexagonal, there are no available accurate estimates for many of the associated energies. As such, the analytical results of the Kossel crystal will provide qualitative mechanism trends to guide experimental direction. Also labeled in Figure 1.3 are adatoms, mobile surface species, step adatoms, mobile species constrained to motion along a step edge, terrace atom, atoms defining the periodic surface potential, terrace vacancies, missing atoms in the surface terraces, kinks, bends in edges leading to half-crystal sites, and Ehrlich-Schwoebel (ES) barriers, energy barriers which must be overcome in order for adatoms to cross steps (2D) and kinks (1D). It is important to remember that these barriers are typically asymmetric, meaning the energy to climb a step is different than the energy required to descend a step.[29] The interactions and consequences of these features combine to describe film growth and surface reconstruction.

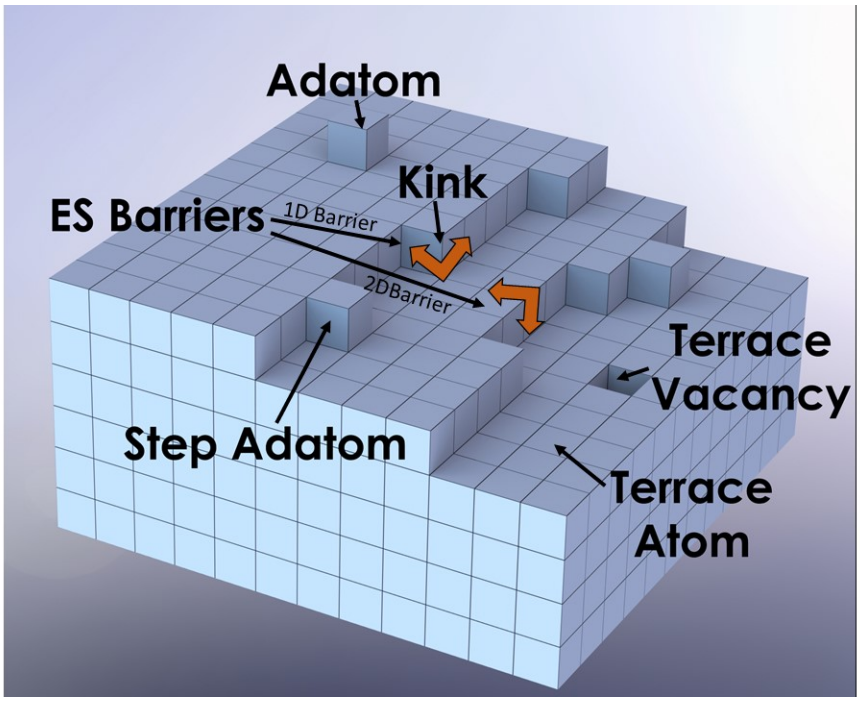

Figure 1.3: A Kossel crystal is a cubic model often used to qualitatively describe real-world crystal growth and rearrangement processes. Ehrlich-Schwoebel (ES) barriers are energy barriers which must be overcome for adatoms to cross steps and kinks.

Most thin film growth does not occur under thermodynamic equilibrium conditions. A

balance between the equilibrium energy minimum, related to the surface energies, temperature, and chemical bonding, and the kinetics, related to the flux and diffusion rate of the molecular or atomic species, determine how and if a thin film will grow.[29, 30, 31] In general, thin film growth occurs in three stages:

1. Removal particles from source material
2. Transport of particles to the substrate
3. Condensation of particles on the substrate

Each step must be carried out efficiently if reasonable growth rates are to be achieved.

Often the flux of particles from the source is modulated via temperature or plasma bombardment. Evaporators and most chemical vapor deposition (CVD) systems heat, or in the case of liquid precursors with high vapor pressures, chill, the source material to control the vapor pressure. Tight control over vapor pressure is critical to ensure reliable deposition processes. Alternatively, sputtering systems remove clusters of material from solid targets via plasma bombardment.

The liberated particles must then be transported to the substrate. In high vacuum conditions, such as in evaporators, line-of-sight deposition conditions occur. In CVD systems, a carrier gas is typically employed. The gas is often chosen to be inert, but reactive carriers can be used to aid in precursor decomposition or provide reactive species. If the particles are charged, a substrate bias can be applied to modulate the impingement energy and is often used to control film stress.

Once the particles impinge on the substrate, they must condense to form the film. The processes that occur on the surface will be discussed in detail in the following sections.

1.3.1 Transport of Particles on the Surface

When presented with a vapor, a surface will have an equilibrium concentration, n_s of adatoms on its surface defined by

$$n_s = n_0 e^{-W_s/kT}, \tag{1.11}$$

where W_s is the energy of evaporation, n_0 describes entropy, k is Boltzmann's constant, and T is temperature. The vapor can be of a foreign species or contain the same species as the substrate. There are then three processes which can occur on a surface:

1. Exchange between the vapor and adsorbed particles
2. Diffusion of adatoms across the surface
3. Diffusion of adatoms along edges

Burton, Cabrera, and Frank (BCF) developed a step flow growth theory relating the step-flow velocity to adatom desorption rates, adatom movement, and the diffusion of atoms over steps and kinks.[32] From this, the affect of the terrace width on step flow velocity (i.e. crystal growth) can be determined. Their model assumes a random walk of the adatoms, where an adatom can move a single atomic position per jump. Therefore, the mean travel of adatoms, x_s, can be described by a random walk model such that

$${x_s}^2 = D_s \tau_s, \tag{1.12}$$

where D_s is the diffusion coefficient and τ_s is the length of time an average particle spends on the surface before evaporating. For monatomic species the D_s and τ_s can be written as:

$$D_s = a^2 \nu' e^{-U_s/kT}, \tag{1.13}$$

$$1/\tau_s = \nu e^{-W_s/kt}, \tag{1.14}$$

where U_s is the energy required to jump between two neighboring surface sites, a is the distance between those sites, an ν is the frequency factor (10^{13} Hz for monatomic species). For monatomic species $\nu \approx \nu'$; however, in the case of complicated molecules, ν and ν' will differ. These relations serve as an upper bound on adatom mobility as molecular species are considered. Substituting back into Equation 1.12 and assuming simple molecules, it becomes clear that the necessary conditions for significant surface diffusion are $x_s > a$, which demands that $W_s > U_s$, as shown in

$$x_s = ae^{(W_s'-U_s)/2kT}. \tag{1.15}$$

Further, as temperature increases, the likelihood that an adsorbed species remains on the surface decreases, so x_s also decreases. In typical systems, Lennard-Jones forces lead to $x_s \approx 400a$ for close-packed surfaces at $\phi/kT \approx 4$, where ϕ is the nearest neighbor interaction. It is important to note that x_s has a strong dependency on the underlying crystal face. For a (100) face of a FCC crystal, $x_s \approx 3000a$.[32]

As an atom or molecule moves across a crystal, it must overcome various energy barriers related to the crystalline surfaces, kinks, and steps. The Terrace Step Kink (TSK) model was developed to describe how crystalline surfaces rearrange and defects form from a thermodynamic limit.[33, 34] As adatoms move across a crystal terrace, they experience a periodic potential, V, of

$$V(x,y) = \frac{1}{2}W_x(1 - 2cos(2\pi\frac{x}{a_x})) + \frac{1}{2}W_y(1 - cos(2\pi\frac{y}{a_y})) \tag{1.16}$$

where the amplitude of the potential well is $W = g\phi_d$. The desorption energy is represented by ϕ_d and g is a factor ranging from 1/30 for van der Waals interactions to 1/3 for covalent

bonding.[35] This amplitude, W, is also the activation energy for surface diffusion.

In 2D materials, such as sp^2 bonded graphene, there are no dangling surface bonds and very little roughness to serve as traps for adatoms. Therefore, the graphene sp^2 surface presents a significantly reduced interaction with adsorbed species, and thus, a much lower W_s and U_s compared to traditional systems. The activation energy to desorb saturated 5-6 member cyclic hydrocarbons from silicon is on order of 2.5 eV[36] compared to 0.5 eV for HOPG surfaces[37] .In fact, on graphene, adatoms will be much more mobile and the temperature dependence of adatom diffusion will be less severe.

1.3.2 Thin Film Nucleation

As adatoms diffuse on a substrate, the system rearranges to minimize its energy. For film growth to proceed, the first step is to create a stable nucleus. This occurs either via homogeneous, a thermodynamically stable structure on an infinite surface, or heterogeneous nucleation, where surface features reduce the energy barrier to nucleation.

First, whether 2D or 3D nucleation will occur is determined by a balance of supersaturation, $\Delta\mu$, strain ϵ, and surface energies. For square lattice, 2D nucleation is favored when

$$\sigma_s \geq \sigma + \sigma_i - \frac{\Delta\mu - n\epsilon}{2s_c}, \tag{1.17}$$

while 3D nucleation occurs when

$$\sigma_s < \sigma + \sigma_i - \frac{\Delta\mu - n\epsilon}{2s_c}, \tag{1.18}$$

where surface energies of the free substrate, free nucleus surface, and nucleus-substrate interface are σ_s, σ, and σ_i, respectively. The area of an atom in the atom is s_c. For a hexagonal lattice, the number of in-plane bonds, n, is three. Therefore, at moderate to high supersaturations, 3D nucleation is thermodynamically prohibited. In 2D crystals, such as graphene and BN, the surface and interfacial energies are small which will reduce the need

for high supersaturation to achieve 2D nucleation.[29, 30].

Homogeneous thin film nucleation is most readily explained by considering an atomically flat substrate, free of defects and step edges. A large, flat sheet of pristine graphene is a perfect example. If a single atom lands on the surface, it will come in thermal equilibrium with the substrate, but causes an increase in the surface energy. Naturally, in deposition systems, many atoms are impinging on a surface, so if they remain on the surface, these adatoms will collide and form a cluster of sufficient size to minimize their collective energy and form a nucleus for subsequent crystal growth. For a 2D system, such as occurs in a layer-by-layer growth mechanism, the free energy change, ΔG_{total}, can be described by

$$\Delta G_{total} = \pi r^2 \Delta G_v + 2\pi r\gamma, \tag{1.19}$$

where r is the radius of the cluster, δG_v is the volume free energy, and γ is the interfacial energy. This defines a critical nucleus size, $r*$, as

$$r* = -\frac{\gamma}{\Delta G_v}. \tag{1.20}$$

These relations are shown in Figure 1.4. It is important to note the temperature dependence of ΔG_v, as is described by

$$\Delta G_v = \frac{\Delta H_m \Delta T}{T_m}, \tag{1.21}$$

where ΔH_m is the latent heat of melting, T_m is the melting temperature, and $\Delta T = T_m - T$. As such, the temperature dependence of r^* is

$$r* = -\frac{\gamma T_m}{\Delta H_m (T_m - T)}, \tag{1.22}$$

which will cause r^* to increase with temperature. Therefore, nucleation can be reduced by increasing the temperature of the substrate, or increased by reducing the temperature.[29, 30]

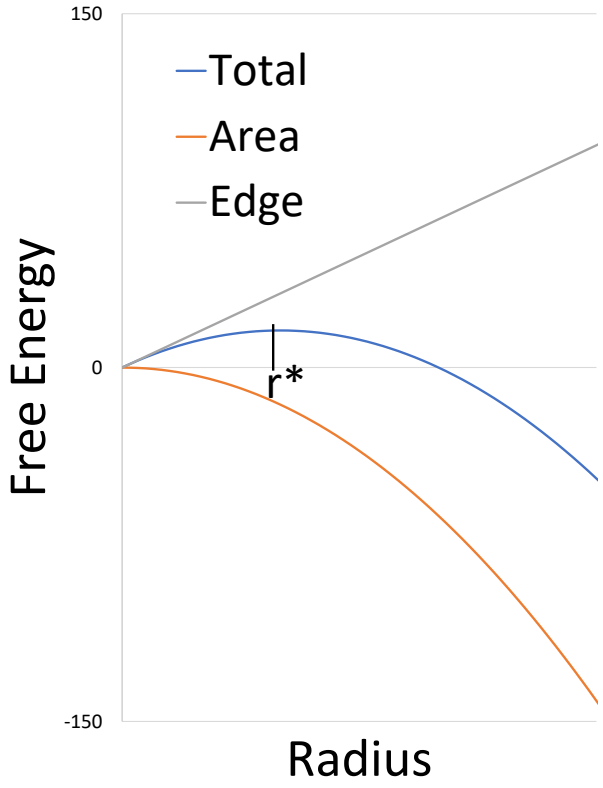

Figure 1.4: The balance between the interfacial surface free energy determined by the area of the nucleus and edge free energy give rise to a maximum in the total free energy which defines the critical nucleus size, r^*. Clusters smaller than this are unstable and will shrink, while clusters larger than r^* are thermodynamically stable and will grow.

As real substrates contain defects and atomic step edges, heterogeneous nucleation often occurs. At these preferential sites, the interfacial energy is reduced, thus lowering the nucleation barrier. In most thin film deposition systems, heterogeneous nucleation is dominant.

The kinetics of the system can also affect nucleation. If layer-by-layer growth is desired, nucleation on plateaus must be eliminated until the previous layer is complete. To ensure lateral growth, the temperature must be sufficiently high for adatoms on the top of the plateau to overcome the ES energy barrier to fall to the lower level. Also, homogeneous nucleation on the plateau must be eliminated. Therefore the flux of particles must be low enough that there is only ever a single particle on the plateau.[29] The density of free particles on the surface can be modulated by reducing the rate of impingement (ie. reduce partial pressure of source), by increasing the diffusion rate of the particles on the surface by increasing the substrate temperature, or by finding conditions which result in smaller plateaus with higher density.

1.3.3 Epitaxy

Thus far, the fundamentals of surface diffusion and thin film nucleation can be generalized to all types of film depositions. Epitaxy refers to a crystalline film grown on a crystalline substrate, such that the lattices exhibit a well-defined alignment. Nanoelectronics require epitaxial crystalline layers as the relative orientation of films has a strong affect on the electronic transport both at the surfaces and across the interface as exemplified by measuring the resistance while rotating graphene flakes on BN.[38] While amorphous films can act as a quasi neutral scattering source, if they exhibit pinholes, island morphologies, roughness, or non-uniform composition, scattering due to the dielectric layer can sevey impact device performance. In such systems, such as graphene, epitaxial dielectric layers are required.

Conditions for Epitaxy

In typical epitaxial processes, the lattice, both in terms of symmetry, lattice constant, and bonding character of the film and substrate must be similar. The structure of the substrate strongly influences the arrangement of the epilayer. If the lattices are well matched, stress buildup can be accommodated elastically and will relax over the first few layers without resorting to defects in the film. The mismatch, f, is defined by $f = (b-a)/a$, where a and b are the lattice parameter of the two materials. Typically, less than 15% percent difference is tolerated[39]; however, it is important to note that a supercell can be used as a lattice parameter and that crystals can rotate with respect to each other.[40] A good example is the graphene buffer layer in the epitaxial graphene system which exhibits approximately a $6\sqrt{3} \times 6\sqrt{3}R30^\circ$ reconstruction with respect to the SiC lattice.[41] As such, a more fitting condition is that the lowest energy configuration must present only a few percent mismatch.

Further, the coefficient of thermal expansion (CTE) of the two materials must be considered to prevent delamination or cracking of the epilayer. If materials exhibit large differences in CTE, large stress gradients will build during cooling, even if the lattices were well matched at growth temperature. For these reasons, homoepitaxial growth, where the epilayer is the same material as the substrate, is often a more straightforward process.

Heteroepitaxy involves dissimilar materials and can introduce defects at the interface which reduce electron mobility, optical efficiency, and carrier concentration. Common defects are screw dislocations, stacking faults, and dislocations due to dopants. As the film grows to a critical thickness, the stress will increase until the building strain causes a break in the dislocation.[30]

Epitaxial Interfaces

The interface between substrate and epilayer is determined by the lattices and chemical bonding. Mayer identified layered adatoms, periodically strained layers, homogeneously strained layers, interdiffusion layers, and distinct chemical compounds as possible inter-

faces as shown in Figure 1.5.[42] In the case of homogeneously strained layers, Frank and van der Merwe concluded a maximum allowable elastic strain of 14%, which is comparable to the result of Royer[39]. Again, it is convenient to look at the epitaxial graphene system. On the Si-face, the buffer layer is a periodically strained carbon layer between much less severely strained graphene and SiC layers. On the C-face, the graphene layers rotate by 30° with respect to the SiC lattice without a distinct buffer layer.[43]

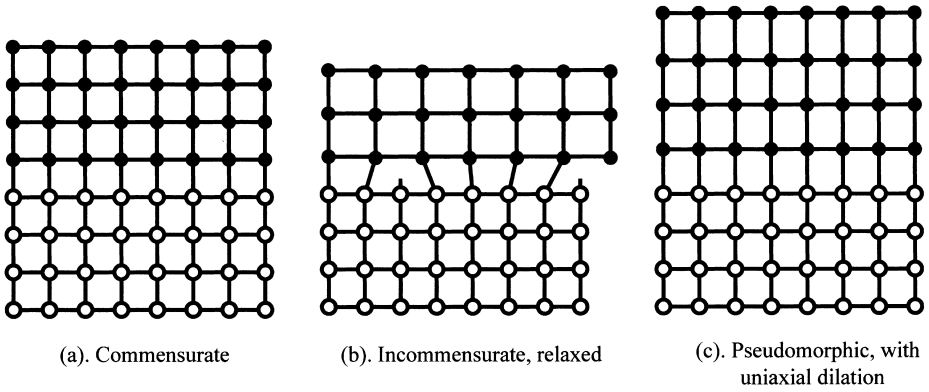

Figure 1.5: Epitaxy is a category of thin film growth in which the film lattice exhibits a preferred alignment with the substrate lattice. There are three common epitaxial interfaces: commensurate interface in which the film and substrate lattices align, incommensurate in which the interface layer is left with dangling bonds, or pseudomorphic in which a uniaxial strain accommodates the mismatch. Reprinted from [44]

For many traditional 3D systems, the misfit dislocation model is an adequate starting point to describe the epitaxial interface. In this model, film bonds are considered elastic and are subject to a periodic potential determined by the substrate. If the lattice spacing of the substrate is larger than the film, then the atoms at the substrate surface will be under compression, while the film atoms will be under tension. If the difference is too large to be accommodated elastically, dislocations are introduced. This affect can also be observed after some critical thickness in systems where a homogeneous strain produces a pseudomorphic overlayer. The stress builds linearly with thickness until a dislocation is introduced.[30]

In semiconductors, such as SiC, the anisotropic bonds lead to dislocations at the in-

terface.[45, 46] This is particularly important when designing electronic devices based on heterostructures as dangling bonds produced at the interface can create conducting energy bands in the gap, but is only important if the adhesion between the crystals is large.[47]

When considering a dielectric-graphene interface, the quality of the graphene can influence the ability to form an epitaxial overlayer. On a pristine graphene surface, there are no pinned nucleation sites, thereby enabling nuclei rotational freedom to find the lowest energy orientation and form epitaxial films. In such a system, the coincidence lattice model can be applied which treats the lattice of the substrate and the lattice of the film as rigid, as shown in Figure 1.6.[48] This is nearly the case in van der Waals solids due to the very weak interlayer interaction. Differing lattice constants are accommodated predominantly by rotation of the crystals to minimize free energy. In reality, pinned locations due to defects or graphene edges can limit the ability of van der Waals solids to accommodate large mismatches, particularly on the nanoscale.

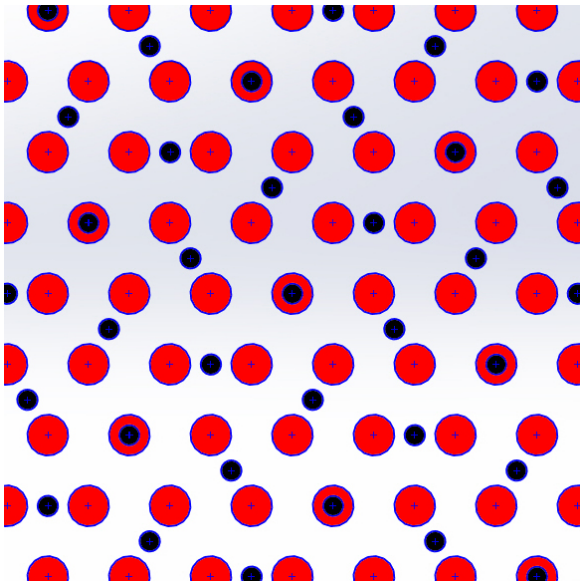

Figure 1.6: The coincidence lattice model describes systems where the epilayer (black circles) and substrate (red circles) lattices are considered rigid. Instead of accommodating the mismatch through strain, the crystals can rotate with respect to each other to minimize the free energy. This often occurs in van der Waals solids due to the very weak interlayer interactions.

A further benefit to the weak interaction of an epilayer on a graphene substrate is a very weak dependence of chemical potential, μ, with film thickness. In systems with strong adhesion, the interfacial layers exhibit differing bonding conditions than in the bulk crystal. This results in a thickness dependent chemical potential, described by

$$\mu(n) = \mu_{\text{inf}} + \frac{\phi_a - \phi'_a(1)}{n^3} \tag{1.23}$$

where n is the number of monolayers, ϕ_a represents the work to separate from a half-crystal position and the prime denotes the presence of a different substrate material. The theory is derived from the Lennard-Jones potential and satisfactorily describes the adsorption of noble gases onto graphite surfaces.[49] This variance in chemical potential can lead to varying growth conditions, such as the Stranski-Krastanov regime, to be discussed in the next section.[30] This is often an undesirable growth mode for nanoelectronics, but one that is hard to avoid. Fortunately, the weak interlayer interactions in 2D materials minimize this effect.

Epitaxial Growth

When adding molecules to a crystal edge, assuming the crystal is larger than r^*, the resulting free energy must be less than the free energy of molecule prior to filling a site on the edge if growth is to occur, as shown in Figure 1.7. The free energy of the crystal phase is lower than the mobile phase by Δh which represents the change in enthalpy due to the phase transition. The energy barrier, ΔU stems from preceding chemical reactions, such as the decomposition of precursors and the orientation rearrangement of complex molecules.

Thin film growth can be described by the relative strength of the interactions between the adatoms (or molecules) themselves and between the adatoms and substrate. Often, the interaction between the film and substrate can create gradients in the surface chemistry with film thickness, leading to a transition between the two primary growth mechanisms.

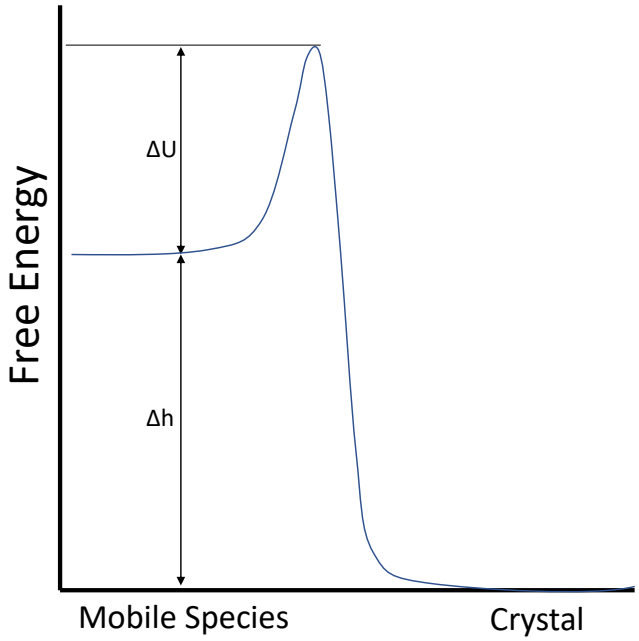

Figure 1.7: The free energy as a mobile species must be reduced as it becomes a stable part of the crystal edge. The enthalpy of solidification is Δh, while ΔU represents the barriers due to preceding precursor reactions.

In general, for film growth to occur, the free energy, G, must be decreasing towards the bulk value as layers build. Hence the chemical potential is defined by the slope of the free energy curve, such that

$$\mu = \frac{dG}{dn}, \tag{1.24}$$

and must always be negative if film growth is to occur. This has been shown to be an equivalent to wetting conditions described by balanced surface tension. Thus, there are three distinct free energy paths, as shown in Figure 1.8 which give rise to three growth regimes that are distinguished by the change in chemical potential, $d\mu/dn$.

In a practical sense, the chemical potential can be described by

$$\mu(n) = \mu_\infty + \phi_a - \phi'_a(n) + \epsilon_d(n) + \epsilon_e(n) \tag{1.25}$$

where μ_∞ is the bulk chemical potential, ϕ_a is the desorption energy of an adsorbate from

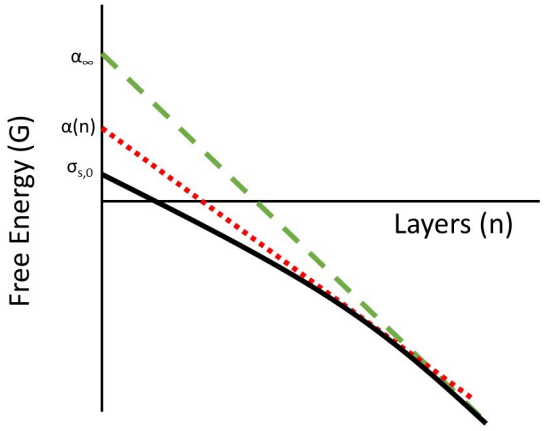

(a) Volmer-Webber $G(n)$ showing $d\mu/dn < 0$, which leads to immediate island formation.

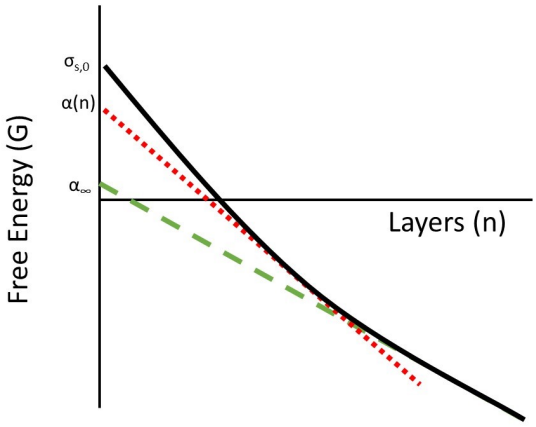

(b) Frank-van der Merwe growth is defined by $d\mu/dn > 0$. This condition demands that layers are completed prior to building a subsequent layer.

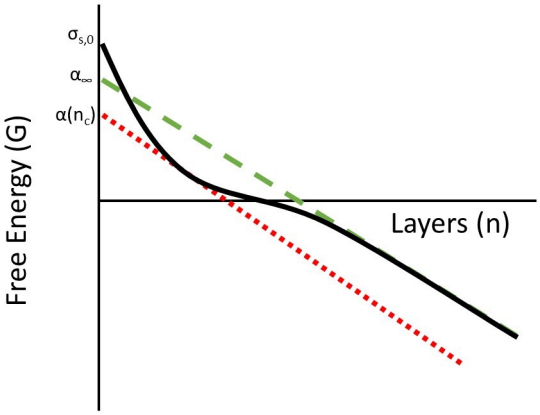

(c) Stranski-Krastanov G(n) showing an inflection point, corresponding to a critical thickness, n_c at which growth transitions from layer-by-layer to island formation.

Figure 1.8: The curvature of free energy of adsorbed atoms, G, as a function of monolayer, n defines the three possible growth regimes: Volmer-Webber (Fig. 1.8a), Frank-van der Merwe (Fig. 1.8b), and Stranski-Krastanov (Fig. 1.8c). The solid line is $G(n)$ which approaches the substrate surface energy, $\sigma_{s,0}$. The dashed line shows the asymptote to the bulk free energy of the over-layer, α_∞. The dotted line is a representative tangent at arbitrary n, and denotes the chemical potential, μ, of that layer.

the same material, ϕ_a' is the desorption energy of an adsorbate from the substrate, ϵ_d is the per atom misfit dislocation energy, and ϵ_e is the per atom homogeneous strain energy, and n is the film layer [30]. When considering small strains, thin film growth falls into several regimes, as shown in Figure 1.9 and are differentiated as:

1. Volmer-Weber Growth: island formation when adatom cohesion is greater than surface adhesion forces, such that $\frac{d\mu}{dn} < 0$

2. Frank-van der Merwe Growth: layer-by-layer growth when surface adhesion is greater than adatom adhesion, such that $\frac{d\mu}{dn} > 0$

3. Stranski-Krastanov Growth: layer plus island growth due to a shift in conditions

As growth proceeds and $G(n)$ approaches the bulk value, a_∞, growth will continue by the simultaneous growth of several monolayers.[50] As previously stated, 2D materials approach the bulk value within the first few monolayers, which may reduce uniformity in few nanometer thick 2D films. While these thermodynamic criteria for film growth modes were originally investigated with respect to epitaxial films, they were later applied to all film growth modes by Markov and Stoyanov.[51]

Nanoelectronics demand films with uniform thickness over large areas (one of the few examples where 3D growth is desired is for quantum dots).[29] This is most often achieved through deposition processes which fall into the layer-by-layer, Frank-van der Merwe, growth regime. Strong adhesion between the film and substrate enables a robust interface to delamination, environmental effects, and electronic transport.

Traditional silicon-based devices utilize amorphous oxide layers as they are free of grain boundaries and readily form robust films on the silicon surface (silicon oxide). This strong adhesion leads to high nucleation density, approaching a saturated monolayer in the case of a well designed ALD process. The self-limiting nature of the chemical reaction leads to a Frank-van der Merwe growth mechanism, enabling highly uniform, few nanometer thick films over large wafers. Further, high deposition rates favor layered growth

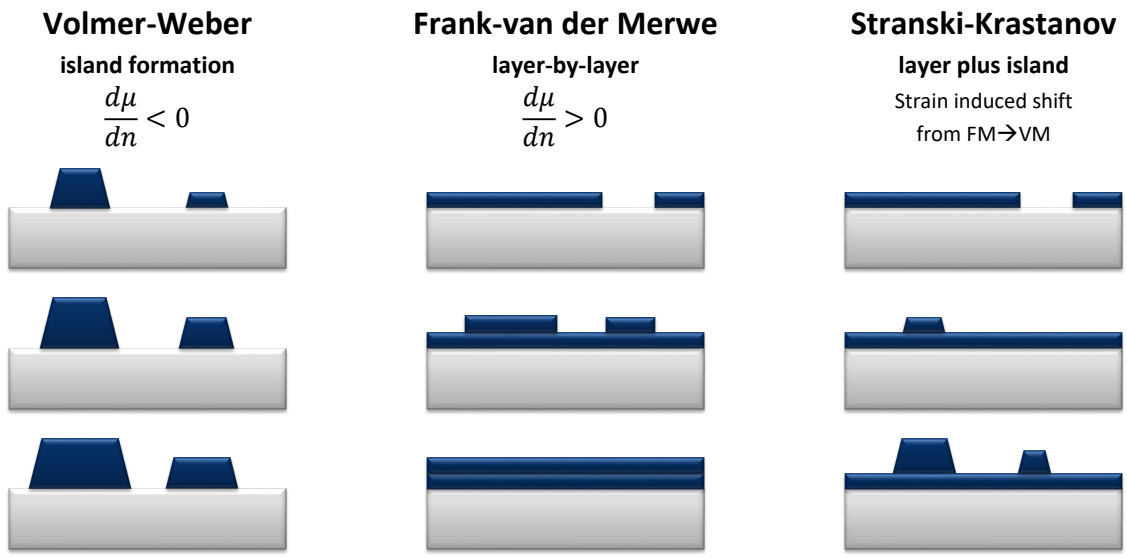

Figure 1.9: Thin-film growth transitions from Volmer-Weber growth to Frank-van der Merwe growth in response to the surface chemistry. Islands are formed when the adhesion within the film is larger than between the film and surface. When adhesion between the film and surface is larger, thin film growth proceeds in a layer-by-layer fashion. As the surface changes due to chemistry or induced strain, the growth mechanism may shift from a layer-by-layer mode to produce islands.

by limiting adatom mobility. This effect has been used in attempts to grow uniform metal films on graphene, to be discussed in the next section

When the adhesion between the film and substrate is very low, growth conditions favor the 3D island formation of the Volmer-Weber regime. Adatoms strongly adhere to one another, and in order to reduce the surface tension, bead up similar to water on a waxed car. Island dominated growth results in films with non-uniform thicknesses. In films up to a few nanometers thick, pinholes are often present. High substrate temperatures also favor island formation as the higher diffusivity enables adatoms to overcome the half crystal activation and move to produce the equilibrium crystal shape.[29, 30] In 2D materials, this is less of a concern as the thermodynamic drive to build vertically is reduced.

Kinetics of Epitaxial Growth

The above thermodynamic discussion determines the equilibrium growth conditions for thin films; however, typical deposition systems operate far from equilibrium. Two important factors that affect the kinetics of growth are substrate temperature and precursor flux (ie, the rate of deposition).

By considering the surface coverage of monolayer n, Θ_n, it can be shown that the rate of coverage the top monolayer, N, is

$$\frac{d\Theta_N}{d\theta} = \frac{M_{N-1} + \Theta_{N-1} - \Theta_N}{\ln \frac{\Theta_{N-1}}{\Theta_N}}, \tag{1.26}$$

where θ is a dimensionless time given by Rt/N_0, where R is the rate of arrival and t is time, and M_n is a strong function of temperature and inverse function of R such that

$$M_n = \frac{4\pi D_s N_s (n^e_{s,n} - n^e_{s,n-1})}{R}. \tag{1.27}$$

Therefore, smooth films can be formed by minimizing M_n under the random walk surface diffusion limit. This can be accomplished by reducing surface mobility by lowing the substrate temperature or by increasing the deposition rate to out compete surface diffusion.[30, 52] This approach has been employed by holding HOPG substrates at cryogenic temperatures during evaporation of metals.[53, 54, 55]

More recently, it has been observed in Au on HOPG that Levy flight can occur during deposition.[56] This allows for longer jumps, and as adatoms approach ballistic transport conditions, slows step velocity.[57] The velocity is dependent on β which varies between 1, corresponding to ballistic flight, to 2, which is the limit for classic random walk, such that

$$v = u_0 y_0 (1 + 2 \sum_{n=1}^{\infty} \frac{1}{q_n^{\beta} + 1}), \tag{1.28}$$

where $q_n = 2\pi n / y_0$, y_0 is the width of a terrace, and u_0 is related to the concentration of

adatoms on the terrace. In the case of ballistic flight, step velocities approaches zero as adatoms simply skip over the steps.[57] As such, for sp^2 systems, in order to avoid island nucleation at high temperatures, low precursor flux is expected to be critical. Also, substrate temperature should not be so high as growth will cease if pure Levy flight conditions are maintained.

Island formation can be overcome by raising the temperature and reducing the deposition rate, such that step flow dominates growth. At high temperatures, the adatom mobility and the critical nucleus size, as described in Equation 1.22, become larger. Thus, if the flux of adatoms is sufficiently low, the likelihood of the formation of a new nucleus on a terrace is low and the adatoms will find an edge of the previous monolayer and contribute to lateral growth. Additionally, for an adatom to traverse a step, the Ehrlich-Schwoebel energy barrier, shown in Figure 1.3 must be overcome.[58, 59] Naturally, at higher temperatures, the barrier is effectively reduced. This scenario will be discussed in detail in Chapter 4 and is the basis of Lateral Atomic Deposition technology for 2D heterostructure production.

1.3.4 Epitaxy in Graphene Systems

A necessary development if 2D materials are to become industrially relevant is the arbitrary stacking into vertical heterostructures. Despite large variances in lattice constant, 2D materials all exhibit weak van der Waals forces between the layers. Therefore, in van der Waals solids, the lattice mismatch requirements are significantly relaxed as the layers can slide over one another without inducing a large stress. Epitaxial layers have been demonstrated with over 50% lattice mismatch which gives much promise that these 2D materials can be arbitrarily stacked.

Metals deposited under UHV conditions on pristine graphite surface fall into the Volmer-Weber regime, yet can exhibit epitaxial growth due to weak interactions with the graphite surface. Wende, et al, demonstrated aluminum islands with (111) orientation on HOPG terraces, and that small islands retain atomic mobility, a testament to the weak bond strength

[60]. Two dimensional metal clusters show a maximum size of about 10-20 adatoms, after which, 3D growth is observed [61]. Gold deposited at room temperature on HOPG(0001) surfaces shows dendrite growth and exhibits epitaxial orientation between Au(111) and HOPG(0001) [62]. Gold deposition on HOPG was then studied at elevated temperatures, ranging from 100-350 °C. It was observed that at temperatures above 100 °C, gold transitions to faceted growth [63, 64]. Single crystal platelets, grown above 200 °C often exhibit dimensions on order of 100 nm [63].

Sample cleanliness is imperative to achieving epitaxial growth as the surface must be vacuum cleaned prior to metal deposition and is directly related to the break down of epitaxy at thicknesses exceeding 1 nm [65]. It may be possible to extend epitaxial regions by annealing at 600 °C, following work by Evans et al, where polycrystalline gold deposits were heated, resulting in large epitaxial gold grains [66]. However, well chosen surfactants can actually aid in epitaxy by modifying the surface energy. Examples include oxygen adsorbed Cu(001) during Fe film growth[67] and even extremely low concentrations of CO drastically affected Pt(111) growth[68].

These studies of Au and Al deposition on HOPG (0001) indicate that sufficient deposition control is available to explore the range of epitaxial growth on graphene structures.

1.4 Thesis Overview

This thesis will focus on methods to deposit reliable dielectric layers directly on epitaxial graphene structures for protection and gating. Despite over a decade of research on graphene-based electronics, only recently has the community directed significant effort into 2D semiconductors and insulators, which are essential for electronic components. Even fewer research groups are looking into direct deposition of 2D heterostructures. This work aims to develop the 2D analog of atomic layer deposition to enable controlled growth of vertical and horizontal heterostructures and open the door for novel devices based on in-plane composition gradients, and, therefore, induced static electric fields. Hexagonal boron

nitride, deposited directly onto epitaxial graphene structures, will serve as the test bed for this new technology, labeled lateral atomic deposition (LAD), but the technology is expected to carry-over to other material systems. This thesis is divided into three primary sections:

1. An overview of the state-of-the-art in epitaxial graphene on SiC production and characterization.

2. An exploration of traditional chemical vapor deposition techniques for the production of 2D heterostructures.

3. An introduction and proof-of-concept example for lateral atomic deposition technology. Further avenues of development will also be discussed.

CHAPTER 2

EPITAXIAL GRAPHENE PRODUCTION AND CHARACTERIZATION

2.1 Epitaxial Graphene Production

2.1.1 Silicon Carbide

Silicon carbide (SiC) is a refractory semiconductor. Selected properties of SiC are listed in Table 2.1 and are compared to silicon. SiC is commercially available in high quality single crystal wafers, up to 4" (120 mm). Larger, 150 mm wafers are available, but are not suited to MOSFETs due to the lower crystal quality. SiC compares favorably to Si for use as a high performance electronics substrate due to its lower dielectric constant which reduces parasitic capacitance, higher thermal conductivity which aids in removing heat from devices on the surface, and improved thermal and chemical stability.[69] SiC processing is a mature technology due to its prevalent use as a substrate for optoelectronics, most commonly, LEDs, and high power electronics.

Table 2.1: Properties of hexagonal 4H- and 6H-SiC compared to Si.

Property	Si	4H-SiC	6H-SiC
Crystal Structure	Diamond	Hexagonal	
Lattice Constants (Å)	5.431	3.073;10.053	3.081;15.12
Band Gap (eV)	1.12	3.23	3.05
Thermal Conductivity c-axis ($\mathrm{W}/(\mathrm{m\,K})$)	130	420	490
Coefficient of Thermal Expansion (10^{-6})	2.6	4-5	
Melting Point (°C)	1414	3103	
Dielectric Constant Static	11.7	9.7	
Dielectric Constant High Frequency	11.7	6.5	

SiC exists in many polytypes, the most common are β-SiC, with a cubic zinc blend crystal structure, and the hexagonal 4H-SiC and 6H-SiC, shown in Figure 2.1. In the work presented in this thesis, 4H- and 6H-SiC will be used due to the symmetry matching of

the (0001) polar faces with the hexagonal graphene lattice. The stacking order of 4H-SiC is ABCB..., while the stacking of 6H-SiC is ABCACB.... The bilayer step height is approximately 2.5 Å.

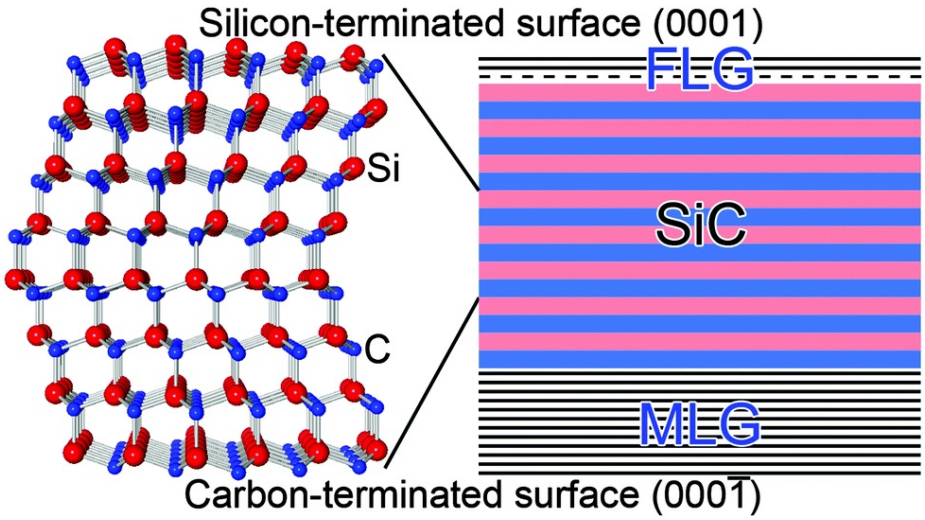

Figure 2.1: The crystal structure of 6H-SiC exhibits ABCACB stacking and has two polar faces, a silicon terminated face (0001) and carbon terminated face (000$\bar{1}$). Epitaxial graphene growth is unique to each face. On the Si-face, a buffer layer and only a few layers of graphene are possible. On the C-face, many layers of graphene can be produced. Reprinted from [70].

SiC can be doped to produce N-type, P-type, or semi-insulation wafers. Nitrogen doping produces N-type, while aluminum doping leads to P-type SiC. Insulating wafers, often doped with vanadium, were used in most of the experiments presented here.

2.1.2 Surface Graphitization

Due to the disparity in vapor pressures between silicon and carbon, silicon preferentially sublimates from the surface of SiC at high temperatures. While the vapor pressure of carbon is almost negligible, at typical growth temperatures (1400-1700 °C) the partial pressure due to the sublimation of silicon is on order of $10^{-3} - 10^{-4}$ Torr.[71] Epitaxial graphene self-assembles from the remaining carbon-rich surface. Three SiC bilayers must decompose to liberate enough carbon for one layer of graphene.

Originally, epitaxial graphene was grown under UHV conditions [72, 10, 1], but the rapid silicon flux leads to inhomogeneous growth and, often, a reduction in graphene quality. Confinement controlled sublimation (CCS) was developed in response and brings the growth into near equilibrium conditions resulting in improved uniformity, quality, and morphology control [73]. In CCS, the SiC substrate is placed in an enclosed graphite capsule with a small leak hole to manage the local Si partial pressure, as shown in Figure 2.2.

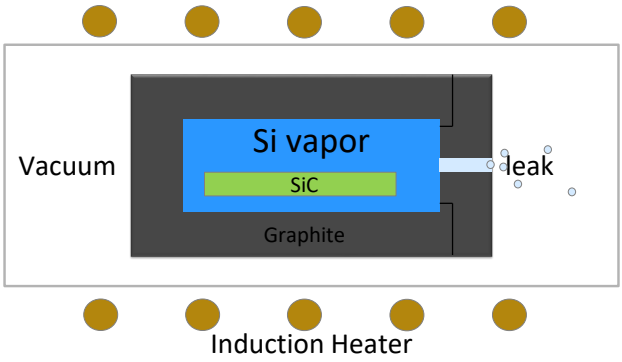

Figure 2.2: The confinement controlled sublimation (CCS) method for epitaxial graphene production brings growth into near equilibrium conditions.

The size of the leak hole and silicon content of the capsule walls are critical parameters to determine the resulting graphene morphology and process reliability. As previously discussed, if a net flux between surface species and the vapor is to occur, the system cannot be at equilibrium. For a net desorption, as is necessary to produce epitaxial graphene, the vapor must be under-saturated with respect to the surface. As the leak hole is opened, and then widened, the rate of graphitization increases as the driving force for Si desorption increases as the system moves further from equilibrium. For most CCS graphene growth processes such as for nanoribbons and monolayers, small leak rates are used to provide improved reliability and morphology control. Larger holes are required for multi-layer graphene. In a closed crucible with no leak hole, the Si partial pressure will rapidly reach equilibrium with the surface. As such, a closed crucible is pivotal for restructuring the surface, but will not facilitate graphene growth as the silicon partial pressure will reach

equilibrium. Another way to suppress graphitization is to hold the Si vapor on the surface by stacking substrates.

The Si partial pressure must also be in equilibrium with the graphite crucible walls. Therefore, pristine graphite crucibles lead to rapid graphitization and must be conditioned. When considering crucibles for graphene growth, several dummy SiC chips are run until processing conditions stabilize. If no graphitization is desired, a pure Si chip can be melted in the crucible to saturate the walls. This process will effectively prevent graphene growth for the lifetime of the crucible.

As growth crucibles age, the processing conditions will drift in response to the building Si liner, reducing graphitization. It is important to maintain a stable operating temperature and adjust the time if long-term stability is desired. If the temperature is increased to compensate, the equilibrium silicon conditions will change and the recipes will need to be recalibrate. This strategy enabled over 100 samples to be produced within tight tolerances for graphene coverage and nanoribbon width with near 100% yield.

The underlying SiC lattice has significant influence on the resulting graphene structure as the lattice spacing for graphene is 2.46 Å compared to 3.07 Å in hexagonal SiC. Growth temperatures between 1400-1800 °C for times ranging from a few seconds to several hours give rise to the various epitaxial graphene morphologies: buffer layer, graphene nanoribbons, monolayer graphene, and multilayer graphene. The various morphologies of epitaxial graphene, as shown in Figure 2.3, contribute to its broad applications and scientific interest.

2.1.3 Silicon-face Graphene Growth

On the Si-face (SiC(0001)), the strain is accommodated by the buffer layer, a $6\sqrt{3} \times 6\sqrt{3}R30^\circ$ reconstruction of the carbon-rich SiC(0001) surface, as shown in the LEED pattern in Figure 2.4. This layer is thought to exhibit a strong interaction with the substrate. The buffer layer has been shown to possess a semiconductor band structure [74]. The subsequent graphene layer, on top of the buffer layer, exhibits the iconic Dirac cone band

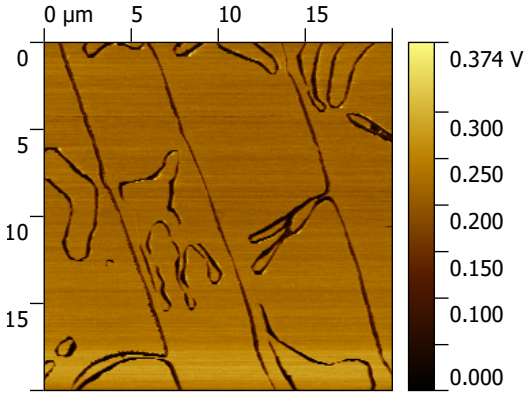

(a) Graphene nanoribbons

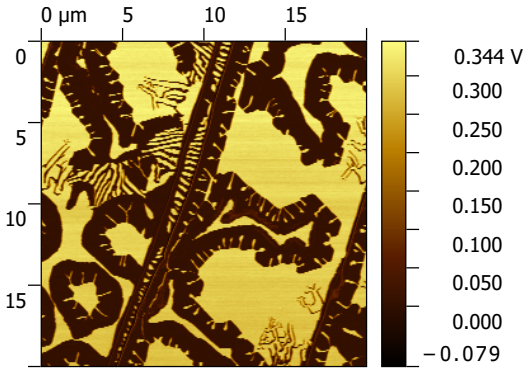

(b) Overgrown graphene nanoribbons

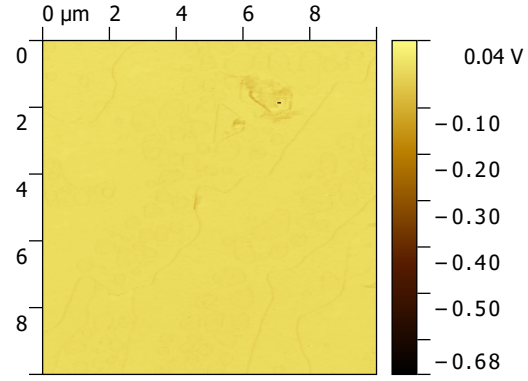

(c) Monolayer Si-face graphene

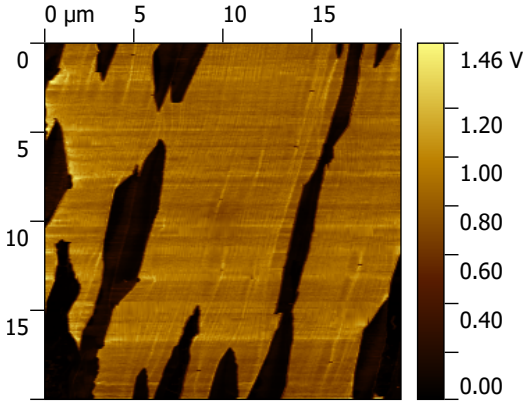

(d) Monolayer graphene domains on C-face.

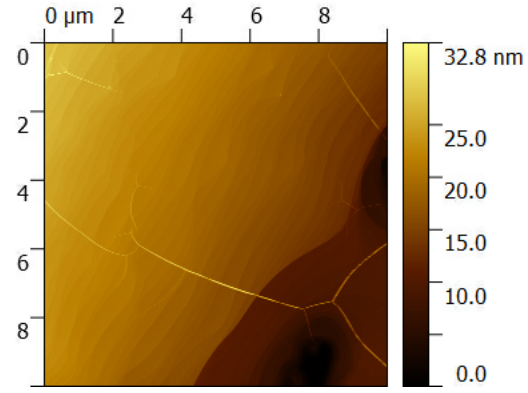

(e) Few layer C-face graphene

Figure 2.3: Surface morphology of epitaxial graphene system. Note that image scales and scan type vary to showcase the characteristic features: 2.3a-2.3d are LFM scans where areas of low friction ($V \approx 0$) indicate graphene coverage, 2.3e shows the pleated topography. The raised lines with three-fold symmetry are pleats due to biaxial stress induced during cooling.

structure. Silicon-face graphene of more than one layer (buffer layer + 2 graphene layers) results in AB stacking, breaking the out-of-plane symmetry and producing parabolic, gapped bands. Another method to produce monolayer graphene on the Si-face is by intercalating the buffer layer with H_2 [75]. This removes the strong interaction with the SiC substrate and produces quasi-freestanding graphene.

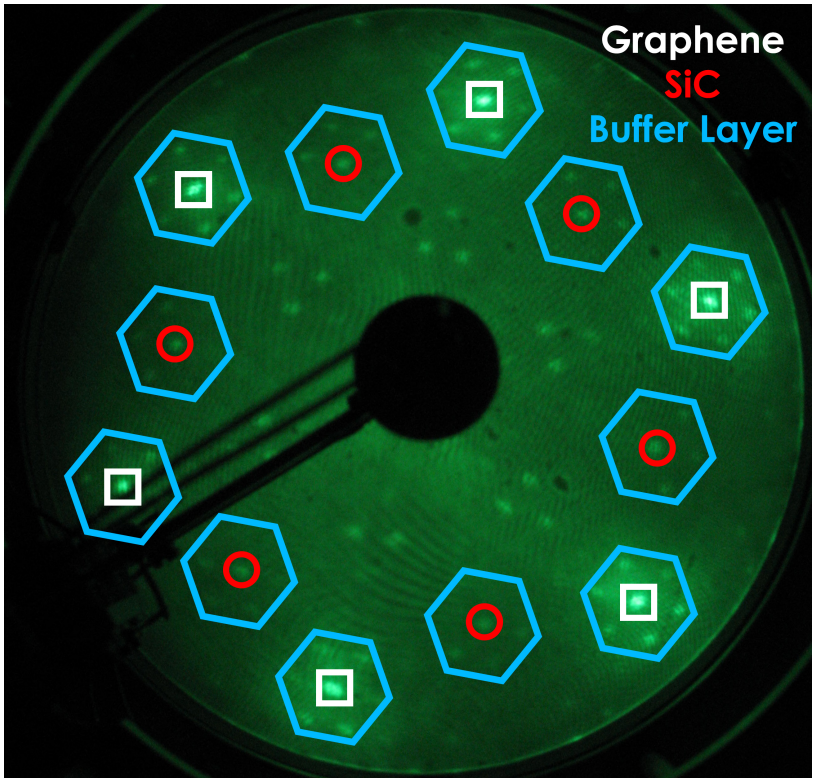

Figure 2.4: LEED pattern taken at 82 eV of Si-face graphene. The $6\sqrt{3} \times 6\sqrt{3}\ R30^\circ$ reconstruction, outlined by hexagons, is indicative of the buffer layer.

The Si-face (0001) terraces graphitize comparatively slowly and self-limit under reasonable conditions. It is difficult to growth more than a few layers, even under high temperature and UHV conditions. As such, crucibles designed for Si-face graphene typically have a small hole to improve precise control of graphene domain size, namely of graphene nanoribbons and to target large area monolayer graphene growth, as seen in Figure 2.3c.

As any miscut of the SiC wafer leads to surface steps, higher order facets are always present, especially after annealing due to step bunching. Due to the higher number of dan-

gling bonds (higher surface energy), these facets graphitize much faster than the SiC(0001) terraces and enable the controlled growth of self-assembled graphene nanoribbons, separated by buffer layer terraces, as shown in Figures 2.3a and 2.3b. The width of the ribbons can be controlled by the annealing time, temperature, and step height. Steps are most often produced by lithographically pre-structuring the SiC surface with arrays of trenches. Since etch depth of SiC is readily controlled down to sub-nanometer levels, access to narrow ribbons is possible without resorting to expensive nanolithography methods such as e-beam lithography, scanning probe lithography methods, or multiple exposure optical systems. Alternatively, SiC steps can be formed during step-flow by annealing which leaves atomically smooth terrace surfaces.

Cross-sectional TEM has shown that nanoribbons drape over the SiC step with larger spacing between the graphene layer and SiC surface than on the terraces [76], which contributes to their charge neutrality. As such, these ribbons have been shown to exhibit transport properties such as ballistic transport over exceptional lengths [15].

2.1.4 Carbon-face Graphene Growth

In contrast, on the C-face (SiC$(000\bar{1})$), graphene layers exhibit a slight in-plane rotation and pleated morphology to produce quasi-freestanding graphene regardless of the thickness [77]. Multilayer C-face graphene has been grown to thicknesses of over 100 layers with single layer mobilities of 40,000's cm^{-2}/V·s and up to several 100,000 cm^{-2}/V·s for the neutral layers in the multilayer epitaxial graphene stack.

The C-face graphitizes rapidly, so nanostructures are difficult to produce. Whereas Si-face graphene grows from step edges to produce ribbons, C-face graphene grows in isolated patches. On the C-face, growth is much faster perpendicular to the step edge and propagates along the step direction from a single nucleation site. Monolayer patches are achievable by limiting Si flux and short growth times, as seen in Figure 2.3d. If multilayer films are desired, as shown in Figure 2.3e, large leak holes and multi-cycle processing can

be required to maintain useful growth rates. The growth rate decreases as each layer is produced due to buildup of Si in the crucible wall. Therefore, reconditioning the crucible, most often by an empty annealing, resets the state and enables further graphititzation.

A cyclic method, described in Table 2.2, was developed to produce graphene films in excess of 100 layers with excellent quality, as shown in Figure 2.5. Each growth cycle consisted of a crucible reconditioning and growth cycle. The bulk structure of the film (46JG04) was probed with Raman spectroscopy and showed no change in FWHM or symmetry of the 2D peak or development of a large D-peak, which is indicative of defects, as shown in Figure 2.5a. The single Lorentzian 2D peak confirms that multilayer graphene, not graphite was produced. The surface structure was examined with LEED and, even after 5 growth cycles, graphene diffraction spots and the characteristic rotation are clearly visible, as seen in Figure 2.5b.

Table 2.2: Cyclic growth recipe for thick C-face graphene. Each cycle produced about 20 layers of multi-layer graphene. A 1 mm leak hole was used and temperature ramping was controlled by the PID (15/2/0).

Crucible Reconditioning	
800 °C	600 s
1200 °C	1200 s
1400 °C	1200 s
1600 °C	2400 s
Growth Cycle	
800 °C	600 s
1150 °C	1200 s
1600 °C	2400 s

2.1.5 SiC Surface Reconstruction

Pre-treatment of the SiC is an important step in determining the quality and morphology of the graphene and falls largely into two categories: thermodynamically driven self-assembled surface modifications[78] and nanofabrication processing, such as lithography and etching. In the first case, SiC wafers cut on-axis typically have an actual miscut of a

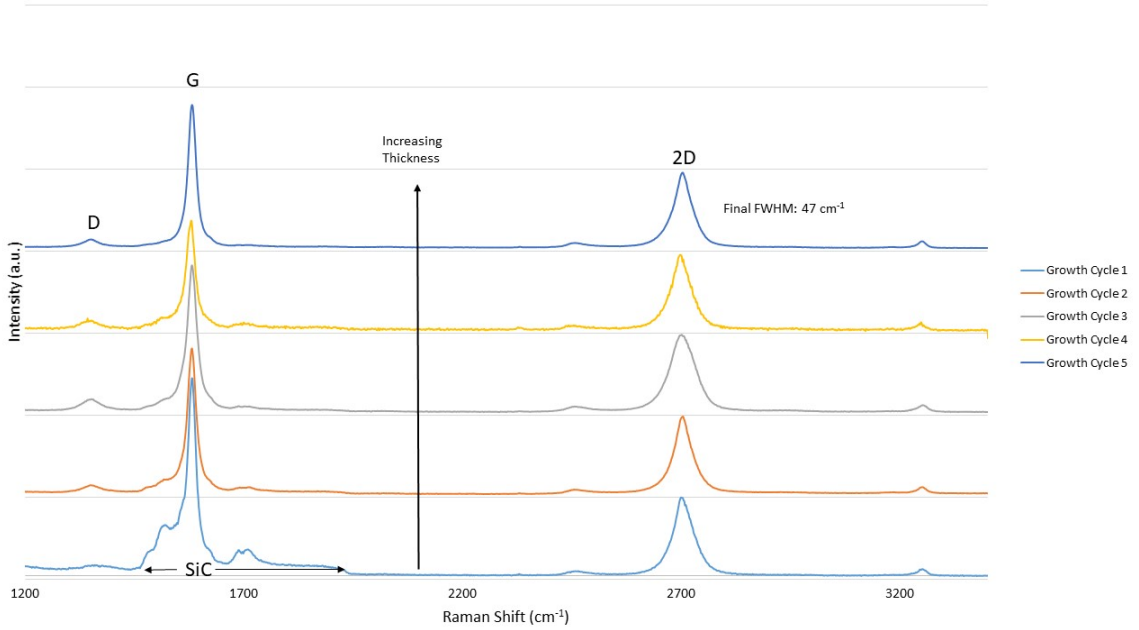

(a) The Raman spectra, taken after each growth cycle of 100 layer grahene film confirms the high quality of the graphene film. The Lorentzian symmetry of the 2D peak confirms that multi-layer graphene, not graphite was produced. Each cycle contributed about 20 layers of graphene, as was determined by ellipsometry. Minimal change in the FWHM of the 2D peak (47 cm^{-1}) is observed. No significant D peak developed, confirming that the graphene retained its structural integrity throughout the growth process.

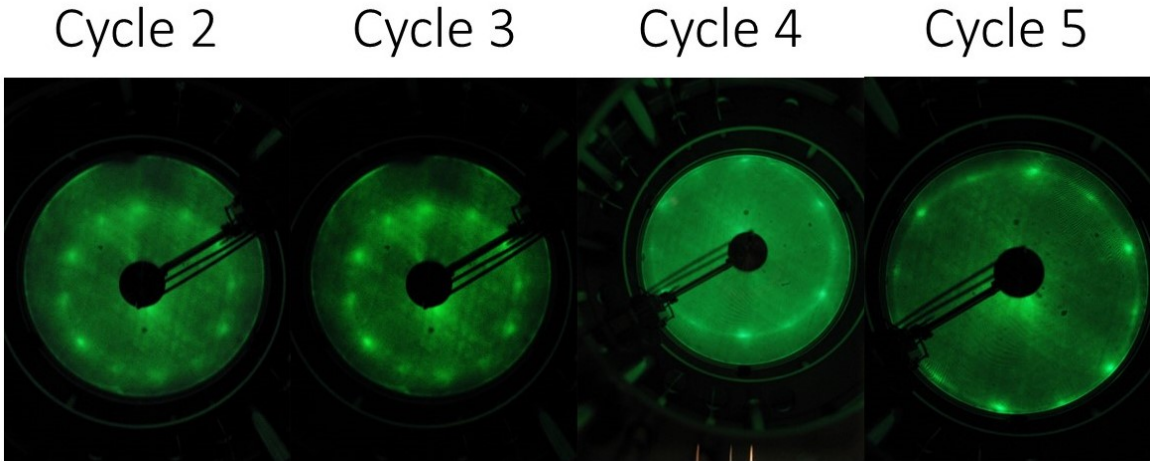

(b) The surface retains a sharp LEED pattern throughout the growth process. The arc connecting the graphene spots is indicative of C-face graphene due to the rotation between adjacent layers. As the penetration depth of the low energy electrons is only a few atomic layers, the underlying SiC is not visible. The patterns were obtained at different energies to maximize the clarity.

Figure 2.5: The development of the Raman spectrum and surface diffraction throughout the cyclic growth of a 100 layer thick C-face graphene film.

few hundredths of a degree leading to bilayer surface steps with terraces on the order of 100 nm, as shown in Figure 2.6a]. after chemical mechanical polishing (CMP). At high temperatures, the steps flow and coalesce into higher steps, up to tens nm, with large, atomically flat terraces, up to 100s μm in width, as shown in Figure 2.6b.

In order to suppress graphitization during this heating, SiC chips can be annealed in a face-to-face configuration [79]. This enables temperatures up to 2000 °C without significant silicon sublimation, while significantly improving step step flow. The face-to-face method is particularly useful for producing graphene nanoribbons and can eliminate the need for traditional nanofabrication techniques. However, when precise arrays of devices or complex geometries are required, structures must be lithographically defined and etched.

Figure 2.6 and 2.3 show AFM images of the morphology of these distinct graphene structures. Lateral force microscopy is particularly helpful to identify graphene regions on partially graphitized surfaces. The interaction between the graphene surface and the scanning probe tip are very low compared to the SiC and buffer layer surfaces which gives rise to the contrast.

2.2 Amorphous Dielectrics for Graphene Electronics

Most electronic devices require dielectric films and elements to passivate the surface and modulate the electronic transport. Whereas silicon readily forms a reliable, high quality interface with amorphous metal oxide dielectrics, graphene is highly inert and does not support direct oxide formation. Over the past half century, deposition and coating techniques have been widely explored to deposit metals and metal oxides on graphene, graphite, and carbon nanotube surfaces to form graphite-alumina composites and electrically insulate the carbon material, but all have resulted in poor interface reliability or have impaired electrical performance [80, 66, 81, 82, 83].

Most graphene dielectric research has focused on amorphous Al_2O_3 due to its high dielectric constant, good temperature and chemical stability, and readily available wet chem-

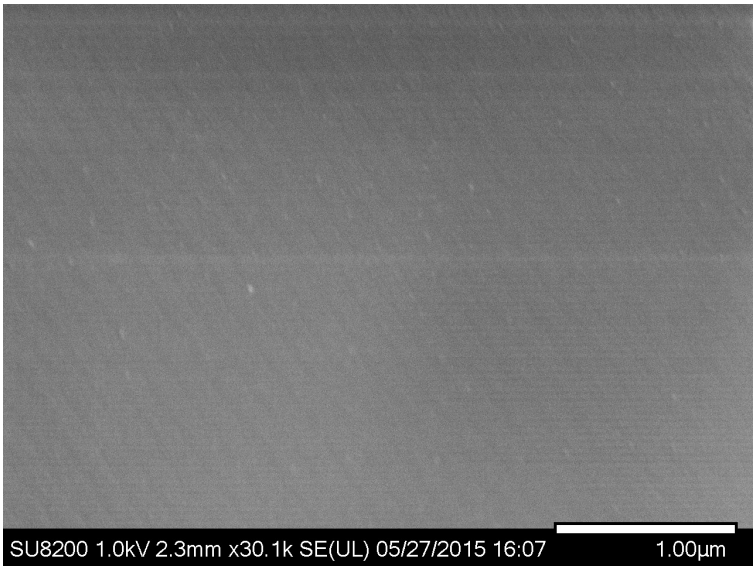

(a) CMP SiC surface

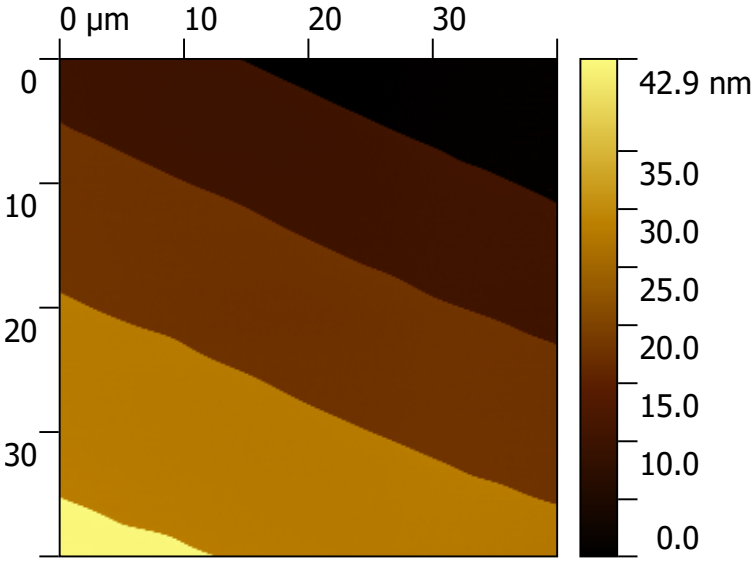

(b) SiC terraces after face-to-face annealing

Figure 2.6: The initial surface of the SiC plays a critical role in determining the graphene morphology and stability of nanostructures. 2.6a) CMP SiC surface with a slight miscut off (0001) produces terraces on the order of 100 nm in width with bilayer steps. 2.6b) After face-to-face annealing, steps flow and coalesce into large steps of a few nm and terraces up to 100 μm in width.

istry and plasma-based processing techniques. (Although, it should be noted that aluminum is a carbide former at high temperatures.) Despite these advantages, it is difficult to form a uniform, thin layer of metal oxides on the graphene surface as the growth lies well within the Volmer-Webber regime leading to island formation [54, 60]. As outlined in Figure 2.7, these islands invariably form incomplete films and interface layers with pinholes, charge puddles, and high, variable leakage currents, especially as film thicknesses are reduced to the few nanometer thickness regime. Pinholes are especially detrimental in tunneling barriers where high electric fields lead to electromigration of metal contacts which can cause shorting.

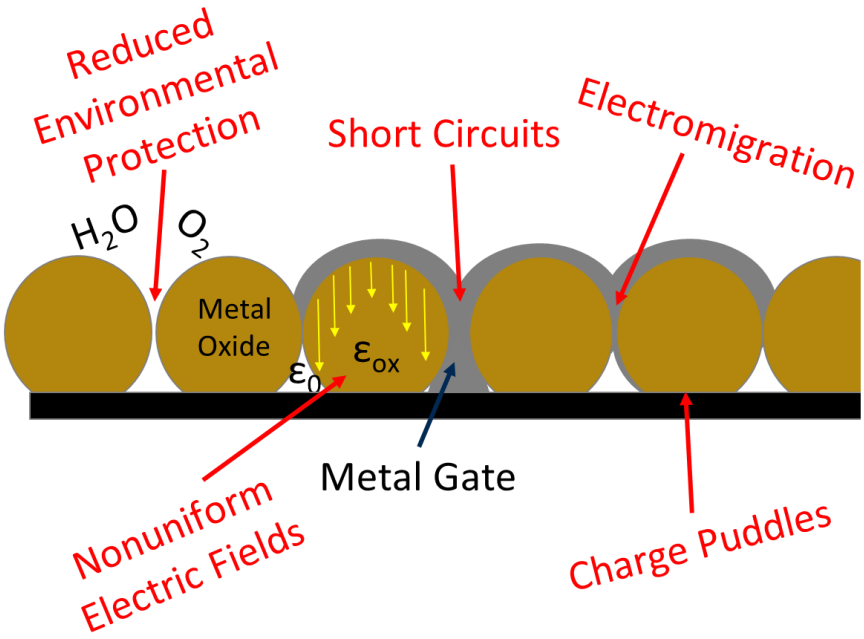

Figure 2.7: Thin amorphous dielectric layers introduce many unintended challenges. On the non-wetting graphene surface, these oxides tend to ball up, resulting in pinholes, charge puddles, and high leakage currents. This morphology does not sufficiently protect graphene from environmental contamination and enables electromigration of top metal electrodes. Further, the non-uniform thickness and stoichiometry result in non-uniform electric fields, even over short distances.

To counter island formation, various surface treatments, deposition techniques, and deposition parameters have been explored to bring the growth into the Frank-van der Merwe regime. All either result in island formation[84, 85, 86] or functionalize[84, 87, 88] the

graphene surface leading to irrecoverable loss in electronic transport performance. Magnetron sputtering damages the first few layers of graphene due to the high energy surface collisions [83, 89]. Evaporated films invariably form islands, unless deposited at cryogenic temperatures ($<$ 200 K), but often still form islands once brought to room temperature [54, 53, 60]. Atomic layer deposition (ALD), which has become the standard for semiconductor dielectric deposition, often relies on a hydrophilic surface to nucleate. Surface functionalization with NO_2 [90] or ozone [91] improved graphene coverage, but degrade graphene performance and have since been largely abandoned. Other attempts have taken advantage of polar traps within the graphene, induced by the underlying metallic layer, to improve graphene wetting, although this technique is not compatible with epitaxial graphene on SiC [85]. Evaporated seed layers ($<$1 nm) of Al have been widely applied, but still do not yield high quality films on graphene surfaces due to island formation of the seed layer, as shown in Figure 2.8 [16, 92]. Thin organic layers have also been applied as a seed layer for ALD processes with encouraging results, but limit the thermal stability of the system [93].

Other dielectric materials, including HfO_2[8, 94] and SiN[95] have also been used. Both modify the graphene carrier density. The plasma SiN process also damaged the graphene giving further justification to avoid plasma processes for depositions on graphene. As graphene exhibits very low adhesion forces to adsorbates, changes in composition of the dielectric are unlikely to drastically improve uniformity or performance. These results make it clear that amorphous dielectric layers, regardless of chemical composition or deposition method, are ill suited for graphene devices.

Decades of research has demonstrated that films grown on high quality HOPG surfaces, similar to graphene, are only adhered by van der Waals interactions.[60, 61, 62, 63, 66] For this reason, as well as the extensive history of challenges that have faced metal oxide growth on graphene, it is clear that materials which exhibit more compatible bonding to graphene, such as the 2D semiconductors, are necessary to facilitate further development in graphene-based nanoelectronics.

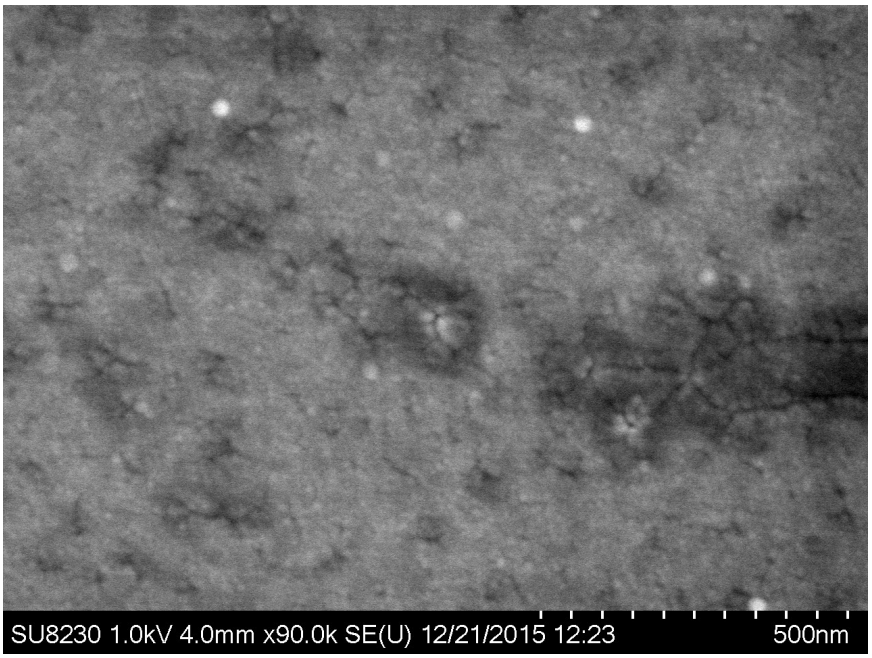

(a) 20 nm of ALD Al_2O_3 on monolayer epitaxial graphene exhibiting non-uniform coverage and grain boundaries.

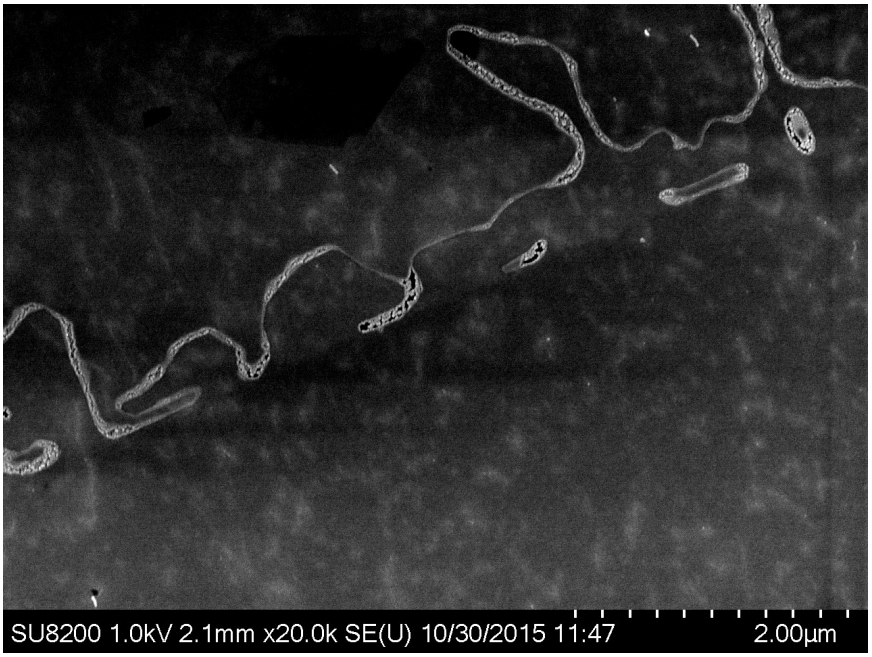

(b) 20 nm of ALD Al_2O_3 on monolayer graphene nanoribbons does not ensure coverage of the graphene surfaces.

Figure 2.8: Despite the implementation of evaporated seed layers, ALD of metal oxides, such as Al_2O_3, does not produce high quality dielectric films on graphene surfaces.

CHAPTER 3
GRAPHENE HETEROSTRUCTURE PRODUCTION

3.1 2D Heterostructures

The electronic transport of nanomaterials is strongly influenced by the local environment[8, 96], lattice orientation[97, 38, 98, 99, 96], and interface quality[96, 100]. In 2D material systems, the impact of poorly designed layered structures is especially important due to symmetry breaking and reliance on in-plane charge transport and momentum matching.[97, 98] This is particularly true when considering stacked 3D and 2D materials due to the out-of-plane symmetry of the 3D lattice. Fortunately, 2D conductors (graphene), semiconductors (transition metal dichalcogenides), and insulators (boron nitride) have been synthesized and promise to enable arbitrary stacking while reducing undesired impact on charge transport due to the weak interlayer interaction. Due to this, 2D heterostructures have attracted much attention.

Epitaxy between critical layers is essential if high performance graphene-based nanoelectronics are to be produced.[97, 101, 38, 98, 99] The tunneling current between MoS_2 and WSe_2 sheets with a 5° rotational misalignment was modeled and showed an order of magnitude drop compared to aligned lattices due to the misaligned K-points.[98] This is one area where the epitaxial graphene system shows a significant advantage over CVD graphene: the graphene-Si-face SiC interface is inherently pristine and epitaxial. SiC wafers are also available in a wide range of conductivities, so the graphene film does not need to be transfered to an insulating substrate.

Nonetheless, most graphene work has been focused on CVD methods due to the low cost and large area production. However, these graphene films are often polycrystalline and must be transfered onto insulating substrates leading to reduced device performance

due to randomly oriented graphene domains, rotationally misaligned layers, and impurities at the interface. Figure 3.1 shows the improved graphene performance of hBN supported graphene compared to SiO_2 and the further improvement by ensuring a clean interface by growing graphene directly on hBN.[100] Epitaxial graphene does not need to be transfered and can be patterned without inducing interfacial defects or impurities. However, this benefit disallows the ability to back-gate the graphene to modulate electronic transport. Therefore, a directly deposited top gate is required for epitaxial graphene devices.

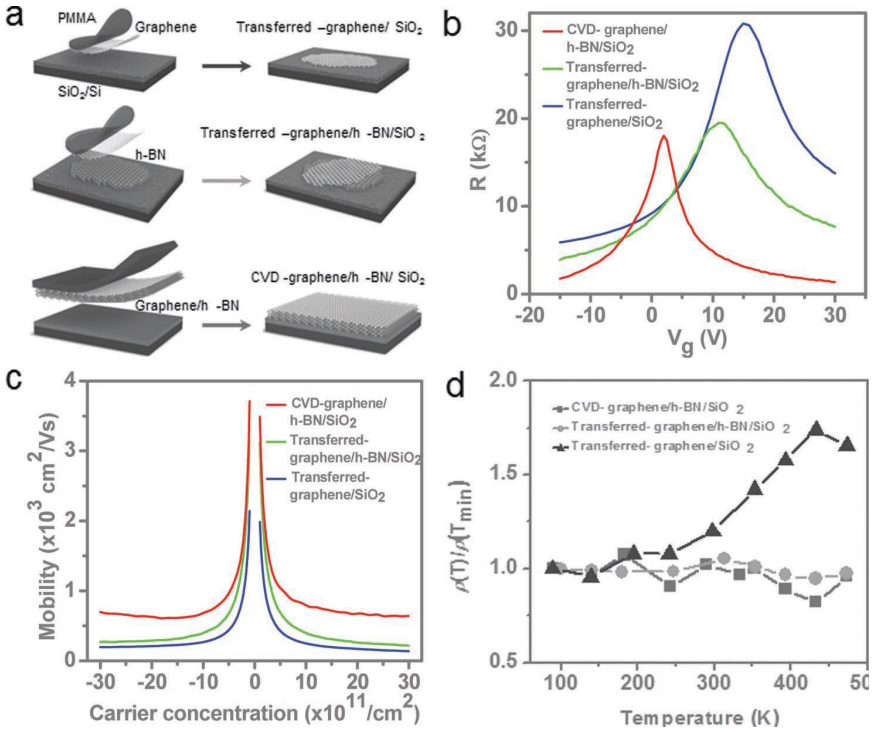

Figure 3.1: The transport properties of graphene sheets transfered onto SiO_2 and hBN were compared to directly grown graphene/hBN heterostructures showing higher performance for directly grown heterostructures. Reduced charged impurities and roughness at the SiO_2 surface showcase the benefit of 2D heterostructures. A further further improvement was observed by eliminating the transfer step which introduces residue and impurities. Reprinted from [100].

Further, as previously discussed, electronic transport in graphene is sensitive to environmental contamination, necessitating a protection layer. Reliable environmental protection demands a pinhole-free, non-reactive film. A highly insulating material is also desired to

minimize parasitic losses. It is important that a protection layer is chosen which minimally effects the underlying graphene devices. The semiconductor industry has largely relied on ALD metal oxides for this purpose, but as discussed in Chapter 2, smooth, pinhole free metal oxides films have not been demonstrated on graphene without functionalizing the graphene surface. ALD Al_2O_3 does not completely cover the graphene surface until thicknesses exceed 10 nm leading to charge puddles.[85] It is again clear that 2D, crystalline materials are ideally suited to provide reliable environmental protection.

Charged surface states [102, 103, 104, 105], surface roughness [106, 107, 108, 105], and impurities [109, 103, 104, 24, 105] severely limit graphene device performance. As these features are prevalent in metal oxides, significant research has been conducted to identify crystalline material systems which are stable in 2D form yet exhibit dielectric or semiconducting character. Layered structures exhibit far less interaction with the transport in the neighboring layer and are thus ideally suited for gating and protection of graphene devices. Boron nitride, transition metal dichalcogenides (MoS_2, $MoSe_2$, WS_2, etc), silicon and germanium analogs of graphene, silicene [110] and germanene [111], and 2D GaN [112] have since been experimentally synthesized, providing an extensive library of 2D materials to be integrated in graphene devices and includes both insulators and semiconductors.

Recently, several groups have experimentally demonstrated direct van der Waals growth of these 2D materials on epitaxial graphene. Small crystals of MoS_2 [113, 114, 115] have shown varying degrees of epitaxy, but display non-uniform growth and a quick transition to vertical growth of incomplete layers. Similarly, WS_2 crystals were grown on epitaxial graphene surfaces, but stress buildup would often cause formation of pyramids and nanorods [116]. WSe_2 also yields non-uniform coverage and inhomogeneous thickness[117, 118]. Lin, et al, demonstrated local growth of MoS_2, WS_2, and hBN on epitaxial graphene surfaces, but without long range order or uniformity [119, 120]. However, despite the challenges showcased in these efforts, epitaxial van der Waals solids have been demon-

strated on epitaxial graphene via growth of single crystal GaN [121]. The growth was conducted in two steps: a nucleation step at low temperature, and a lateral growth phase at higher temperature. In order to achieve uniform 2D layers, nucleation and growth steps must be engineered to encourage lateral growth, while controlling film stress. Selected results are showcased in Figure 3.2.

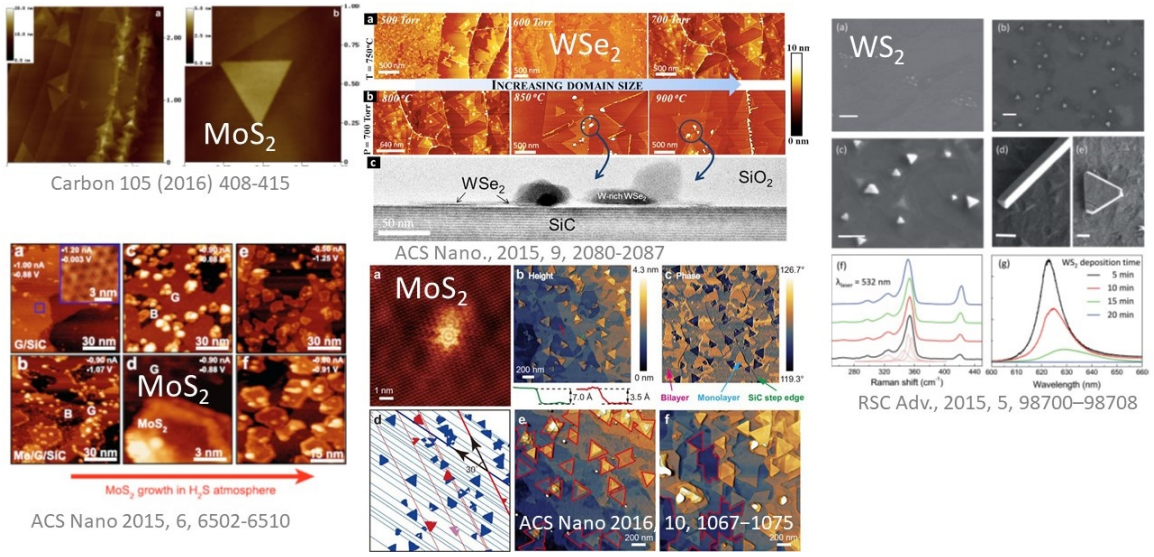

Figure 3.2: Direct growth of van der Waals solids is becoming a popular research field, but, to date, long range order has not been achieved. Reprinted from [115, 113, 115, 118, 116].

3.2 Boron Nitride for Graphene Nanoelectronics

Of all the 2D materials, boron nitride is perhaps the most important for graphene-based devices due to its wide bandgap and chemical and thermal stability. This makes it useful as a gate, tunneling barrier, and environmental protection layer. Further, its structure is nearly identical to graphene. Due to this, much work has been done to synthesize and integrate BN into graphene devices.

Boron nitride is an isomorph of graphene and enables graphene devices with improved mobility compared to metal oxide layers. It exists in two layered polymorphs, rhombohedral (rBN) and hexagonal boron nitride (hBN) which are differentiated by their stacking

order, as shown in Figure 3.3. The stacking of rBN is ABC, while hBN is AA'. Both rBN and hBN are sp^2 hybridized with interlayer van der Waals forces of approximately 52 meV, compared to 3.25 eV for the B-N sp^2 bond within the layer. Similar to graphene, BN, ideally, exhibits no dangling bonds and surface charge traps. Optical surface modes have higher energies than metal oxides which should lead to improved high temperature device performance, as demonstrated in Figure 3.1d.[100]

The honeycomb BN lattice is lattice matched to graphene, exhibiting only a 1.7% mismatch (a_{hBN}=2.50 Å vs. $a_{graphene}$=2.46 Å) leading to many of the benefits of BN dielectric layers and substrates over amorphous oxides. It has been shown that for 2D heterostructures, tunneling current sharply decreases with increasing lattice mismatch, making BN an ideal candidate for graphene-based devices.[98] Compared to transition metal dichalcogenides, BN also exhibits smaller corrugations, removing another source of scattering.

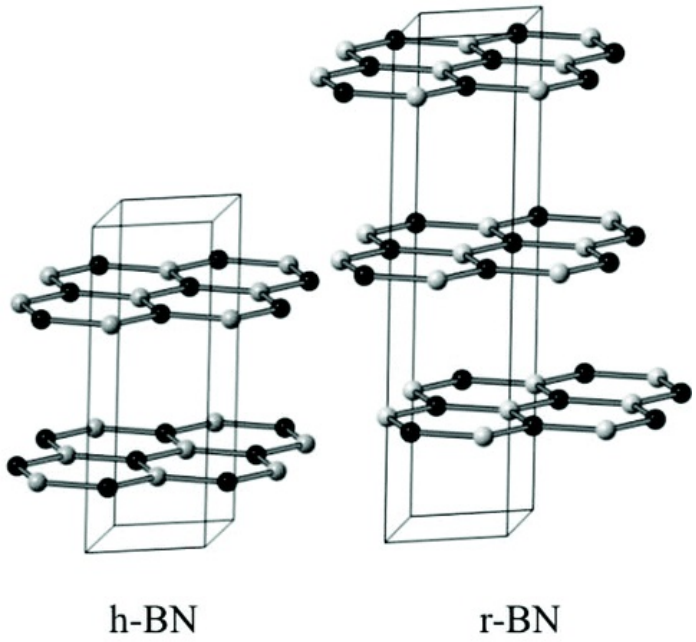

Figure 3.3: Boron nitride exists in two sp^2 hybridized layered structures, hexagonal and rhombohedral which are differentiated by the stacking order. hBN is AA', while r-BN is ABC. Reprinted from [122]

Both polymorphs of BN are wide band gap semiconductors with a band gap of approx-

imately 6 eV and very similar band structures. The debate continues as to whether either form is a direct or indirect semiconductor. Theoretical treatments often yield indirect band gaps of 5.5-6 eV [123, 124] despite experimental evidence for a direct band gap [125, 126]. Experimental evidence also exists for an indirect band gap via a phonon assisted excitation [127]. Regardless, while important for optical applications, for use in electronic devices as a protection layer, gate, or tunneling barrier, either rBN or hBN would be suitable and a significant improvement over metal oxide layers. Further, many applications desire only a single layer, for which there is no distinction between rBN and hBN. The dielectric constant perpendicular to the layers of BN is on order of 4-5 in either structure.

The electronic transport of hBN supported and gated graphene devices is improved with respect to metal oxide dielectrics. Bulk hBN supported graphene devices exhibit improved transport over SiO_2 supported graphene due to reduced surface roughness.[128, 101] Exfoliated graphene transfered to hBN flakes show a 300% increase in mobility with no change in sheet resistance compared to SiO_2 substrates, implying a 3x reduction in charged scattering centers [129].

Transfered hBN films as top gates also enhance graphene performance compared to metal oxides. Graphene transistors with a hBN gate exhibited hole doping due to charged impurities, attributed to the transfer process, although the carrier concentration of 6×10^{12} cm^{-2} was still $4\times$ lower than that induced from HfO_2 [8]. Lee, et al, fabricated a graphene field effect transistor (FET) supported on hBN which exhibited mobilities $3\times$ greater than SiO_2-based devices [130]. In another example, hBN layers were used as a top gate on a graphene FET which showed no reduction in mobility compared to the virgin graphene and a dielectric constant of 2-4 [96].

3.2.1 CVD hBN Growth Methods

Typical methods of growing BN films include ammonia borane, borazine, and triethylborane and ammonia in CVD[131, 132, 133, 134, 135, 136] and ALD[137, 138] systems,

pulsed laser deposition (PLD) from sintered targets [139], and molecular beam epitaxy (MBE) [140, 141]. Due to graphene damage from high energy PLD systems and limited accessibility to MBE systems, the following discussion will focus on advances in CVD BN film growth and integration into graphene devices.

The most common CVD hBN production method is to decompose ammonia borane and flow the byproducts over a hot substrate. Ammonia borane ($H_3N{-}BH_3$) is an attractive precursor as it fixes the stoichiometry of the BN and does not contain any carbon which must be removed during deposition. The powder is stable at room temperature and decomposes around 65 °C. The gaseous by-products polymerize, releasing stored hydrogen and forming B-N chains, rings, and hBN films on proper substrates, as described in Figure 3.4 [142]. The ammonia borane sublimation temperature for hBN growth is often between 100-130 °C to promote hydroborazine formation.[142, 130] Typically, monolayer to few-layer hBN films are grown on catalytic metal surfaces around 1000 °C due to catalytic screening [143].

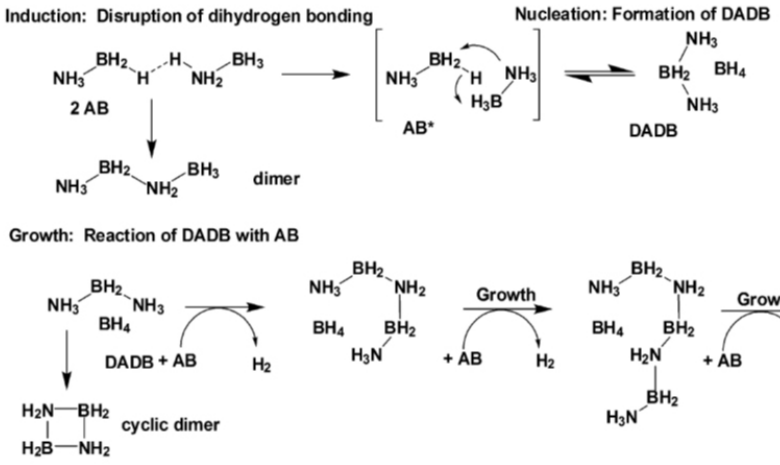

Fig. 5 The proposed thermal dehydrogenation mechanism of ammonia borane showing discrete induction, nucleation and growth steps leading to hydrogen release.

Figure 3.4: hBN growth from ammonia borane requires several intermediate steps and vapor phase reactions which complicates growth of high quality hBN films. Reprinted from [142].

Such hBN films are almost exclusively grown on catalytic metal foils, such as copper or nickel, in the presence of H_2. Bresnehan, et al, demonstrated transistors with a 10-50 nm

CVD grown and transfered hBN gate on a 75 mm quasi-freestanding epitaxial graphene wafer which exhibit cutoff thresholds 2.4x higher than HfO_2 coated devices. The hBN was grown on hot Cu foil with ammonia borane as the precursor in a low pressure tube furnace.[8]. Lee, et al, showed that the preparation of the Cu foil had a significant impact on the distribution of BN allotropes, namely cubic BN, and size of hBN grains demonstrating the importance of the catalytic nature of Cu facets in hBN growth.[130] In all of these cases, the hBN is polycrystalline and exhibits no particular orientation to the graphene lattice, as exemplified in the cross sectional TEM images in Figure 3.5.[96] Therefore, metal foils are not suitable substrates for synthesizing materials for high performance electronics.

An alternative single source precursor for hBN is borazine, which is a cyclic benzene-like ring of B-N. Borazine derived hBN layers have attracted much attention due to their high crystalline quality. The films are often grown on metal (111) surfaces in low pressure or ultra high vacuum (UHV) systems. Park et al, synthesized hBN films of varying thicknesses on different facets of Pt, showing that Pt(111) resulted in multilayer films, while low pressure growth on (100) resulted in monolayer films demonstrating the importance of the surface catalysis in decomposing the borazine precursor [144]. Hemmi, et al, demonstrated single crystal monolayer BN films on epitaxially grown Rh(111) in an UHV CVD system [145]. Borazine derived films have shown Raman excitations at the E_{2G} mode with FWHM of 11-15 cm^{-1} [146], comparable to the best bulk BN crystals[125, 147]. Despite the benefits, borazine was not chosen for this study due to handling complexity, as the liquid must be kept chilled to avoid decomposition.

Metalorganic chemical vapor deposition of hBN via triethylboron and ammonia and molecular beam epitaxy will be discussed in Chapter 4.

3.2.2 Direct Growth of Graphene-hBN Heterostructures

It is clear that direct deposition of graphene/hBN heterostructures is essential to avoid trapped charged impurities from the transfer process and enable precise registry between

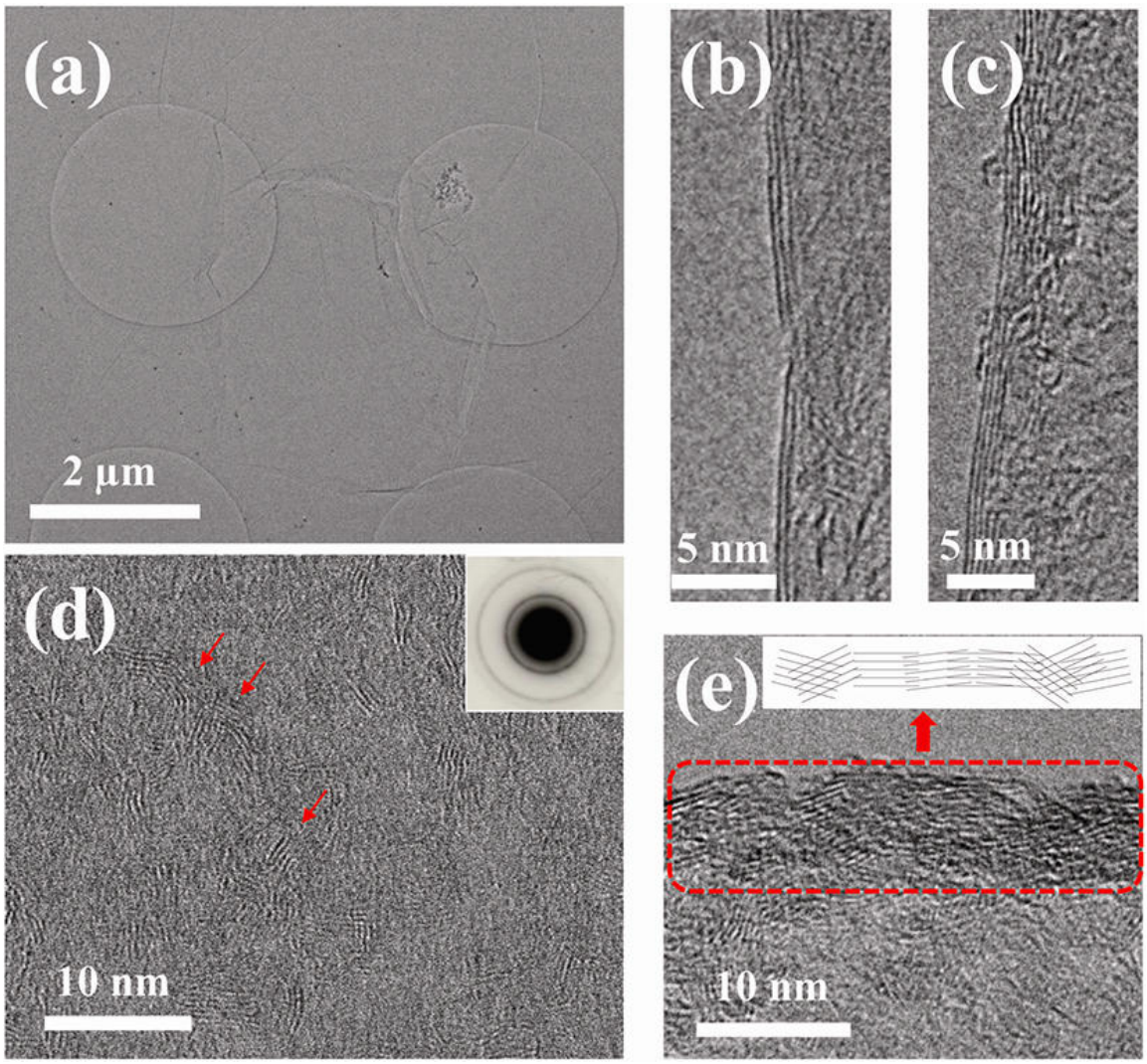

Figure 3.5: When metal foils are used as substrates for 2D material synthesis, randomly oriented grains are formed due to the rough polycrystalline foil. This morphology is incompatible with high performance electronics and, thus, metal foils are not suitable substrates for synthesizing electronics grade materials. Reprinted from [96].

the graphene and hBN lattice. Ideally, heterostructures would be coated in situ, prior to exposure to atmosphere via a high purity vapor phase deposition technique.

Much work has focused on growing graphene layers on boron nitride substrates and layers. Bjelkevig, et al, demonstrated CVD graphene deposition on ALD hBN on Ru(0001). It was found that the graphene was extrinsically doped by the underlying BN layer, although the fluorescence in the Raman spectra indicates high defect concentration in the BN layer [133]. Later work demonstrated direct CVD growth of graphene monolayers on CVD hBN on Cu foil.[148] Wang, et al, compared the effect of direct CVD graphene growth to transfered graphene. Direct CVD graphene was found to exhibit mobilities $2-3\times$ higher than transfered graphene and reduce carrier densities by an order of magnitude compared to graphene that was transfered to hBN. The difference between the CVD and transfered graphene on hBN indicates lower doping and fewer charged impurities resulting from the transfer process.[100]

Despite many examples of CVD graphene grown directly on hBN, very little work has been published demonstrating direct growth of hBN on graphene (or HOPG) surfaces. To date, three approaches have been used: polymer derived ceramics, CVD, and MBE (see Chapter 4).

Polymer derived ceramics utilize a spun-on polyborazylene solution which is then annealed at high temperatures. These thick films often contain high oxygen content, yet retain crystalline character on epitaxial graphene substrates, as shown in Figure 3.6, indicating the forgiveness of van der Waals solids to defects and induced strain [149]. As evident by the epitaxial growth of transition metal dichalcogenides on graphene, van der Waals solids can accommodate lattice mismatches in excess of 25%, compared to just a few percent for traditional materials. Further, due to the spin coat process, polymer derived ceramics are not suited for graphene passivation due to retained organic elements.

CVD hBN growth has also been attempted on graphene and HOPG surfaces. Selected Results are summarized in Figure 3.6. Liu, et al, demonstrated hBN growth via am-

monia borane decomposition on CVD graphene layers; however, TEM analysis revealed nanocrystalline hBN surrounded by an amorphous BN matrix [150]. An amorphous layer was also formed between HOPG and hBN. [151] Lin, et al, demonstrated hBN films from ammonia borane on epitaxial graphene, but TEM analysis revealed no long range order or indicate of epitaxy.[120] Single layer graphene/hBN sheets showed that hBN growth could be initiated at graphene edges.[152]

Borazine has also been used to deposit BN nanoplatelets on 900 °C substrates with thicknesses up to 30 nm on graphene flakes [153]. All of these examples showcase the challenge of creating uniform crystalline BN layers directly on graphene surfaces. Other work attempted to use borazine to grow hBN on epitaxial graphene.[154] As the growth temperature was increased to 1350 °C, 3D growth and hydrogen etching was observed. At 1100 °C, $2\,\mu\mathrm{m}$ grains were reported, but AFM showed a depression indicating possible etching. The same group found that hBN would substitute for CVD graphene on copper foils creating in-plane heterostructures, likely due to the high temperature hydrogen environment etching the graphene.[155]

The goal of the following research is to realize direct integration of 2D boron nitride onto epitaxial graphene nanoelectronics. In this thesis, two methods are explored: CVD with ammonia borane as the BN precursor in a high vacuum CVD system and a novel lateral atomic deposition (LAD) approach with triethyleboron (TEB) and ammonia as the boron and nitrogen sources, respectively.

3.3 CVD Approach for BN-Graphene Heterostructures

Since graphene has no catalytic potential, higher substrate temperatures are expected to facilitate hBN formation on graphene substrates from the byproducts of the ammonia borane decomposition compared to catalytic metal foil substrates. Jang, et al, recently demonstrated hBN growth on sapphire, a non-catalytic substrate, with ammonia borane at temperatures of 1400 °C, which suppressed the pleated morphology found in strained samples

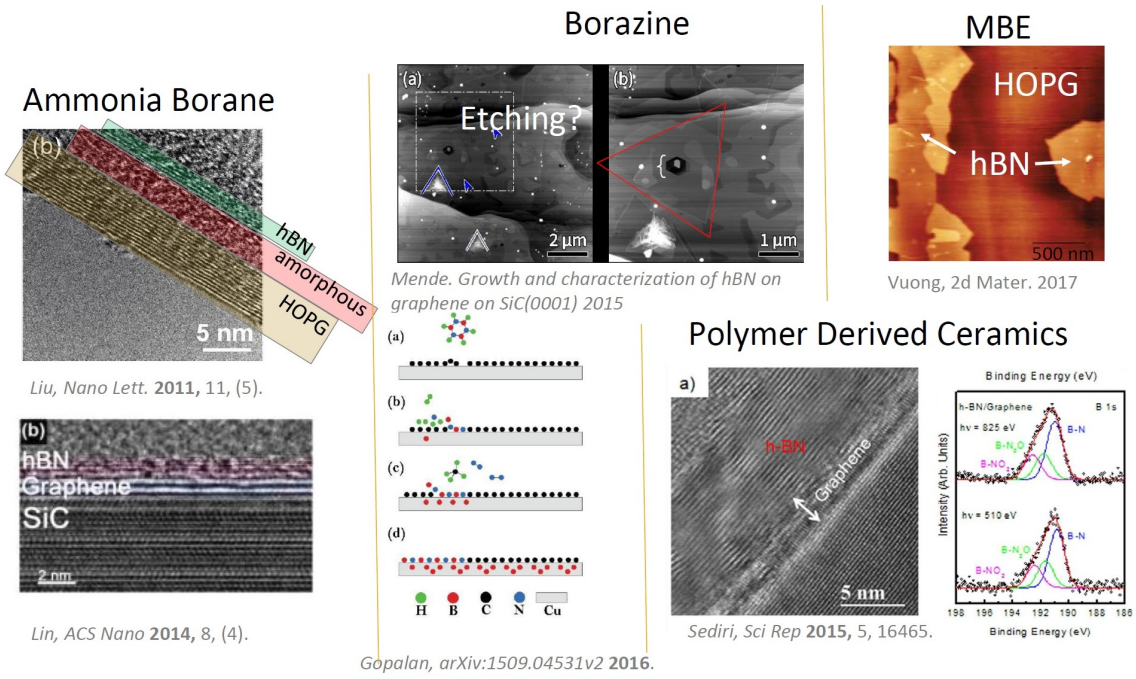

Figure 3.6: Selected results of direct growth of hBN on graphene and HOPG surfaces showcasing the challenges across CVD, MBE, and polymer derived ceramics techniques. Reprinted from [151, 120, 154, 155, 149, 156].

grown at lower temperatures [157]. Thus, I designed and built a CVD reactor to accommodate deposition temperatures up to 1750 °C. See Appendix A for a detailed system description.

CVD Reactor Design

A custom linear tube CVD reactor, as described in Figure A.2, was assembled to study the ammonia borane decomposition and polymerization on epitaxial graphene samples. To facilitate high quality films with low oxygen content, the system was designed to reach a base pressure of 10^{-7} mbar. The ammonia borane precursor was heated to 60-120 °C and the gaseous by-products were carried with 5% H_2/Ar to the deposition zone which was heated via an induction coil and graphite susceptor to 300-1750 °C. A throttle valve enabled deposition pressures from 10^{-6} mbar up to atmospheric pressure. The substrates were vacuum annealed at 800 °C prior to BN growth to ensure clean surfaces which are

essential to enable epitaxial BN growth.

Ammonia Borane Results

A large processing parameter space was studied yielding evidence of 2D hBN growth on buffer layer and graphene after high temperature annealing. Deposition pressure, substrate temperature, precursor temperature, and post-deposition annealing conditions were varied.

Prior reports of hBN on graphene were conducted using atmospheric pressure CVD (APCVD) both within the de Heer group by Yike Hu and elsewhere [152], but the results showed large granules, incomplete 2D morphology, or regions of rapid 3D growth. This has two probable causes: vapor phase polymerization of the precursor and rapid growth rates resulting in non-uniform 3D clusters. In response, a low pressure CVD (LPCVD) process was implemented to increase the carrier gas velocity; the precursor decomposition temperature was lowered to 80 °C to reduce mass flow, and the substrate temperature was increased to 1400 °C to encourage lateral growth due to the high mobility on graphene and hBN surfaces in order to limit island nucleation, as described in Chapter 1. The film was then vacuum annealed to crystallize the thin, granular regions, which resulted in unified BN domains as seen in Figures 3.7 and 3.8, for buffer layer and graphene, respectively. XPS analysis, shown in Figure 3.9, is typical of stoichiometric hBN with minimal oxygen and carbon content. As the hBN films were sub-monolayer, removal of adventitious carbon and oxygen was not possible. Nonetheless, the total detected concentration was only a few atomic percent for each. This result also persists in granular films suggesting vapor phase parasitic reactions or strain induced crumpling upon cooling.

In conclusion, while the evidence suggests that CVD hBN deposition on the epitaxial graphene system should be possible, control of the deposition requires higher levels of precision than are attainable with the present CVD tool. Nonetheless, several key observations are valuable:

1. Low precursor flux rates enable 2D morphology, whereas high rates yield a granular

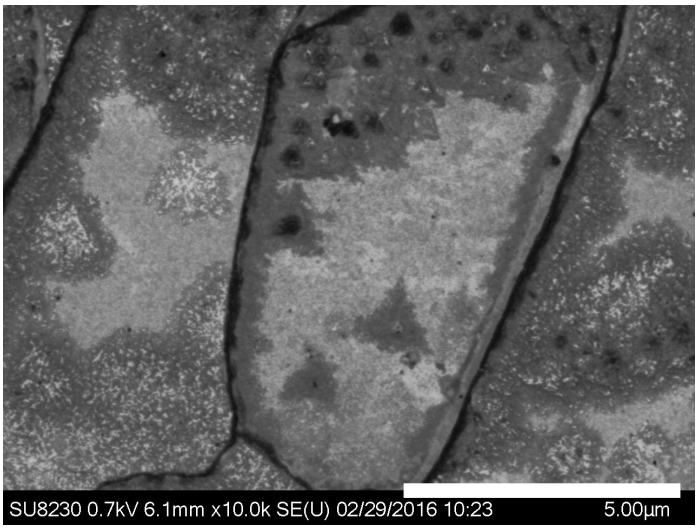

Figure 3.7: Annealed hBN, light regions, on buffer layer, dark regions, exhibiting epitaxial triangular grain growth.

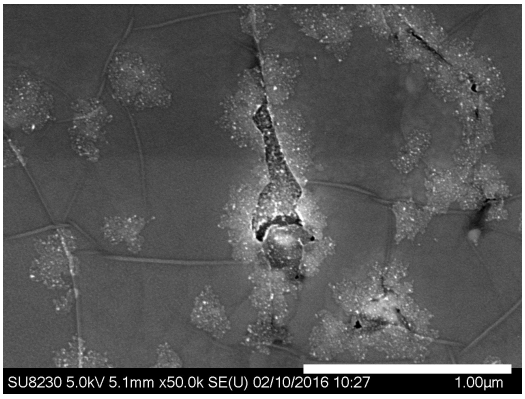

(a) Deposition: 80 °C, 3 min, 1400 °C, 2×10^{-2} mBar Annealing 1: 1400 °C, 10^{-6} mBar

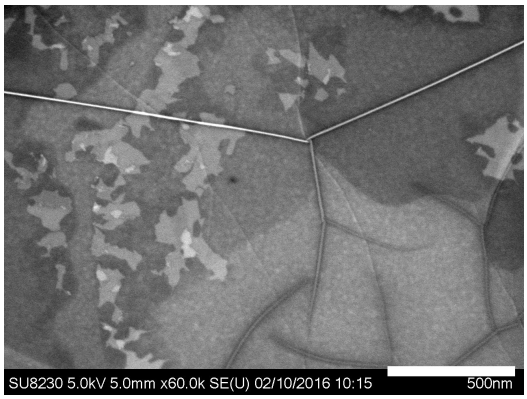

(b) Annealing 2: 1700 °C, 1 hr, 10^{-6} mBar

Figure 3.8: Direct BN deposition on multilayer C-face graphene was conducted at low temperature leading to regions of granular BN. After annealing at 1700 °C, the granular regions crystallized into planar BN grains. The bright lines are pleats present in C-face epitaxial graphene.

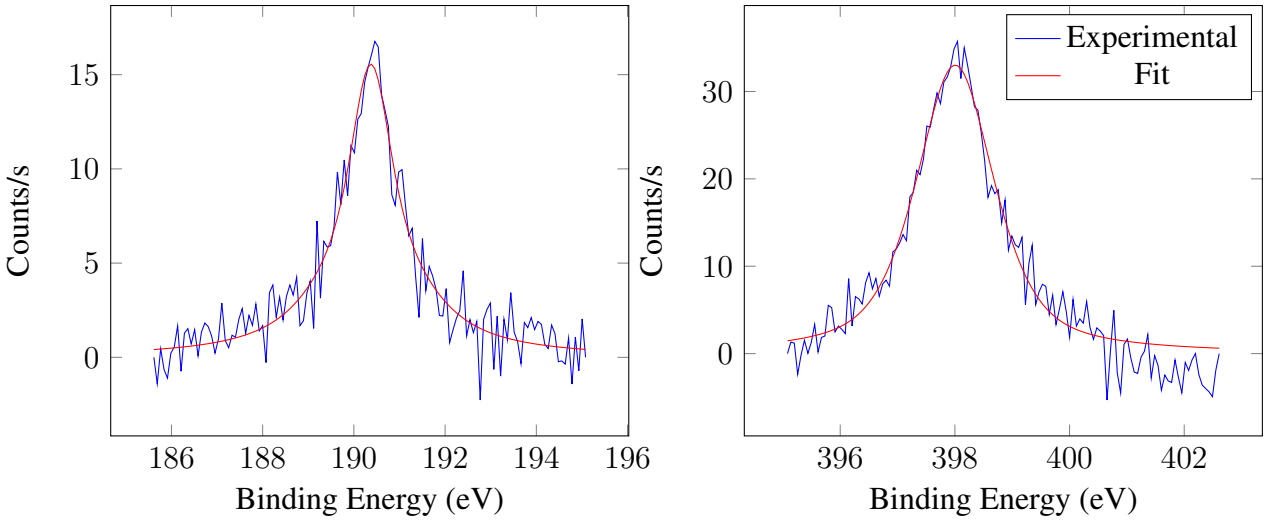

(a) Boron XPS signal centered at 190.4 eV corresponding to sp^2 bonding, typically observed at 191 eV.

(b) Nitrogen XPS signal centered 398.0 eV corresponding to sp^2 bonding, typically observed at 398 eV.

Figure 3.9: XPS taken from annealed hBN film grown via LPCVD with ammonia borane is consistent with hBN.

structure. Stable island nuclei are more likely form at high deposition rates which leads to multilayer films. Also, sufficient diffusion time must be accommodated to align impinging grains. Epitaxial metallic platelets have been grown on HOPG surfaces using low precursor fluxes, whereas amorphous materials are grown at under high flux conditions to out-compete surface diffusion.

2. High temperatures during deposition and annealing contribute to higher quality BN films by encouraging lateral growth. High temperatures increase the potential barrier for island nucleation, enable high surface diffusion rates, and allow adatoms to overcome surface potential wells.

3. Vapor phase parasitic reactions must be eliminated to ensure 2D growth. Cold walled reactors will limit precursor decomposition and polymerization prior to the growth zone. Additionally, chemical reactions can be separated into half reactions, as in ALD.

CHAPTER 4
LATERAL ATOMIC DEPOSITION

This chapter presents a novel deposition technique, specific to 2D heterostructures: lateral atomic deposition (LAD). Direct growth of hBN/epitaxial graphene heterostructures will serve as proof of concept. LAD is the 2D analog to atomic layer deposition (ALD) where instead of a 2D layer of atoms being deposited with each cycle, a 1D row of atoms is added to the boundary of a grain. A generalized process is shown in Figure 4.1. There are many reports of 2D material synthesis with ALD, but it is important to note that these examples all rely on the coalescence of nanocrystalline material, producing a monolayer within a few cycles.[158, 159, 160, 161] They do not demonstrate controlled lateral growth. This often leads to polycrystalline films which are ill-suited to high performance nanoelectronics and is limiting for integrated structures. In contrast, LAD will be shown to produce large grains (100's nm) which are oriented with respect to the substrate leading to single crystal films over large areas. Also, the cyclic nature of the process, in principle, could enable direct growth of in-plane ribbon structures and composition gradients. This stark contrast in growth regime which is afforded by refractory 2D material systems offers new opportunities for high performance nanoelectronics, highly scalable manufacturing processes, and self-assembled nanostructures.

4.1 ALD vs LAD

Atomic layer deposition has been a staple in semiconductor manufacturing for the past several nodes. It provides precise control over layer thickness in 3D materials and has been adapted to a wide range of materials. Most notably, it is ideally suited to deposit large area, ultra thin dielectric layers, such as HfO_2. ALD relies on self-limiting precursors to ensure uniform coatings with high thickness precision. In an ideal process, as shown in Figure

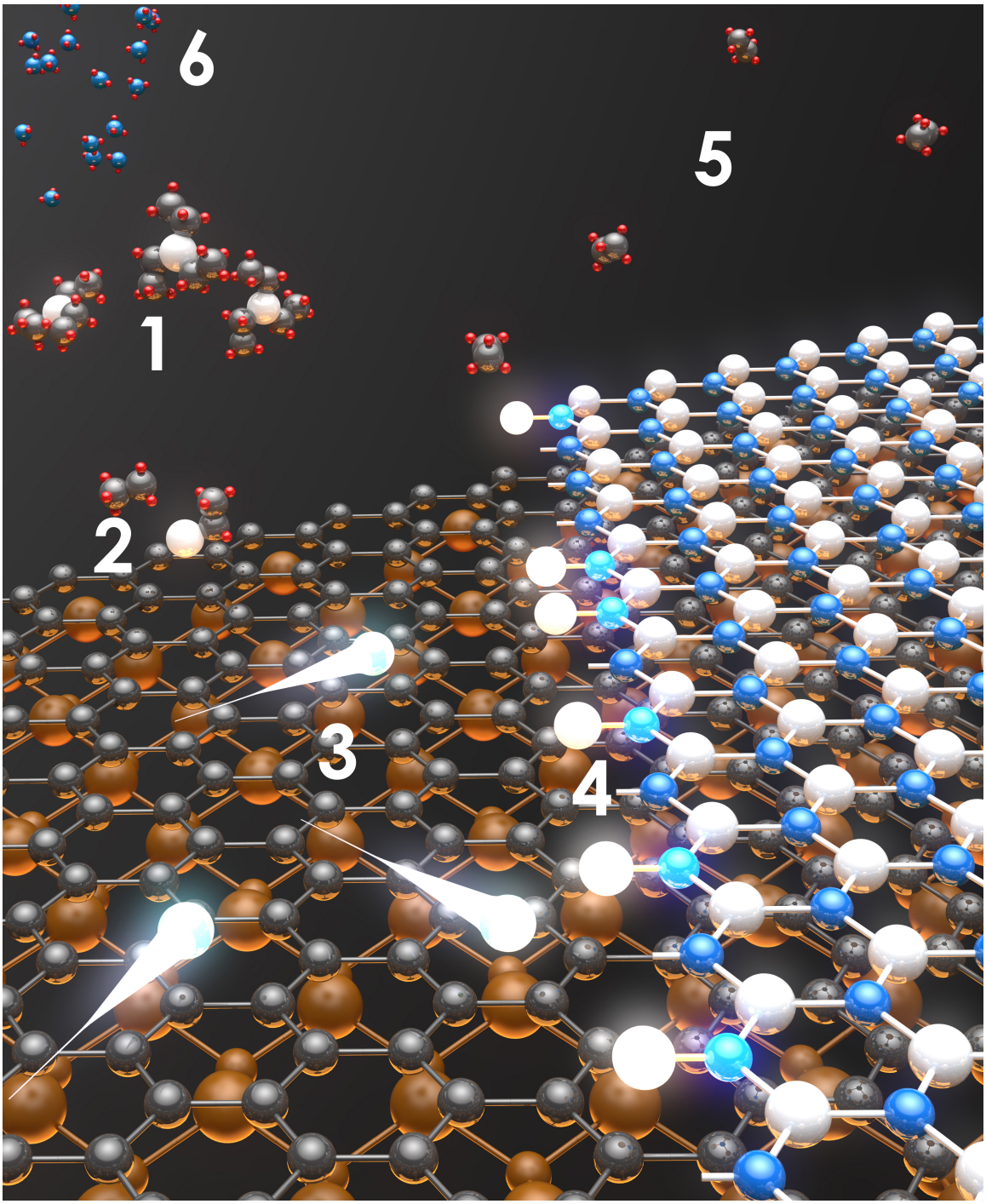

Figure 4.1: The lateral atomic deposition (LAD) process is the 2D analog to ALD. Instead of depositing a monolayer per half-cycle, a single row of atoms is woven onto the step edge. After the first precursor is injected (1), the molecules decompose on the surface (2), and then diffuse across the surface (3) until they find a suitable site on the edge of the growing film (4). The by-products of the decomposition are pumped away (5) and the precursor for the second half-cycle is introduced (6). The cycle is repeated until the film covers the desired surfaces.

4.2, the precursor completely saturates a heated surface, while excess precursor is pumped away. Often, as is the case for oxides, the second half cycle presents a different precursor, and the process is repeated, building up a pin-hole free film one atomic layer at a time.

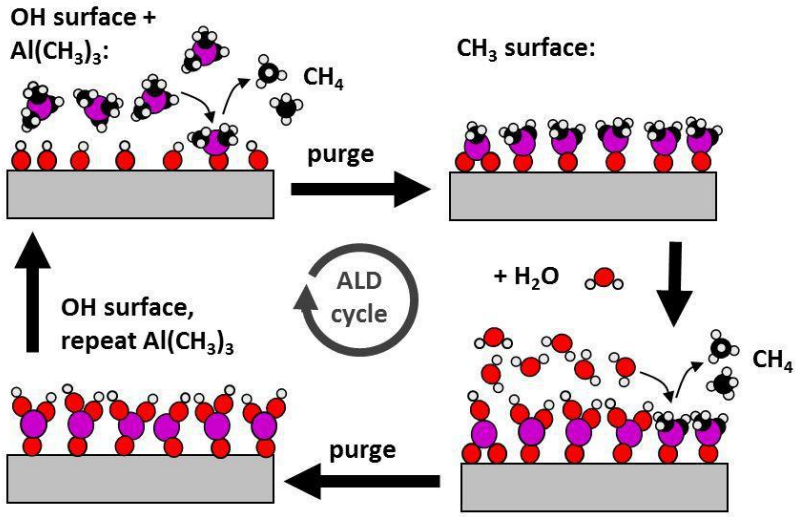

Figure 4.2: An ideal atomic layer deposition cycle begins by saturating the surface with the first precursor. The excess precursor is then purged prior to initiating the second half-cycle. In an ideal process, one atomic layer is deposited with each half-cycle. Reprinted from Pearson Group.

However, there are several caveats which must be considered to achieve the ideal growth properties of ALD, namely substrate temperature, surface adhesion, and precursor stability. Combined, moderate temperatures are often ideal for high quality amorphous dielectric films as there is sufficient thermal energy to crack the precursor, but not decompose ligand tails, and to enable some surface diffusion. Temperatures of a few hundred degrees are ideal for metalorganic precursors to avoid significant carbon content in the film.

When considering crystalline films, higher temperatures are required to increase surface diffusion so adatoms can find thermodynamically preferred sites. However, this is often accompanied by undesired precursor decomposition. Carbon content tends to rise, which severely degrades the dielectric film properties.

The epitaxial graphene system lifts many of these constraints, rendering it an ideal test bed to develop a true 2D material deposition method for both in-plane and out-of-

plane heterostructures. The SiC substrates and graphene are refractory materials, enabling deposition and annealing temperatures in excess of 1500 °C. Further, 2D materials, such as graphene, reducing the adatom hopping barrier, enabling much higher surface mobilities, especially on the pristine epitaxial graphene surface.

4.2 Lateral Atomic Deposition of Boron Nitride on Epitaxial Graphene

Lateral atomic deposition, like molecular beam epitaxy (MBE) and metalorganic vapor phase epitaxy (MOVPE), uses separate precursor sources for both boron and nitrogen and does not rely on a catalytic substrate.

Molecular beam epitaxy has also been explored on HOPG substrates and offers the potential for improved purity with pure boron and nitrogen sources.[156] However, growth rates were exceptionally low (0.09-1.15 ML/3 h), the hBN was polycrystalline and exhibited no preferential orientation with respect to the HOPG lattice. Further, the plasma nitrogen source is likely to damage graphene devices. As the growth temperature was increased, the growth rate was found to decrease as would be expected if the adatoms were approaching Levy flight conditions, as discussed in Chapter 1. At low substrate temperature (1390 °C), multilayer hBN islands were formed; whereas, at high temperature (1690 °C), single layer domains were grown only from the HOPG steps, as shown in Figure 3.6.

MOVPE has been shown to produce high quality 2D boron nitride films on Si [162] and sapphire[163, 126, 164] substrates. Based on the findings of the ammonia borane experiments, an exploratory study was conducted at Georgia Tech Lorraine, in Abdallah Ougazzaden's lab, to determine if cyclic MOVPE hBN was a viable path for an epitaxial graphene dielectric using triethylborane (TEB) and ammonia as the B and N sources, respectively. A commercially available Aixtron 3x2 close coupled showerhead (CCS) reactor was used. The depositions were carried out in an 85 mBar H_2 atmosphere with a NH_3:TEB ratio of 1000. TEB was dosed at 1 $\mu\mathrm{mol}/\min$ for 1 s. The system was purged for 3 s between pulses. The total flow through the chamber was maintained at 20 SLPM. Prior to

film growth, the samples were exposed to TEB to saturate the surface with boron. Selective growth of 2D hBN on graphene was observed.

As said above, wetting the surface is challenging due to the lack of dangling bonds on the high quality, epitaxial graphene surfaces. Initial tests, aiming for 3 nm of BN, revealed BN deposition, but with a granular, 3D morphology that was primarily isolated to step edges, defects, and the buffer layer and SiC surfaces. It is unknown whether this occurred during cooling due to the compressive strain caused by the graphene-hBN coefficient of thermal expansion (CTE) mismatch, or during the growth process. Several deposition profiles and wetting agents were explored to improve the graphene wetting: extended TEB preflow at deposition temperature, low temperature TEB preflow at 700 °C and 850 °C, aluminum preflow due to its strong adhesion to graphene at high temperatures, and surface nitridization.

The growth rate was found to be significantly lower on graphene samples than on sapphire substrates, likely due to adatoms approaching Levy flight conditions or higher re-evaporation rates on the graphene surface. While the growth was expected to yield approximately 3 nm thick films, sub-monolayer films were produced, as shown in Figure 4.3a. In response, several seeding options were explored. Low temperature TEB preflow yielded smoother films on graphene, but larger granules on buffer layer, as shown in Figure 4.4a and 4.3b. High temperature aluminum exposure via trimethylaluminum (TMA) resulted in smoother films on graphene, but showed nonuniform contrast under SEM analysis, possibly due to carbide formation, as shown in Figure 4.4b. Ammonia pre-exposure (in all other runs, TEB was introduced first), created a rough texture on the graphene regions indicating possible hydrogen etching, as shown in Figure 4.5a. Since none of the seeding options offered significant improvement in growth rate, BN films with significantly higher number of cycles, were grown. The results are presented in the subsequent sections.

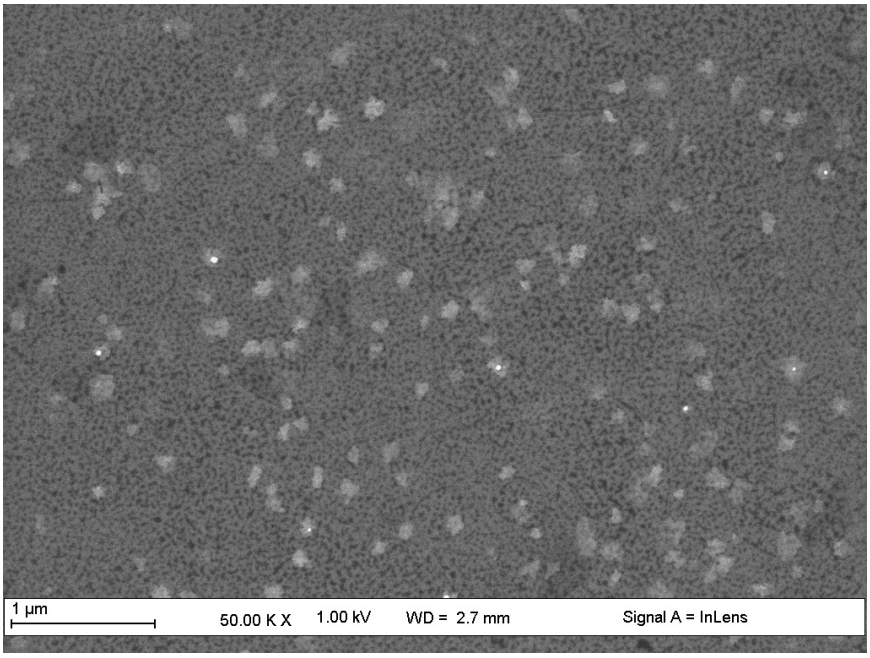

(a) Boron preflow at 1270 °C resulted in submonolayer coverage.

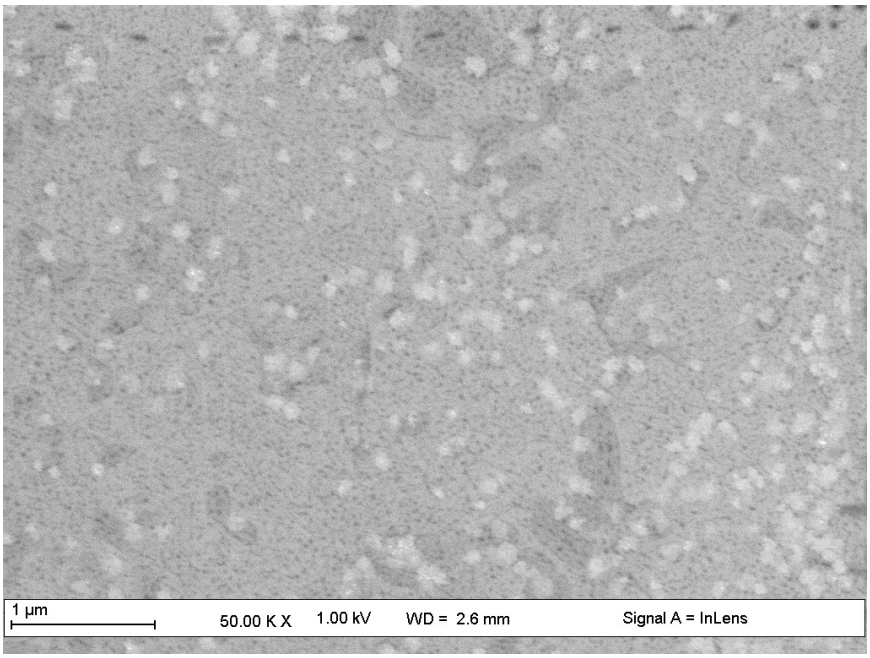

(b) Low temperature boron preflow at 600 °C resulted in submonolayer coverage.

Figure 4.3: 1 of 3. Surface morphology following hBN film seeding study. Results compare to 3 nm uniform films on sapphire.

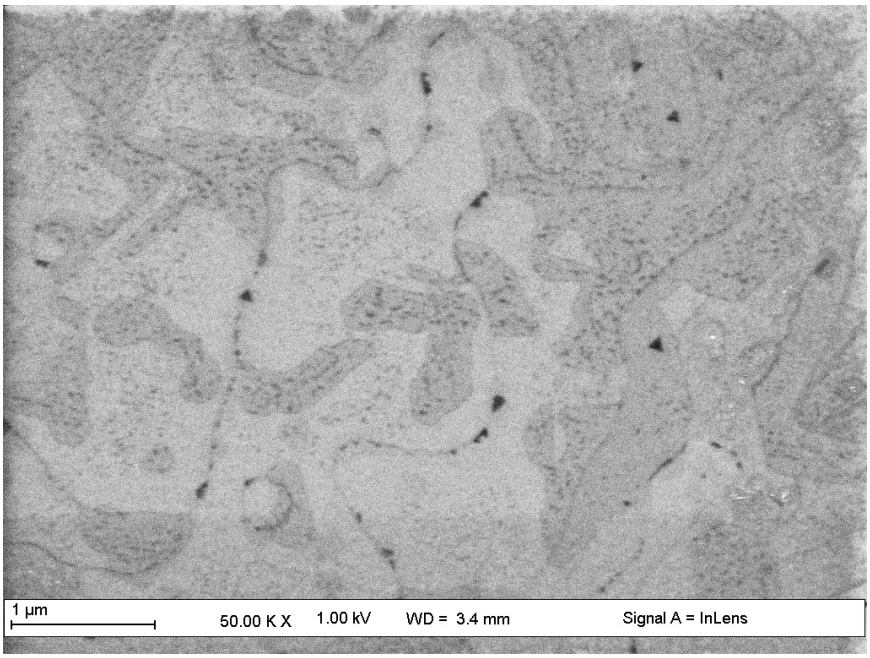

(a) Low temperature boron preflow at 850 °C resulted in submonolayer coverage.

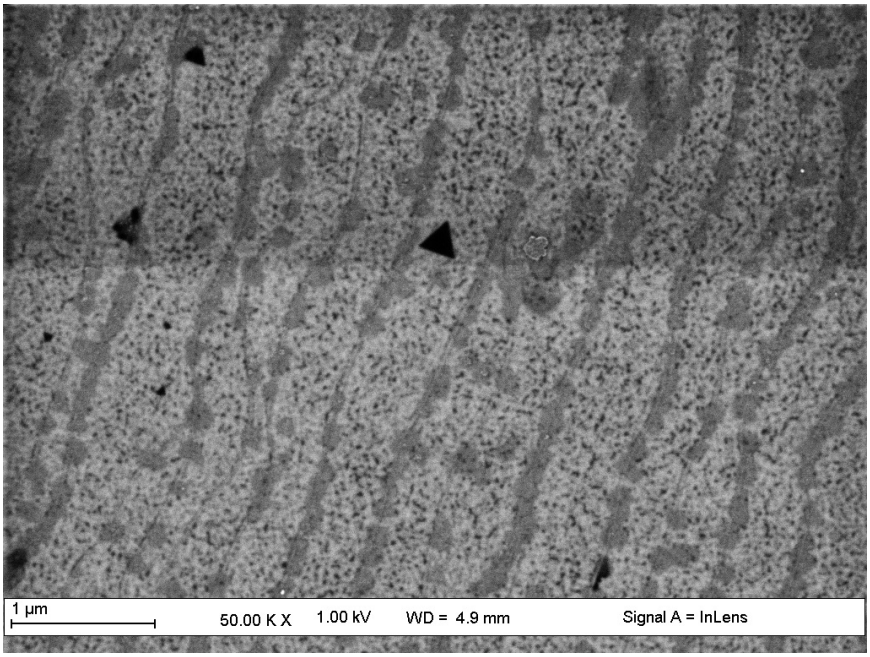

(b) An aluminum adhesion layer was applied resulting damaged graphene surfaces, likely due to carbide formation

Figure 4.4: 2 of 3. Surface morphology following hBN film seeding study. Results compare to 3 nm uniform films on sapphire.

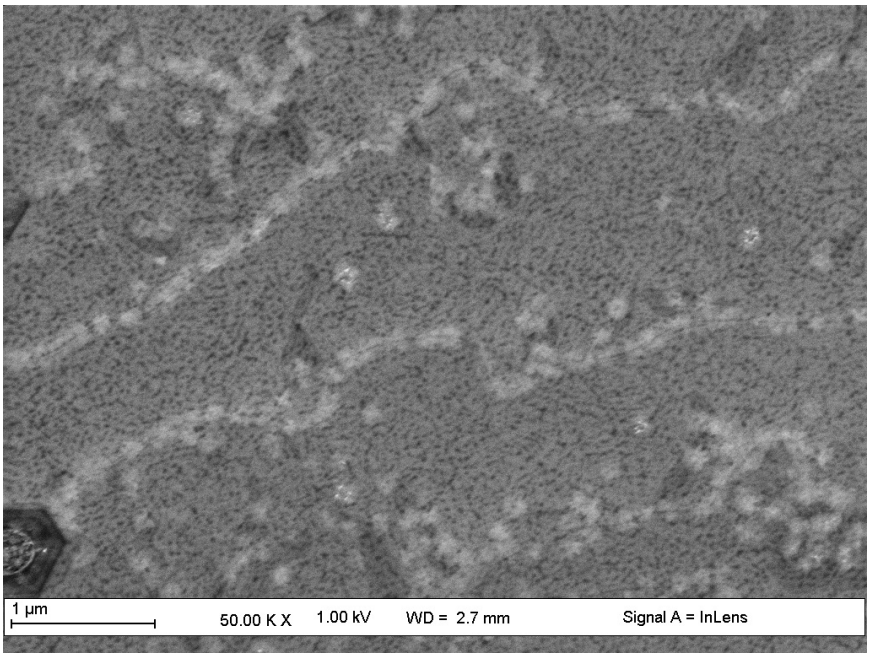

(a) Surface nitridization with ammonia at deposition temperature resulted in a rough surface, possibly due to hydrogen etching.

Figure 4.5: 3 of 3. Surface morphology following hBN film seeding study. Results compare to 3 nm uniform films on sapphire.

4.2.1 Role of Hydrogen in hBN Growth

The pure hydrogen carrier led to partial hydrogen intercalation of the buffer layer on Si-face samples and may undesirably etch graphene nanostructures. The intercalation was evident in cross sectional TEM, LEED, and Raman spectroscopy, shown in Figures 4.19, 4.23, and 4.24, respectively. As such, an inert carrier, such as helium is desirable. Early MOVPE studies of III-V materials showed that a helium ambient produced higher quality nitride films than hydrogen, but, largely due to cost, hydrogen was chosen for most subsequent studies.[165] Further, other epitaxial hBN techniques work under UHV conditions, without any carrier.[145] In response, helium was substituted for the hydrogen carrier gas.

Unlike hydrogen, helium is not expected to passivate the Si-terminated SiC surface. While He may intercalate, it is expected that moderate annealing temperatures will return the graphene to its initial state.

The high vacuum, high temperature pulsed precursor reactor, described in Appendix

B, was used to compare helium and hydrogen as carriers in high purity environments at temperatures up to 1750 °C. The base pressure was 10^{-7} Torr and deposition pressures ranged from $10^{-2} - 500$ Torr by modulating the flow of the carrier gas. Precursor dosage, carrier flow, and substrate deposition temperature were varied to optimize the chemical composition of the hBN film. High vacuum conditions were also explored.

The high temperature substrate was found to strongly decompose the ethane ligands on the TEB molecule. Despite temperatures insufficient to graphitize SiC, highly carbon-rich films were produced under helium and vacuum. In contrast, even low pressure hydrogen atmosphere strongly reduced the carbon content. Similar to the effects of hydrogen in CVD graphene growth, it is suspected that hydrogen preferentially etches carbon within the hBN film. Therefore, hydrogen is an active species in the hBN process and is necessary if carbon containing precursors are used at high temperatures.

This is in contrast to early results with GaN where hydrogen degraded the film quality.[165] It should be noted that GaN is grown at lower temperatures (700-800 °C), so the metalorganic precursor will undergo significantly less decomposition. Therefore, hydrogen etching of carbon content is unlikely to be required in these cases.

4.2.2 Characterization of Graphene and Boron Nitride

Characterizing epitaxial graphene systems requires a number of techniques to create a comprehensive picture of the structure and interactions between the layers. This section will present a brief description of various common techniques and key observations relevant to this study.

The morphology of the BN films was visually examined via scanning electron microscopy (SEM) and atomic force microscopy (AFM). The chemical composition was probed with x-ray photoelectron spectroscopy (XPS) and Raman spectroscopy. High resolution x-ray diffraction revealed a layered crystal structure. Cross sectional high resolution transmission electron microscopy (HRTEM) with energy dispersive x-ray spectroscopy was

performed to confirm the crystal structure, interface quality, and layer composition.

Surface Morphology: Scanning Electron Microscopy

Scanning electron microscopy is one of the most convenient ways to view the morphology of 2D materials quickly and over large areas. In comparison to scanning probe microscopy techniques sample morphology can be probed in just a few minutes. However, especially when considering nanostructures and semiconducting or insulating substrates, proper imaging conditions become critical. In general, a low electron landing energy, low beam current, and close working distance are mandatory to achieve high resolution images of graphene nanostructures on SiC. The low landing voltage corresponds to a small cross section and, thus, higher surface sensitivity. Ideal landing energy varies between 100 and 1000 eV, depending on the substrate and topography. On the Hitachi SU8230 SEM , the beam can be decelerated down to 10 eV; however, this operating mode demands a flat surface to maintain a non-distorted electric field. A low beam current, 5 μA, is important to reduce charging on semiconducting and insulating substrates and to minimize damage to the graphene nanostructures. Front side copper tape and good electrical conductivity between the substrate and stage can also aid in reducing charging effects. The best spatial resolution is often achieved with an in-lens secondary electron detector. For larger graphene structures, back scattered electrons, which are more sensitive to Z number, can improve contrast. Working distance must be minimized to reduce aberrations, errant magnetic fields, and probe size. Despite all of these efforts to minimize charging effects, integration times must still be limited to a few seconds to achieve the best image. These conditions are outlined in Table 4.1

Continuous BN films with a pleated surface morphology preferentially grew on graphitized regions as shown in Figure 4.7 and 4.28. A pleated morphology is indicative of van der Waals solids grown on positive CTE substrates. Similar to multilayer epitaxial graphene, BN has a negative in-plane CTE, due to out-of-plane phonon vibrations, which induces a large compressive strain upon cooling from high deposition temperatures. The

Table 4.1: SEM imaging parameters for 2D materials on semiconductors for a Hitachi SU8230

Parameter	Units	Target Value
Accelerating Voltage	kV	0.5-1
Probe Current	μA	5
Deceleration	V	100-500
Working Distance	mm	1-2
Detector		In-lens SE

weak interlayer forces allow the sheets to slide with respect to each other to accommodate this strain without cracking, forming pleats. The pleats often emerge from defects where the BN is pinned and radiate with tri-fold symmetry, indicative of biaxial in-plane strain [166]. The height of the pleats is 5-15 nm as determined by AFM, as shown in Figure 4.10.

In order to grow uniform vdW solids, film growth must occur under conditions which enable sufficient adatom mobility to encourage lateral growth of each layer. In typical MOVPE processes, the simultaneous introduction of precursors causes parasitic vapor phase reactions leading to small clusters that nucleate islands on the surface. The high temperature and carrier flow used here, in addition to eliminating vapor phase reactions by separating the precursors, contribute to low growth rate conditions which favor selective lateral growth on sp^2 hybridized surfaces, such as EG and well oriented hBN. The sp^2 hybridization on the graphene and hBN surface ensures high adatom mobility at the high growth temperatures enabling the high quality vdW heterostructure growth. The buffer layer and SiC surfaces exhibit a higher concentration of granular BN, which could be due to strain between the lattices which is not accommodated as favorably as on the graphene surfaces.

There was no discernible difference between BN grown on monolayer Si-face and multilayer C-face graphitized regions confirming that SiC catalysis was not a dominant effect. Both exhibited a pleated morphology, and a scratch test confirmed that BN layers must be deposited as the graphene thickness would not be affected by the modest pressure (85 mbar) and temperature (1260 °C) deposition process.

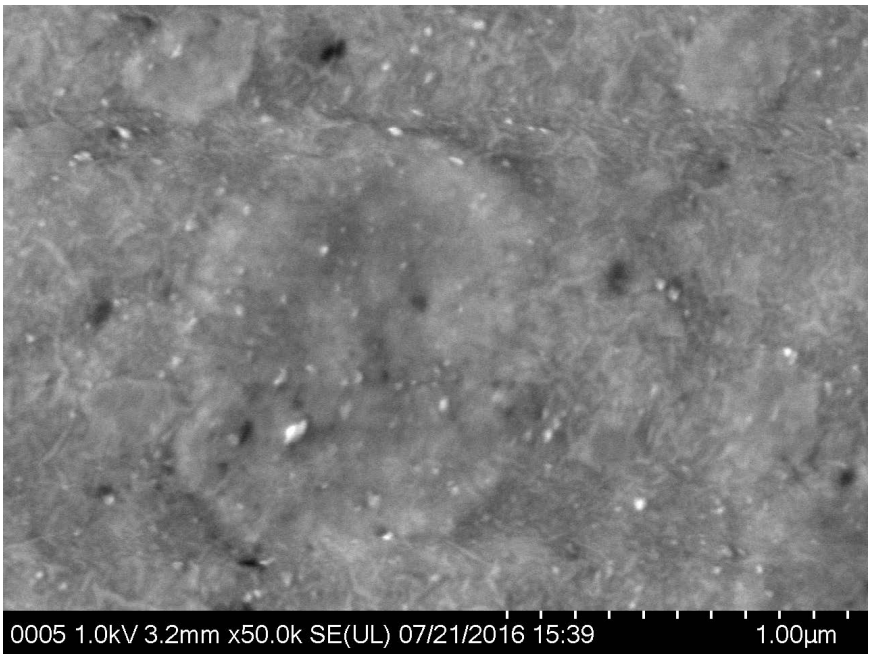

(a) BN on sapphire control sample

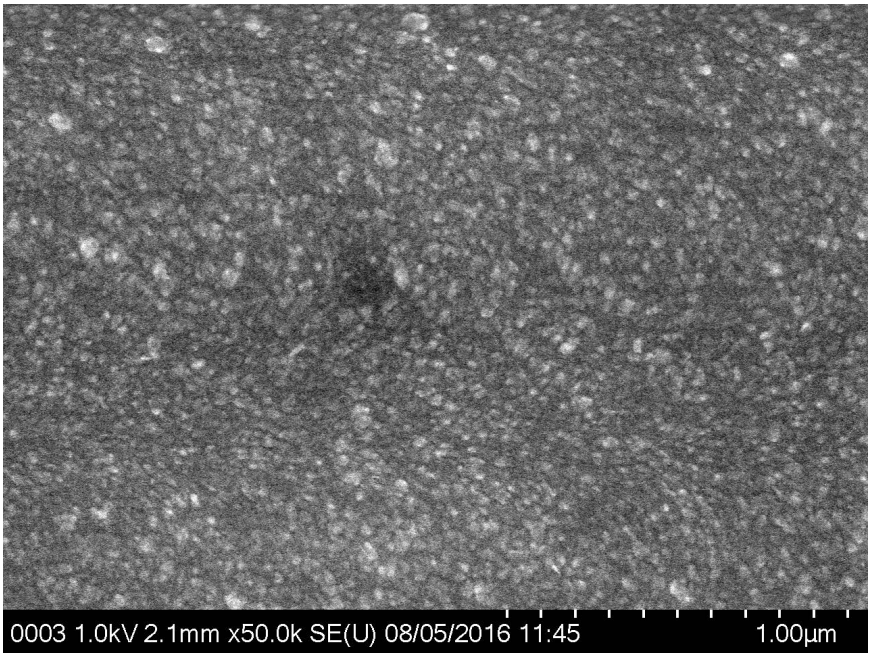

(b) Granular BN on CMP SiC surface

Figure 4.6: 1 of 4. Surface morphology of 15 nm thick LAD deposited BN on epitaxial graphene surfaces exhibiting selective area growth of 2D BN films with pleated morphology on graphene surfaces.

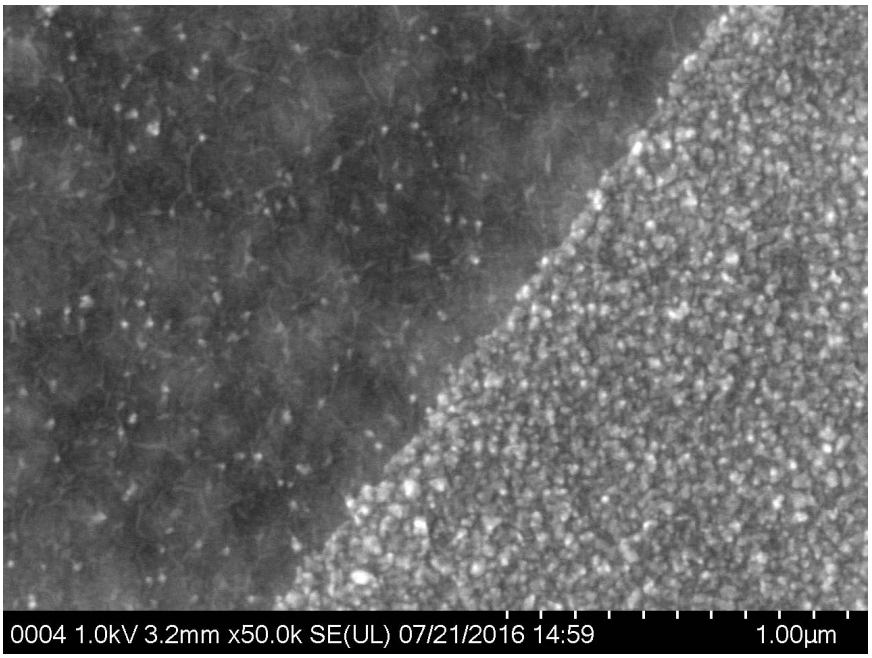

(a) Granular and tightly pleated regions of BN on adjacent SiC terraces after face-to-face annealing. The tight pleats indicate 2D layers with a high density of pinning sites due to a strong interaction with the substrate.

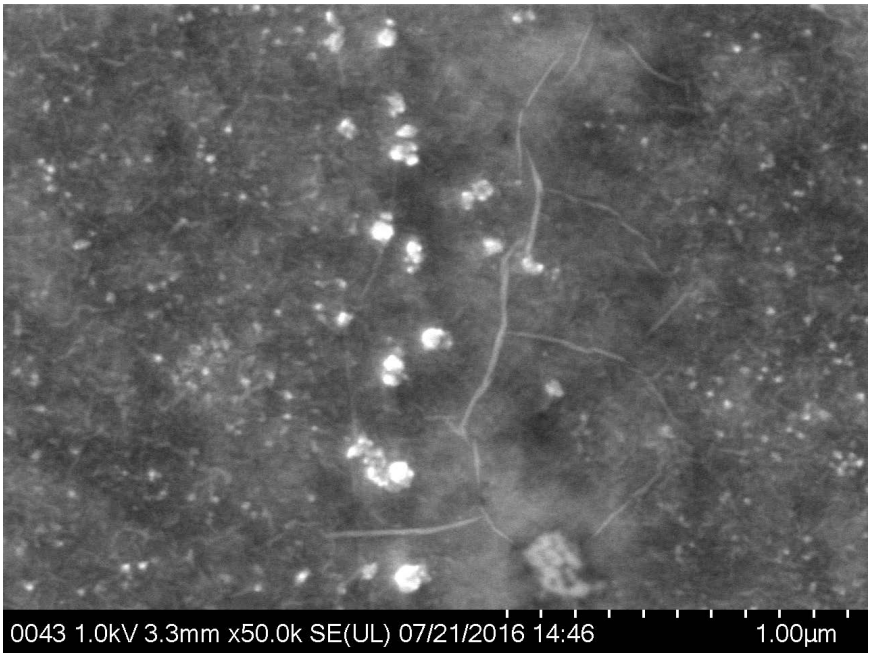

(b) BN on wide graphene nanoribbons showing large pleats over the ribbon, but high density granular morphology and a tight pleated structure on the buffer layer regions

Figure 4.7: 2 of 4. Surface morphology of 15 nm thick MOVPE deposited BN on epitaxial graphene surfaces exhibiting selective area growth of 2D BN films with pleated morphology on graphene surfaces.

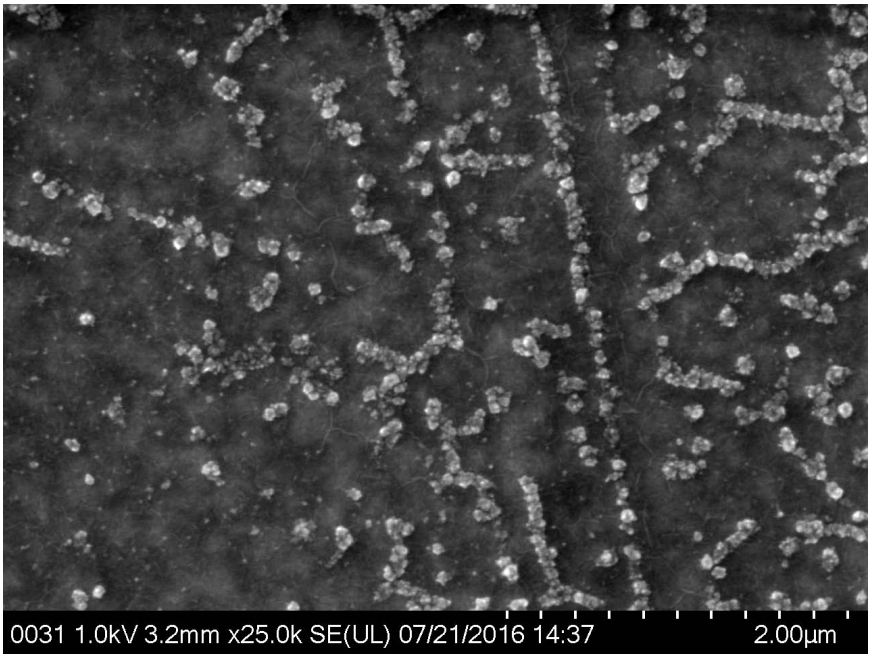

(a) BN on narrow graphene nanoribbons showing smooth, pleated BN overlayer on the nanoribbon, but with higher density of granules on the surrounding buffer layer. The ribbon is along the step edge indicated by the straight line of granules and exhibits no granules within the ribbon boundaries showcasing the promise of LAD for nanostructures.

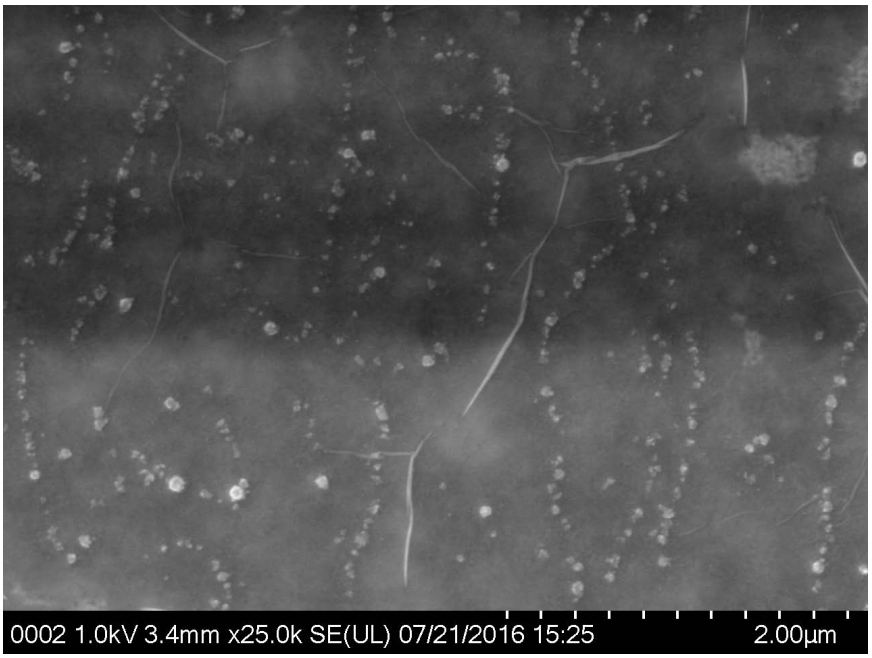

(b) BN on monolayer Si-face graphene exhibiting a pleated morphology and few granular clusters

Figure 4.8: 3 of 4. Surface morphology of 15 nm thick LAD deposited BN on epitaxial graphene surfaces exhibiting selective area growth of 2D BN films with pleated morphology on graphene surfaces. The tight pleated structure visible on the buffer layer and SiC surfaces indicates a higher level of pinning than on graphene, but demonstrates that if the conditions can be modified, 2D BN films can be grown over the entire system.

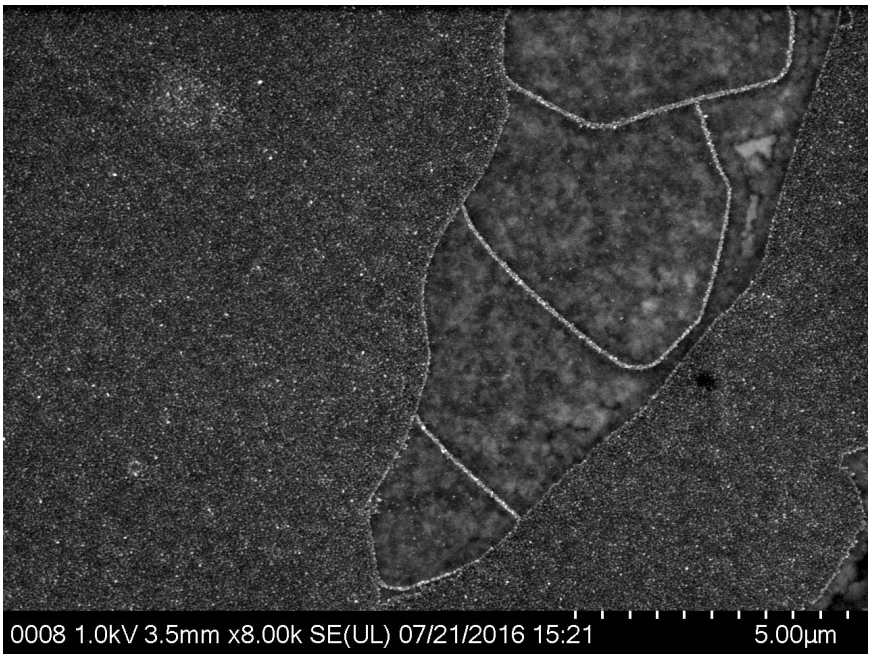

(a) BN on C-face monolayer graphene domains showing smooth BN films over the graphene domains and a granular structure outside

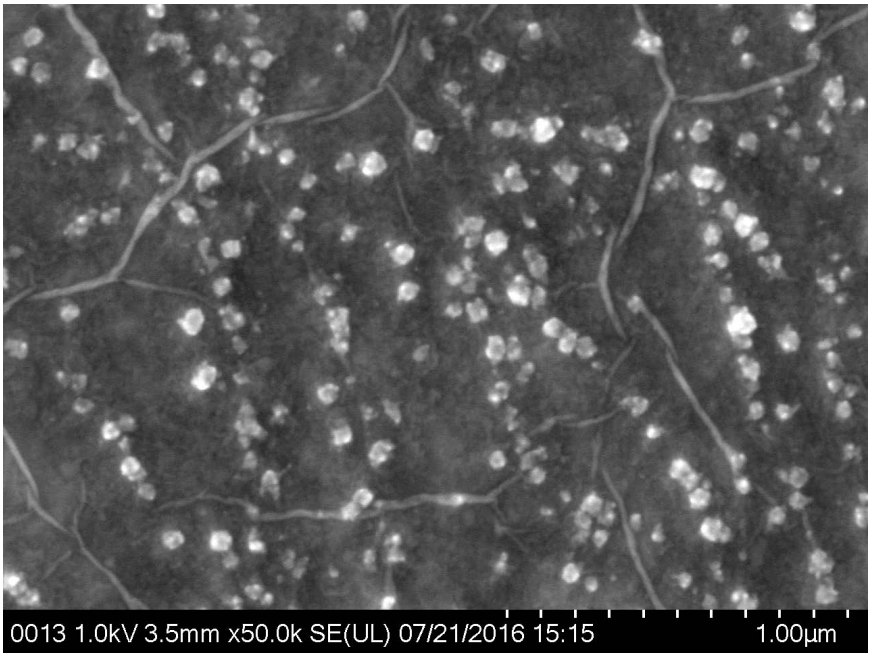

(b) BN on few layer C-face graphene retains pleated structure, even after BN deposition

Figure 4.9: 4 of 4. Surface morphology of 15 nm thick LAD deposited BN on epitaxial graphene surfaces exhibiting selective area growth of 2D BN films with pleated morphology on graphene surfaces.

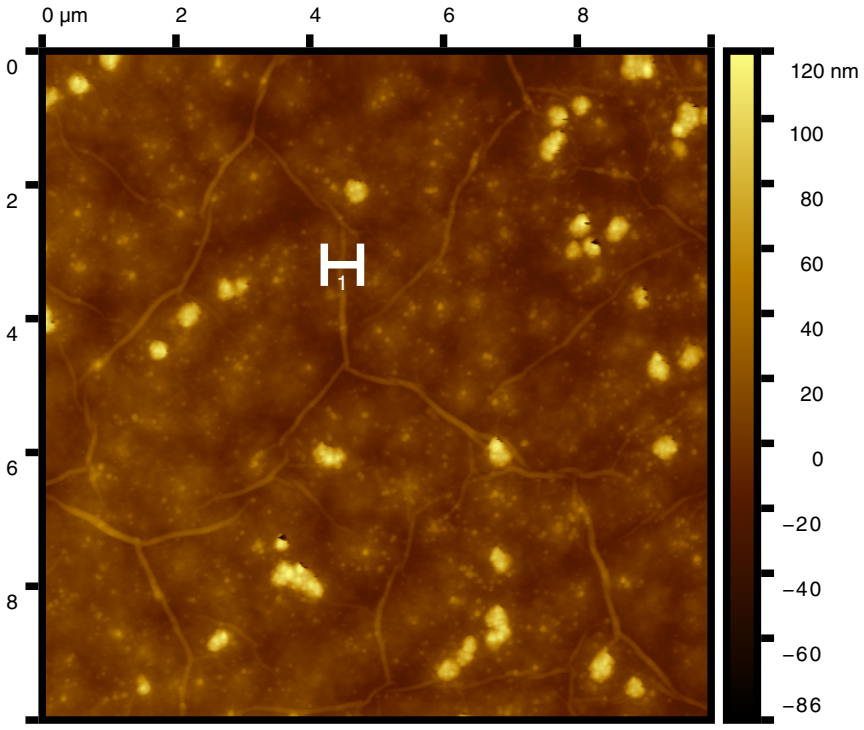

(a) Contact AFM image of pleated hBN surface on monolayer graphene.

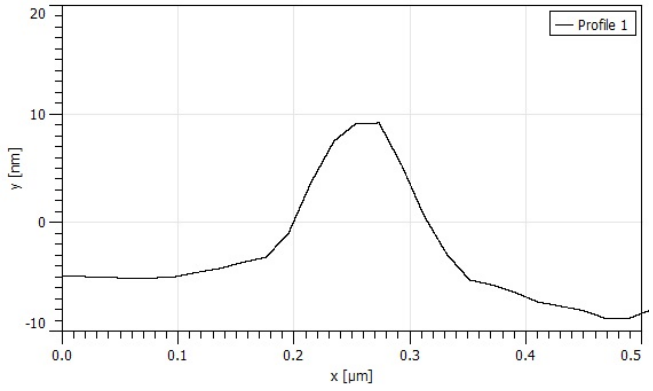

(b) Profile of the line selected in (a).

Figure 4.10: The pleated surface of the hBN film is due to the negative in-plane CTE of 2D materials. The heights of the pleats are 5-15 nm, corresponding to the expected CTE induced strain. Sample S0119-53JG76

With BN thicknesses above 20 nm, the concentration of crumpled granules on pleated regions increased. Due to the large strain in the system, there is a critical thickness, above which, the film transitions to favoring granule formation. The increasing stress within the layers overcomes the weak van der Waals interlayer force and causes the BN sheets to crumple. No sp^3 hybridized boron is identified in XPS, even on highly granular surfaces, which offers support for a crumpled paper morphology. The size of the granules can be related to the mobility of the surface with high mobility surfaces presenting large granules. Similarly, the areal density of granules can be considered. The granule size, d, varies such that $d_{graphene} > d_{bufferlayer} > d_{SiC}$, as shown in Figure 4.11. Graphene surfaces exhibit higher mobilities and, thus, lower nucleation densities; SiC offers many nucleation sites and lower mobilities. The nucleation site density can be clearly seen by depositing gold on an overgrown graphene nanoribbon at elevated temperatures, as shown in Figure 4.12. As such, higher substrate temperatures are expected to facilitate 2D growth on buffer layer and SiC surfaces by providing thermal energy to overcome potential wells on the surface.

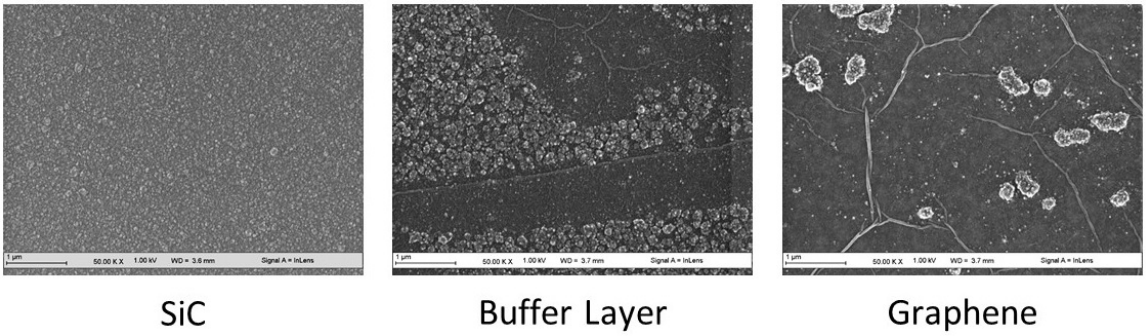

Figure 4.11: The surface granule size, d, can be correlated to the surface nucleation density and mobility of SiC, buffer layer, and graphene. As expected, the nucleation density is highest on the SiC surface and lowest on graphene.

Incomplete films reveal the lateral, epitaxial growth front, as shown in Figure 4.13. The nucleation density is very low on monolayer graphene, with nucleation sites separated by up to 1 μm. The lateral growth rate is approximately 1.5 atoms per half cycle. This is larger than the 1 atom/half-cycle expected from an ideal LAD growth due to an over-saturation of

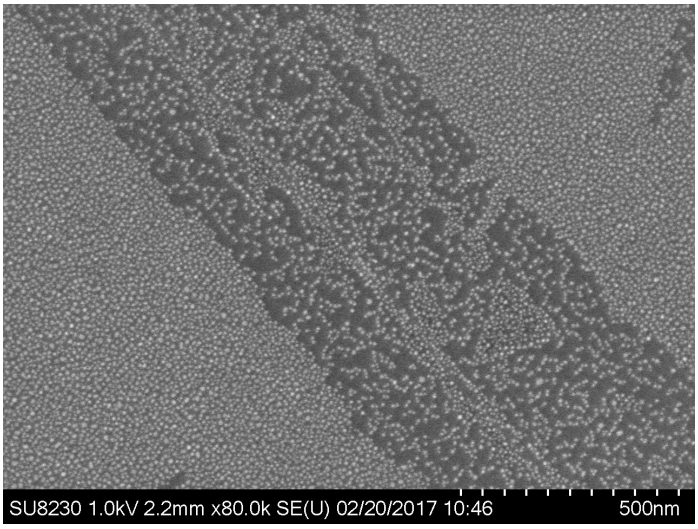

Figure 4.12: The density of nucleation sites is related to the roughness and bonding character of the surface. Graphene exhibits very low roughness and no dangling bonds which significantly reduces nucleation density compared to buffer layer. Here, the density is clearly demonstrated by gold particles which were deposited in a UHV evaporator on a 500 °C overgrown graphene ribbon.

boron. Further process optimization is expected to resolve this problem.

The dendritic structure and symmetric hexagonal symmetry are also indicative of excess boron concentration and low processing temperatures. Higher processing temperatures are known to improve crystallinity by improving surface diffusion. Dendrites form under diffusion limited conditions. The equilibrium crystal shape for BN is a truncated triangle. This stems from the broken symmetry compared to graphene, which exhibits hexagonal grains, due to the non-equivalent lattice sites containing boron and nitrogen. As a significant number of nitrogen sites are occupied by boron atoms, the relative difference is reduced resulting in hexagonal structures.

Boron Nitride Chemical Structure: X-ray Photoelectron Spectroscopy

X-ray photoelectron spectroscopy (XPS) is a powerful tool to probe surface chemistry and composition. The low energy photoelectrons can only escape from the top few nanometers, giving very good surface sensitivity. XPS functions by illuminating the sample with X-rays,

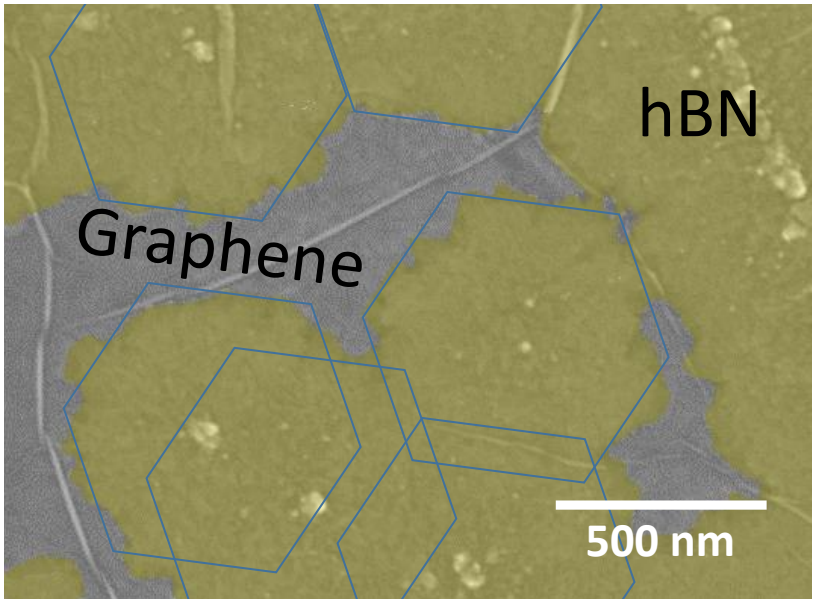

Figure 4.13: Oriented hexagonal growth fronts are visible in incomplete films after 1200 cycles. The growth rate was approximately 1.5 atoms per half cycle. The distance between nucleation sites on monolayer epitaxial graphene is up to 1 μm. Sample 49JG43-S0123.

typically monochromatic Al K-alpha ($E_{photon} = 1486.7$ eV). This ejects core electrons. The kinetic energy, $E_{kinetic}$ of the electrons is then detected and the binding energy, $E_{binding}$ of the electron can be determined, such that

$$E_{binding} = E_{photon} - (E_{kinetic} + \phi) \tag{4.1}$$

where ϕ is the work function of the detector. The process is described in Figure 4.14.

This elastic process describes the primary peaks in an XPS spectra. However, loss mechanisms can also occur, and are critical to understanding sp^2 bonded materials. The $\pi - \pi^*$ transition, which is present in both graphene and hBN, is about 6-9 eV. This loss in kinetic energy causes a satellite peak at 6-9 eV higher in binding energy. The presence of these peaks is one of the best ways to chemically differentiate sp^2 and sp^3 BN as the B1s and N1s peaks are found at nearly identical positions. In sp^3 BN, no satellite peaks will be observed.

Figure 4.15 shows selected XPS spectra taken from a 10 nm hBN film on epitaxial

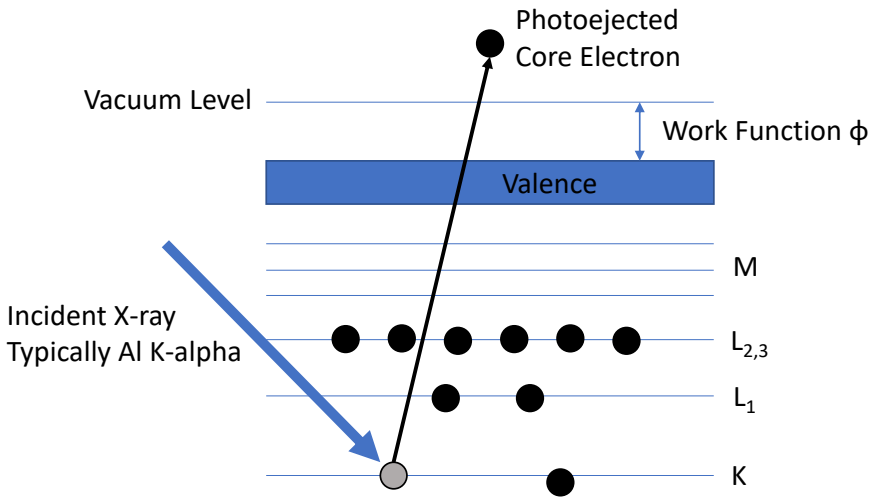

Figure 4.14: In XPS, the kinetic energy of photoejected core electrons is measured. The binding energy can then determined as described in Equation 4.1.

graphene after Ar sputtering on a Thermo K-alpha XPS. Once the adventitious surface carbon is removed, hBN, graphene, and SiC XPS signatures are identified, as shown in Figure 4.16. The B 1s and N 1s peaks each present one significant component, centered at 190.8 eV and 398.5 eV, respectively, corresponding to literature values for sp^2 hybridized BN.[8, 135, 167] Satellite peaks, occurring at 198 eV and 406 eV are present for both B and N, respectively, due to the $\pi - \pi^*$ transition which are not present in cubic (sp^3) BN.[168] The peaks do not shift throughout the thickness of the film indicating homogeneous chemical structure. Comparing the normalized areas, after Shirley background subtraction, yields a B:N of 1:0.81, indicating a nitrogen deficiency. The C 1s spectrum reveals two dominant components: graphene at 284.5 eV and SiC at 283.3 eV. Buffer layer could not be identified, likely due to intercalation. The Si 2p spectrum shows only a pure SiC contribution at 100.8 eV. The oxygen spectrum (not shown) is primarily composed of a small concentration of metal oxides at 532.3 eV, likely SiO_2 and B_2O_3. Granular BN films were also analyzed and reveal sp^2 bonding, supporting the crumpled sheet morphology.

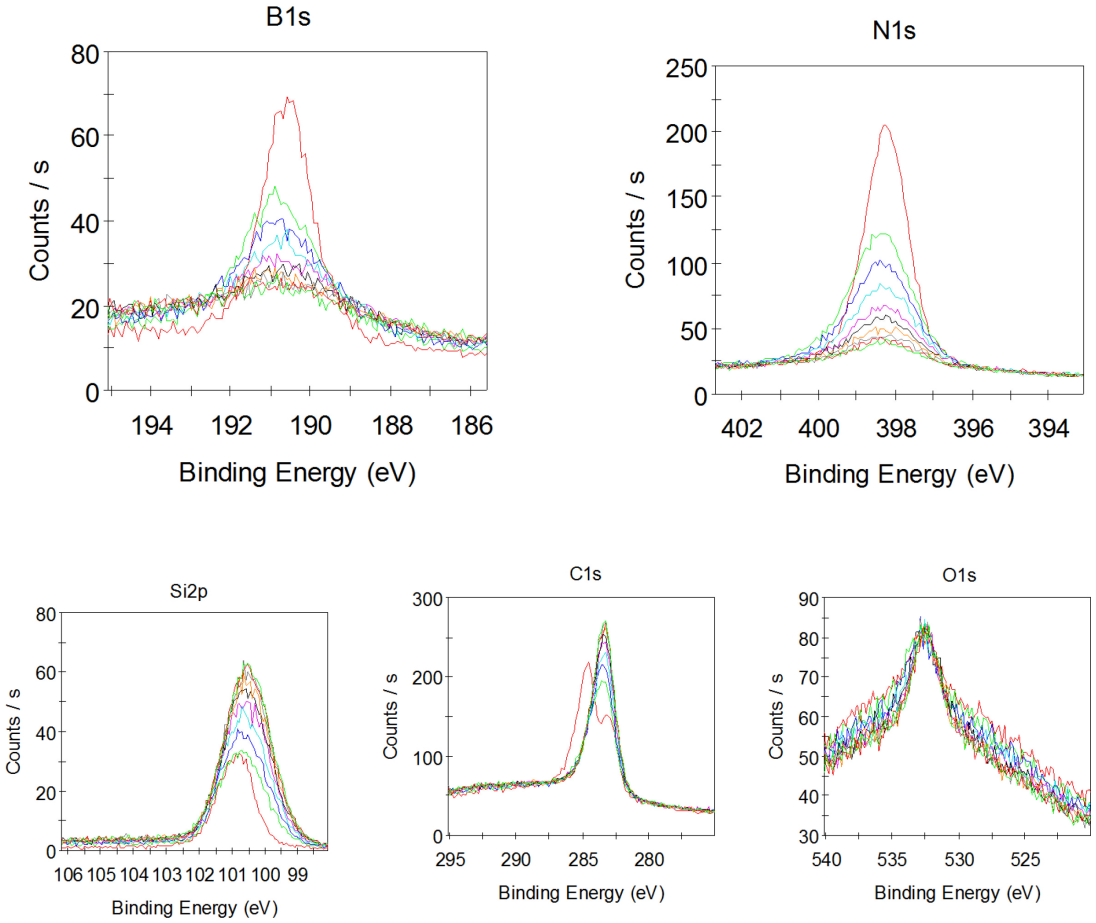

Figure 4.15: XPS depth profile taken from a 10 nm thick BN on monolayer graphene film. The B (191 eV) and N (398 eV) spectra are indicative of sp^2 bonding with no other significant component present. The slight shift in the B and Si spectra after the first etch cycle (red) is due to the removal of surface oxides. The significant shift in the C spectra is due to the removal of adventitious carbon.

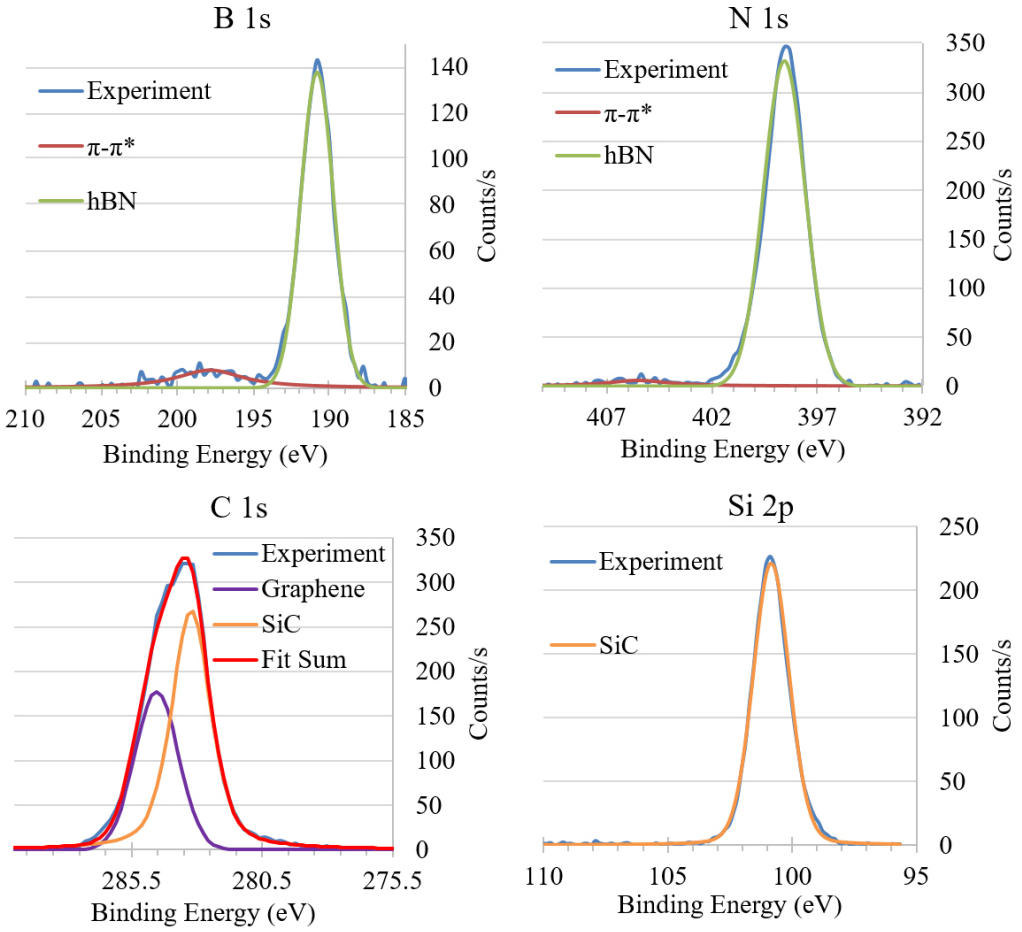

Figure 4.16: Ion sputtered XPS spectra after removal of the Shirley background showing decomposed contributions from BN, graphene, and SiC.

Boron Nitride Chemical Structure: Raman Spectroscopy

Raman spectroscopy, performed in Loiseau's lab (ONERA-LEM, Chatillon, France), of the first few layers of hBN on graphene reveals a strong E_{2G} peak at 1370.6 cm^{-1} with FWHM of 47.5 cm^{-1}, as shown in Figure 4.17. The 2D graphene peak occurs at 2735 cm^{-1} confirming that the peak is related to the hBN. The bulk hBN film reveals a large background signal, which is likely due to the excess boron content in the film and defect states in the gap due to the nitrogen deficiency (see Figure 4.24). Similar broadening has also been observed for BCN alloys.[169] The band gap of BN is about 6 eV which should not be overcome by the 532 nm (2.33 eV) laser.

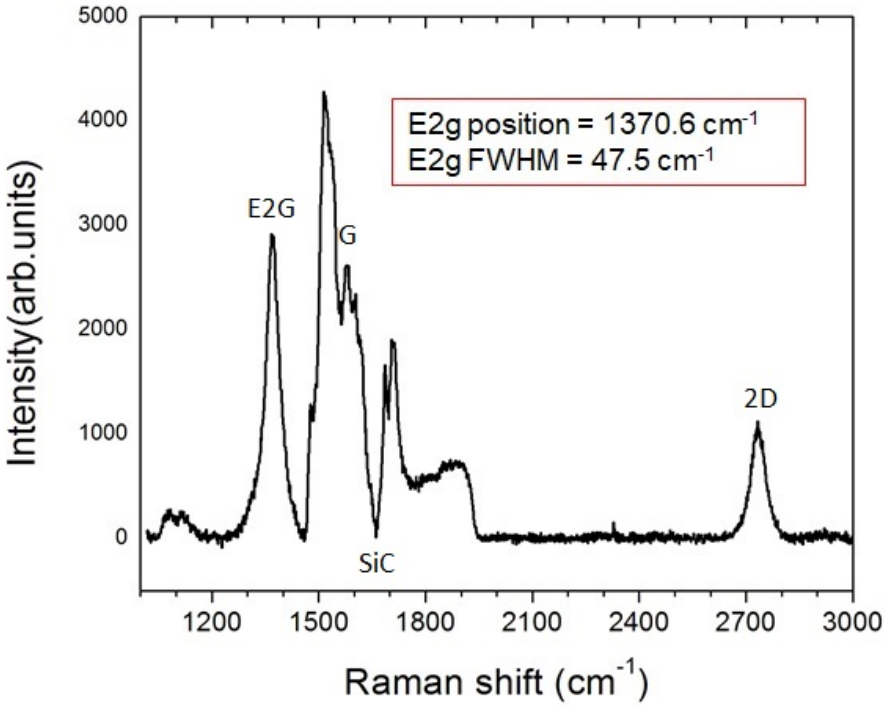

Figure 4.17: Raman of the a few layer hBN flake after exfoliation of most of the hBN film reveals a strong E_2G peak with FWHM of 47.5 cm^{-1}.

Boron Nitride Crystal Structure: X-ray Diffraction

High resolution X-ray diffraction (HRXRD) scans, as shown in Figure 4.18, confirm highly ordered hBN layers. The hBN (0002) peak is located at 25.5° 2θ corresponding to an interlayer spacing of 3.50 Å. This represents a 4.8% expansion over bulk hBN (3.33 Å), likely due to rotational stacking faults, residual intercalated hydrocarbons, or induced stress from cooling. Despite the expansion, the rocking curve was measured and found to be 0.04° indicating a highly oriented stack of BN layers. The interplanar spacing of graphene is nearly identical to BN, so to confirm that the source of the peak was from the BN deposition, scans were taken prior to BN growth which do not show a graphene peak for monolayer up to few layer graphene due to the small cross section. XRD spectra were also taken of granular BN films on SiC and did not exhibit any features besides the SiC substrate peaks confirming that the pleated morphology is a characteristic of 2D BN layers. The granular BN morphology of these films may be composed of crumpled-up BN sheets as the XPS signals from both granular and layered BN are identical indicating sp^2 bonding for both the 2D and 3D BN morphologies, similar to the ammonia borane study.

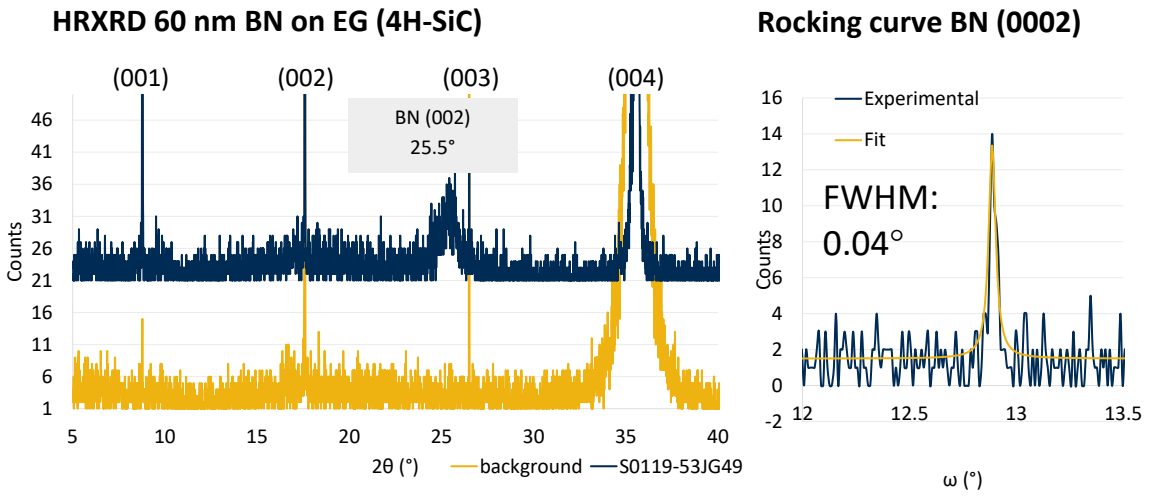

Figure 4.18: HRXRD showing hBN growth on epitaxial graphene sample. The background scan shows that the peak is not due to the single layer of graphene on the surface. The BN(0002) rocking curve is indicative of a highly oriented sample. Sample S0119-53JG49.

Boron Nitride Crystal Structure: Transmission Electron Microscopy

Cross-sectional scanning transmission electron microscopy (STEM), energy dispersive X-ray spectroscopy (EDX), and electron energy loss spectroscopy (EELS) studies, performed by Gilles Patriarche (Figure 4.19) and Annick Loiseau's lab (Figure 4.21), present a clear layered hBN film. The substrate for the sample images was few layer Si-face graphene on 4H-SiC. Lamella with thicknesses of 70-80 nm were prepared by David Troadec via focused ion beam (FIB) milling with a gallium beam following deposition of 50 nm of amorphous carbon to protect the hBN and graphene from ionm bombardment and to reduce delamination. The images were taken along the $\langle 11\bar{2}0 \rangle$ zone axis. EDX was performed to determine the extent of Ga-ion damage, differentiate graphene and hBN, and to examine the chemical uniformity of the film.

The high resolution images, presented in Figure 4.19a-c, confirm the van der Waals solid structure. The stacking order of the BN layers can be seen in Figure 4.19b, confirming hBN. The spots within the hBN layers are AA' stacked, as opposed to ABC for rhombohedral BN. No grain boundaries were observed at the graphene-hBN interface over 1.5 μm of cross sectional scans, with each imaging spanning approximately 75 nm, as shown in Figure 4.20. Atomic planes within the hBN film have interlayer spacing of 3.6 Å, which is in agreement with the XRD results. This spacing is expanded with respect to bulk hBN (3.33 Å), likely due to partial intercalation from the high temperature hydrogen growth environment, induced strain, and stacking faults. Faint lines between some of the bright hBN layers indicate the presence of these faults. Further, atomic positions are also visible in the graphene layers, as seen in Figure 4.20b, confirming that the hBN grew epitaxially. It is also worth noting that the first graphene layer is offset from the topmost SiC layer by 4.5 Å, similar to the 4.2 Å reported for quasi-freestanding epitaxial graphene following hydrogen intercalation.[170]

The bonding character of the hBN film was probed with EELS at various distances from the graphene surface as shown in Figure 4.21a. The spectra, shown in Figure 4.21b, reveal

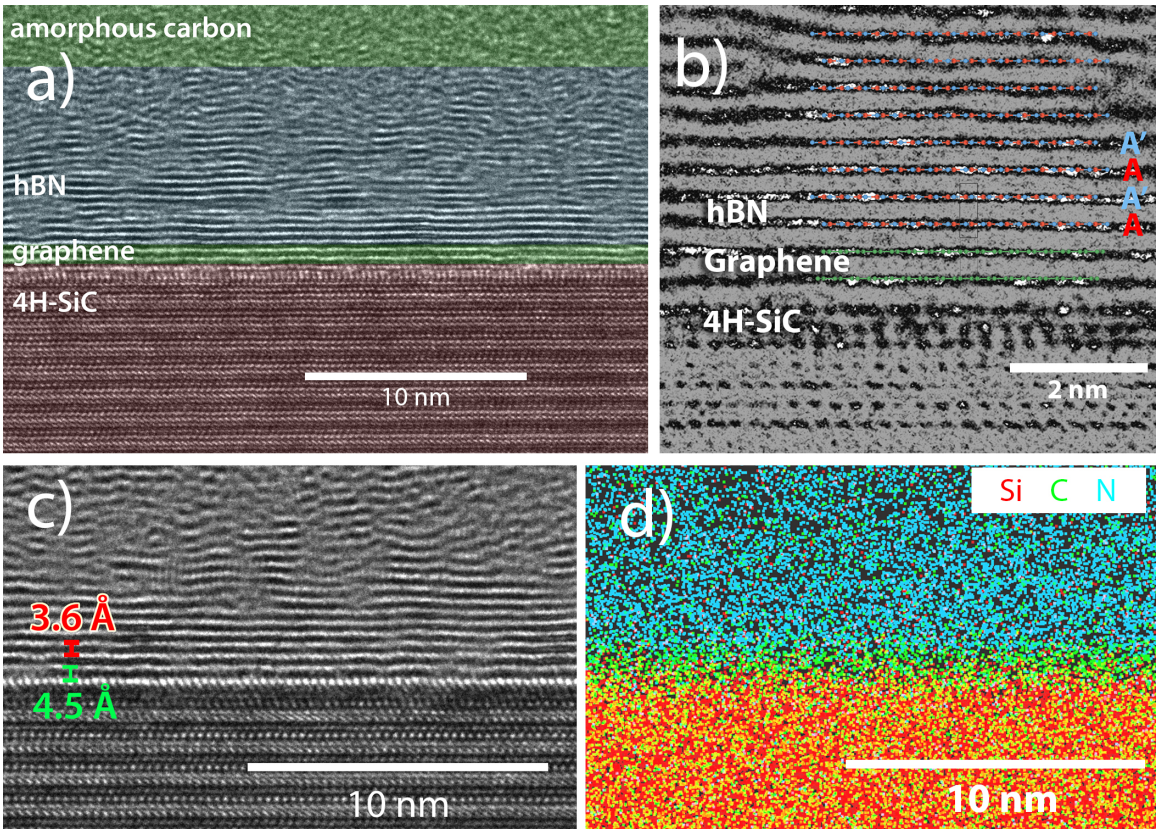

Figure 4.19: Cross-sectional STEM of BN on few layer Si-face epitaxial graphene taken along the $\langle 11\bar{2}0 \rangle$ zone axis. a) High resolution image depicting coherence in the hBN layer. The disorder present at the interface of the BN and amorphous carbon protection layer is due to an insufficient carbon protection layer which resulted in Ga ion damage as seen in EDX (Figure 4.22). The graphene layer identification is taken from the EDX analysis. b) The stacking order is AA', corresponding to hBN. c) The interlayer spacing of the hBN layer is 3.6 Å. The spacing of the first graphene layer is expanded to 4.5 Å, likely due to hydrogen intercalation of the buffer layer. The stacking order of the hBN can be seen, confirming hBN. d) EDX analysis shows the intact graphene interface, damage due to the FIB preparation, and uniform BN composition. The imaging was performed by Gilles Patriarche.

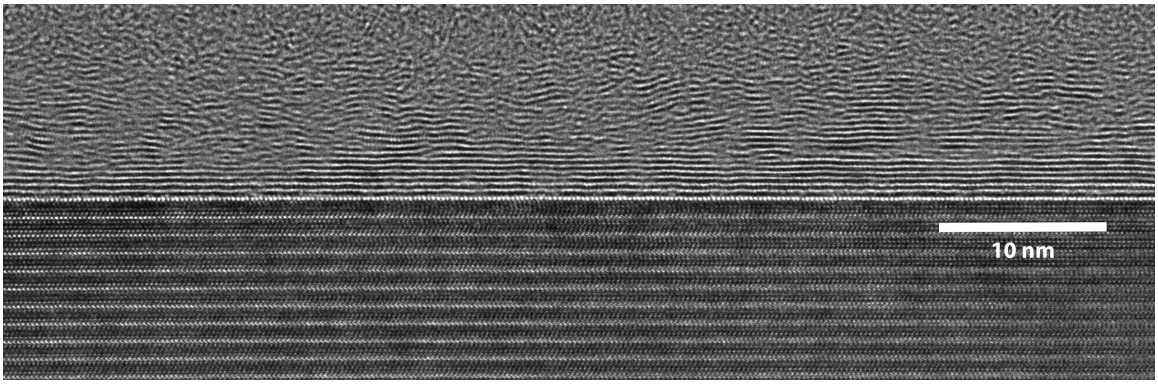

(a) The critically important graphene-hBN interface exhibits no defects over at least 70 nm.

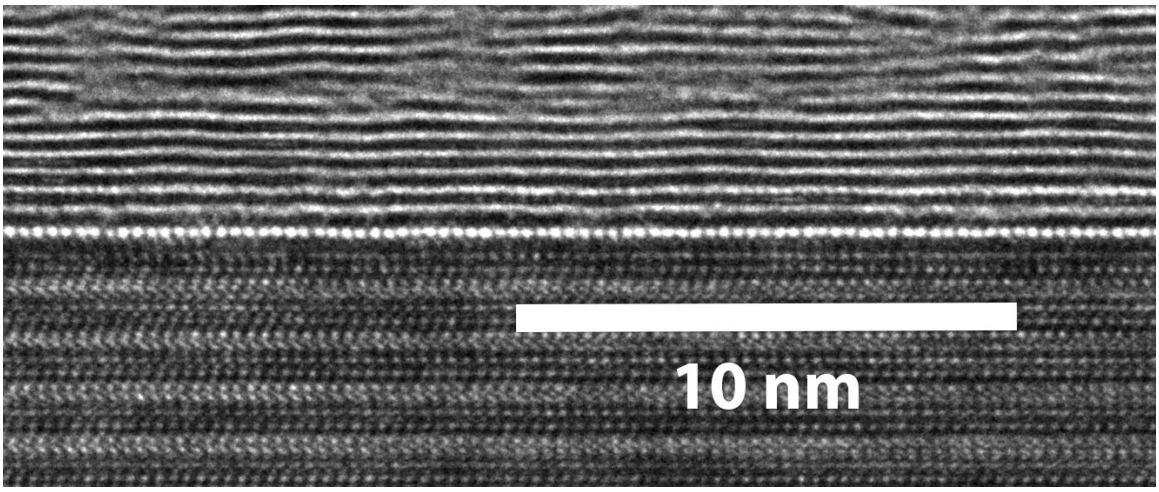

(b) Zoom of full image showing atomic positions in the SiC, graphene (first 2 layers), and hBN film, confirming epitaxy of all three layers.

Figure 4.20: Cross sectional TEM reveals a pristine graphene-hBN interface and epitaxial growth. Imaging performed by Gilles Patriarche.

a sharp π^* peak at 191.1 eV, which is indicative of sp^2 hBN at the graphene interface.[171, 172] The hBN film begins to deteriorate after about 7 nm from the graphene surface (blue dot) as oxygen and carbon are incorporated into the film. This is confirmed via an EDX profile shown in Figure 4.21c It is not possible to differentiate damage due to the FIB preparation from inherent defects in the film.

The graphene layer was confirmed to survive via EDX analysis, shown in Figure 4.19d. A thin region composed entirely of carbon overlaps with the first 2-3 atomic layers, corresponding to the buffer layer and 1-2 layers of graphene on the Si-face. These layers are intact with spacing consistent with EG. The nitrogen EDX signal is consistent throughout the hBN layer confirming uniform chemical composition throughout the hBN film. Boron does not provide sufficient contrast against the background signals due to its low atomic number. A high gallium and carbon content were observed in the top of the hBN film corresponding to the region where the hBN film appears to deteriorate 7-10 nm from the graphene surface. This degradation is at least partially due to an insufficient amorphous carbon protection layer for the FIB lamella preparation. While the interface is coherent along the length of the scan, a fast Fourier transform of the top layers revealed a reduced coherence length of 5 nm.

Boron Nitride Crystal Structure: Low Energy Electron Diffraction

Low energy electron diffraction (LEED) probes the out-of plane diffracted electrons and gives information on the in-plane atomic arrangement. Typical electron energy is between 20-200 eV. The low energy often limits penetration depth to a few atomic layers. This is makes LEED particularly useful in the epitaxial graphene system as surface reconstructions can be readily observed. If the incident and scattered electron wave vectors are k and k', respectively, the condition for constructive interference, and, therefore a diffraction spot, is

$$(k' - k) \cdot d = 2\pi \times integer \tag{4.2}$$

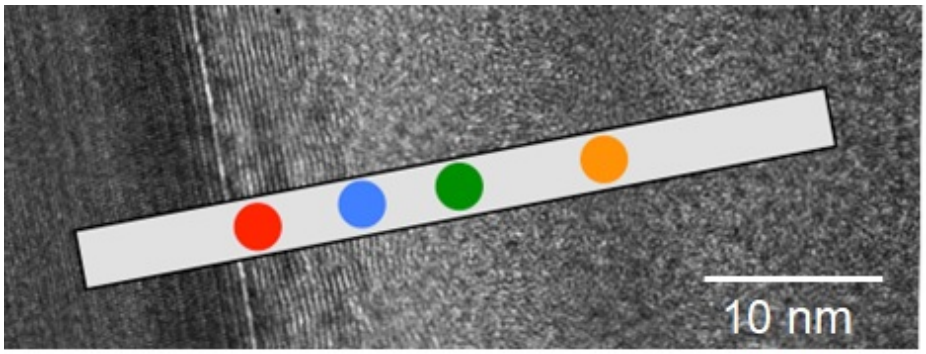

(a) EELS analysis was conducted at various distances from the graphene-hBN interface. Sharp hBN plane are visible near the graphene surface.

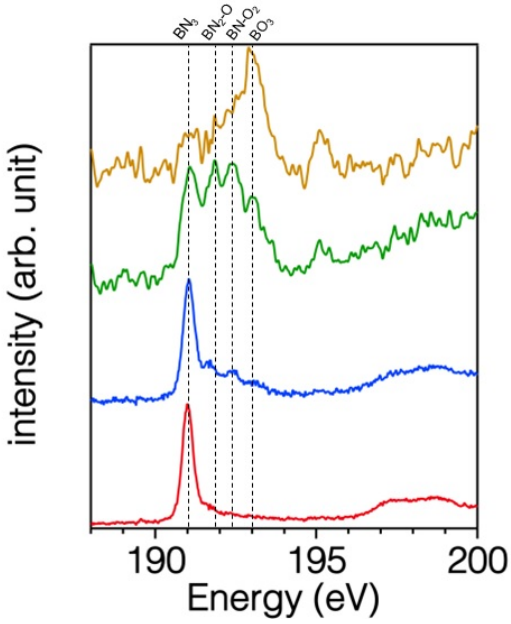

(b) EELS spectra shows degrading hBN film with distance from the graphene interface. It is not possible to separate the contribution from the FIB preparation from any inherent disorder in the film.The colors refer to specific locations shown in Figure 4.21a.

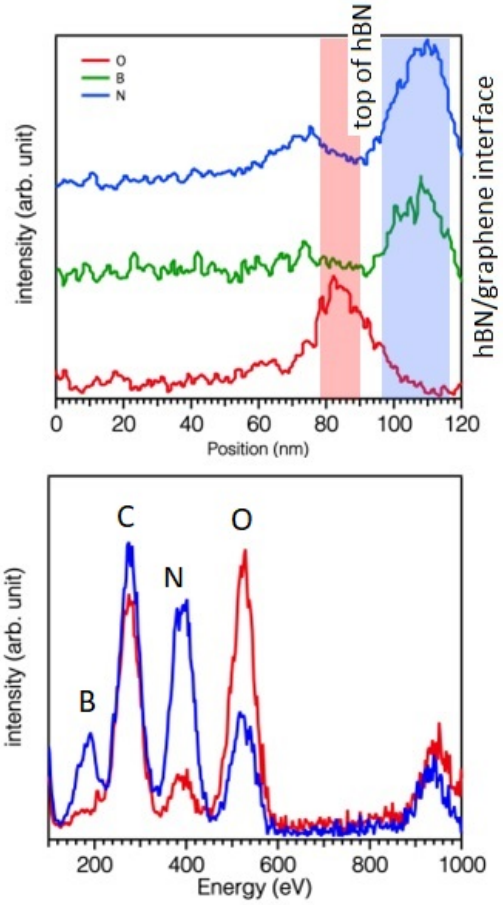

(c) EDX profile confirming that there is no significant carbon or oxygen content within the film. The graphene/hBN interface is located at 120nm. The energy spectra of the red (disordered hBN film) and blue (crystalline hBN film) highlighted regions are shown.

Figure 4.21: EELS analysis shows a sharp π^* peak at 191.1 eV which is consistent with sp^2 BN. EDX confirms that there no significant carbon or oxygen content in the crystalline hBN film near the graphene interface. This study was performed in Annick Loiseau's lab.

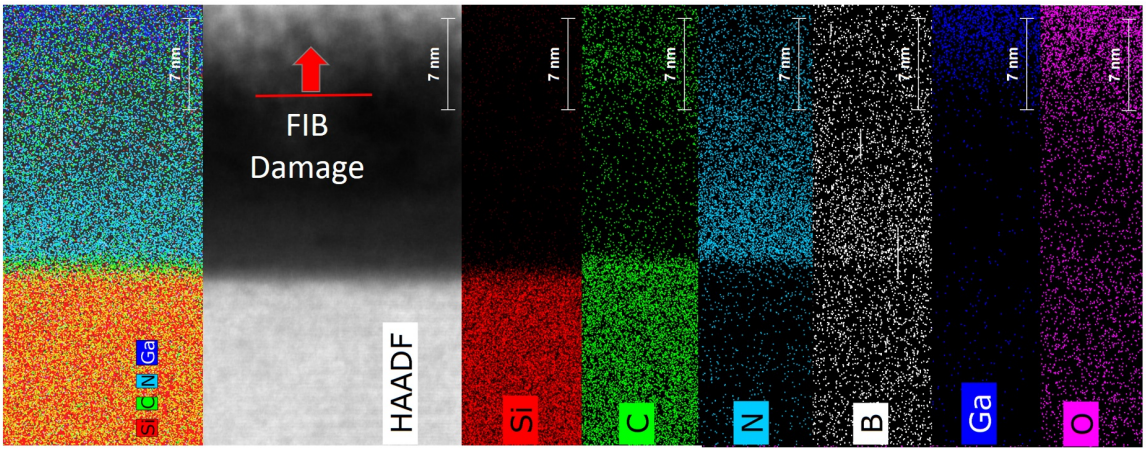

Figure 4.22: Cross sectional EDX analysis reveals uniform BN composition and a sharp interface between the graphene layer and hBN film. The carbon protection layer was insufficient, so Ga damage from the FIB preparation is seen at the top of the film.

where d is all lattice vectors in the surface plane, such that

$$d = n_1 a_1 + n_2 a_2. \tag{4.3}$$

The vectors a_1 and a_2 define the lattice on the surface. The Bravais lattice of the surface can be determined from the diffraction pattern.

LEED was performed in the lab to probe the underlying graphene structure. Figure 4.23 shows the LEED pattern generated by 227 eV electrons. The high energy was necessary to probe the hBN, graphene, and SiC simultaneously. Two hexagonal patterns rotated by 30° are evident and correspond to the lattices of graphene and hBN and SiC. The buffer layer reconstruction is not visible, either due to hydrogen intercalation or, more likely, the short coherence in the buffer layer due to the BN over-layer. If randomly oriented BN grains were present, a ring would be observed near the graphene spot radius. This is especially impressive considering that the LEED spot size is a few mm.

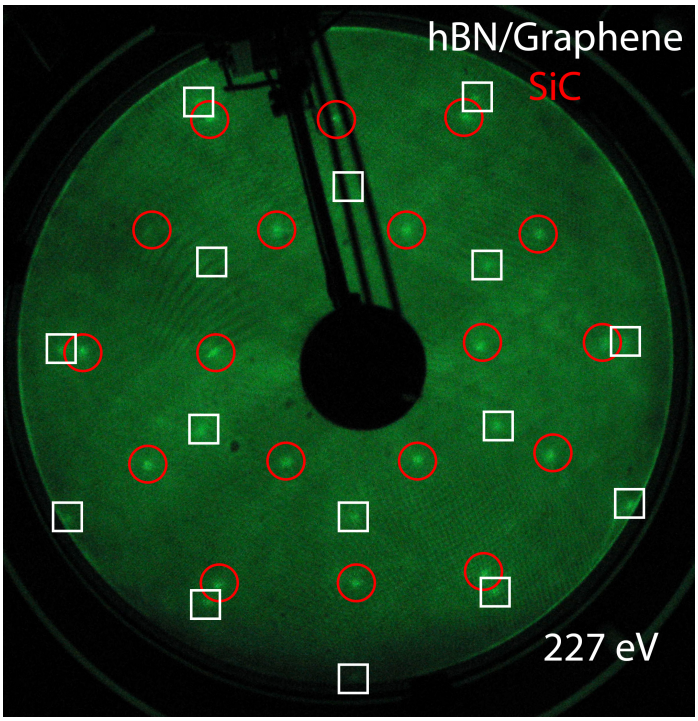

Figure 4.23: LEED taken at 227 eV of a Si-face monolayer graphene sample coated in 15 nm BN. The graphene and hBN spots coincide and SiC spots are clearly visible. No rings are visible, confirming the rotational orientation of the hBN film. No buffer layer signal is visible either due to the short coherence in the buffer layer or due to hydrogen intercalation. Sample S0129-53JG79

Graphene Quality after hBN Coating

The quality of the underlying graphene was examined post BN deposition via Raman spectroscopy, LEED, and electronic transport studies. The BN film exhibits significant broadening, masking the underlying graphene Raman signature. Due to the extremely weak interlayer bonding between BN and graphene, the BN layer could be mechanically removed leaving behind clean graphene surfaces, which are more strongly bonded to the SiC. Raman spectroscopy was performed on these exposed surfaces. Monolayer graphene samples were analyzed to confirm that the D peak, which is related to defects in the graphene layer (1375 cm^{-1}) did not appear due to the high temperature hydrogen environment or chemical attack from the NH_3, as it is known to attack graphite. Figure 4.24a shows the Raman spectra line map across the boundary between the BN film and epitaxial graphene surface, showing minimal change in the graphene as a result of BN deposition. The 2D peak position remained at 2715 cm^{-1} and the FWHM broadened from 45 to 56 cm^{-1}, which is typical for hydrogen intercalated monolayer Si-face EG. There is a possibility that a damaged graphene layer could have been removed with the BN film. The same experiment was done on overgrown graphene nanoribbon samples to determine the extent of hydrogen intercalation of the buffer layer. As seen in Figure 4.24b. No graphene peaks were present in the spectra taken on the exposed terraces, indicating that hydrogen intercalation was inhomogeneous.

Van der Pauw resistance measurements on monolayer Si-face epitaxial graphene coated with 20 nm of BN reveal P-type doping of the graphene. The sheet resistance was found to be $172\,\Omega/\square$. The resulting carrier density was 1.5×10^{14} cm^{-2} with mobility of 70 cm^2/V·s. Virgin epitaxial graphene monolayers exhibit similar sheet resistance, but with carrier concentrations of $10^{12} - 10^{13}$ cm^{-2}.

Due to the linear band structure of graphene, the product of the observed charge density and mobility can be correlated to sheet resistance. These results are comparable to charge densities of 10^{13} cm^{-2} and mobilities on the order of 1,000 cm^2/V·s which corresponds

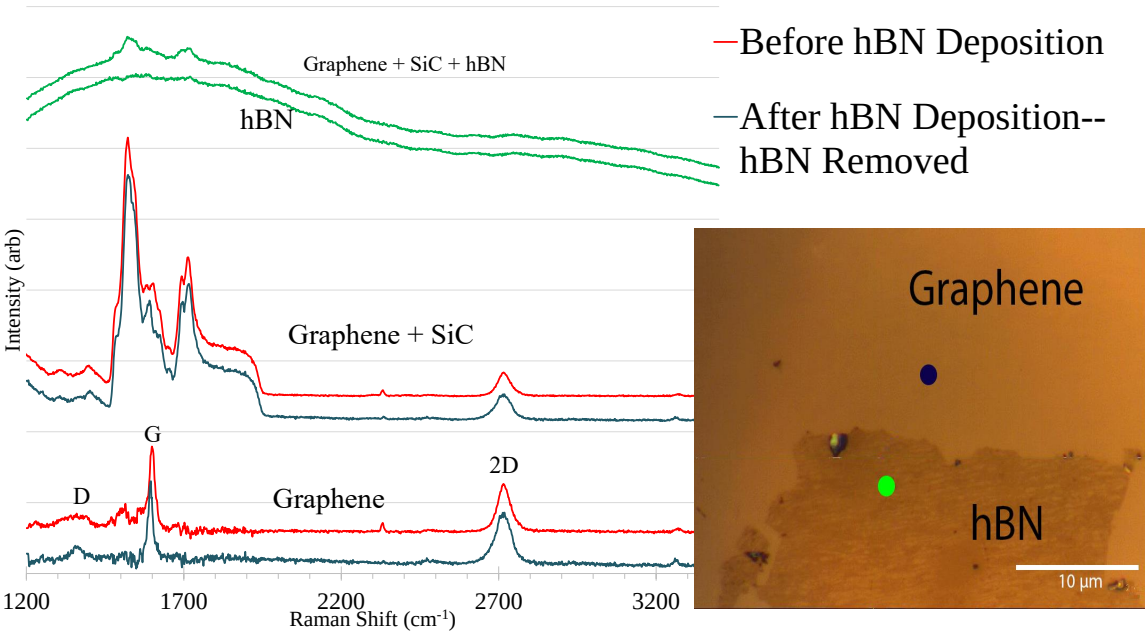

(a) Raman spectra taken from areas covered by BN and from the clean underlying graphene show that the graphene is not damaged during the deposition process. The slight broadening of the 2D peak is indicative of bilayer formation due to hydrogen intercalation of the buffer layer.

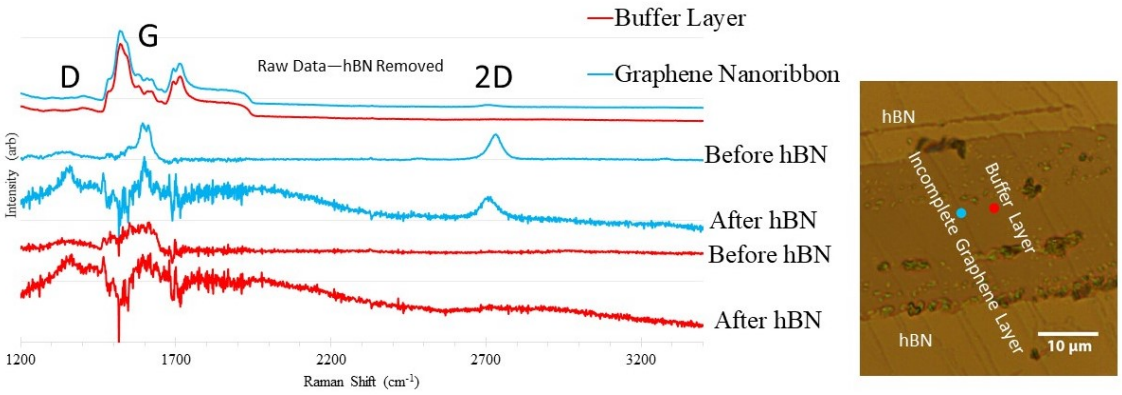

(b) Raman spectra showing that the buffer layer was not widely intercalated during the hBN growth process as no 2D peak develops on the buffer layer covered terraces. The background after hBN exfoliation is due to incomplete removal of the BN film.

Figure 4.24: Raman spectra taken before and after hBN deposition. After exfoliating the hBN film, the underlying graphene could be accurately probed.

to high quality, monolayer epitaxial graphene layers, indicating that the low mobility in graphene transport is due to adsorbate doping and not damaged during hBN deposition. A different sample exhibited carrier densities of $3.7-6.6\times10^{13}$ cm^{-2} from 4 K to 300 K, again with P-type doping. There was no observed change after annealing at 420 K, indicating that the hBN layer provided good protection from environmental contaminates. Future experiments will seek to modulate the induced charge density in graphene by controlling the stoichiometry of the hBN layer and modulate the BN composition to induce in-plane static electric fields.

The Fermi level of the graphene can be determined from the carrier concentration. The density of states, D_{2D}, is linearly proportional to energy,

$$D_{2D}(E) = \frac{g_s g_v \left|E\right|}{2\pi(\hbar v_F)^2} \tag{4.4}$$

where g_s is the spin degeneracy (2), g_v is the valley degeneracy (2), and v_F is the Fermi velocity (10^8 cm/s). The carrier density, n, can then be found by integrating over the filled states,

$$n_{P-type}(T) = \int_{-\infty}^{0} D_{2D}(E)(1 - f_{FD}(E,T))dE \tag{4.5}$$

where f_{FD} is the Fermi-Dirac distribution: $(e^{\frac{E-E_F}{k_B T}}+1)^{-1}$. Thus, Fermi level corresponding to the above mentioned charge density is -0.71 eV at 4 K. The literature says that there is a 10 meV divergence from linearity at 0.75 eV, justifying disregard for sub-bands [173].

Conclusion

Cyclic precursor injection onto hot, high mobility substrates yields a unique, row-by-row growth mode. Here, the lateral atomic deposition process was identified while exploring traditional processing space for 2D heterostructure production. Vertical, epitaxial heterostructures of hBN/graphene/SiC were produced with a pristine graphene-hBN interface. The processing space afforded by a commercially available Aixtron showerhead reactor

combined with a refractory substrate and high quality epitaxial graphene surface enables large epitaxial 2D heterostructures via LAD, whereas ALD of 2D materials grown on metal foils results in polycrystalline films with nanoscale grains.

4.3 Development of Lateral Atomic Deposition Technology

Further study is needed to optimize the LAD process prior to device fabrication. Specifically, the growth temperature, TEB:NH_3 ratio, and post growth annealing should be examined to produce stoichiometric hBN films. Following, the stability of BN films in harsh environments and electric fields will need to be studied to determine the efficacy of hBN as a passivation layer, gate dielectric, and tunneling barrier for epitaxial graphene devices. Finally, process times must be reduced for industrial applications.

Further characterization and optimization are required to understand the growth mechanism and improve the quality of hBN on epitaxial graphene. The preliminary results were obtained from a sequential deposition of TEB and ammonia which limits vapor phase polymerization and can provide highly controllable growth dynamics. The particle formation on the surface of the films, induced strain, and the presence of defect bands, as evident by Raman and lack of signal from low temperature cathodo-luminescence, indicate that there is room for structural and chemical improvement. The high charge density of the graphene indicates high adsorbate doping from the hBN. Also, hydrogen intercalation should be avoided or reversed for hBN integration into graphene nanoribbon-based nanoelectronics.

4.3.1 Deposition Mechanism

High temperature CVD processes completely decompose metalorganic precursors on the hot surface (>1000 °C). The carbon tails in TEB strongly decompose above 800 °C, as demonstrated by a sharp increase in carbon content with substrate temperature in Figure 4.25. As such, the growth of hBN via cyclic introduction of TEB and ammonia can largely consider the movement and reactions of atomic species on the surface.

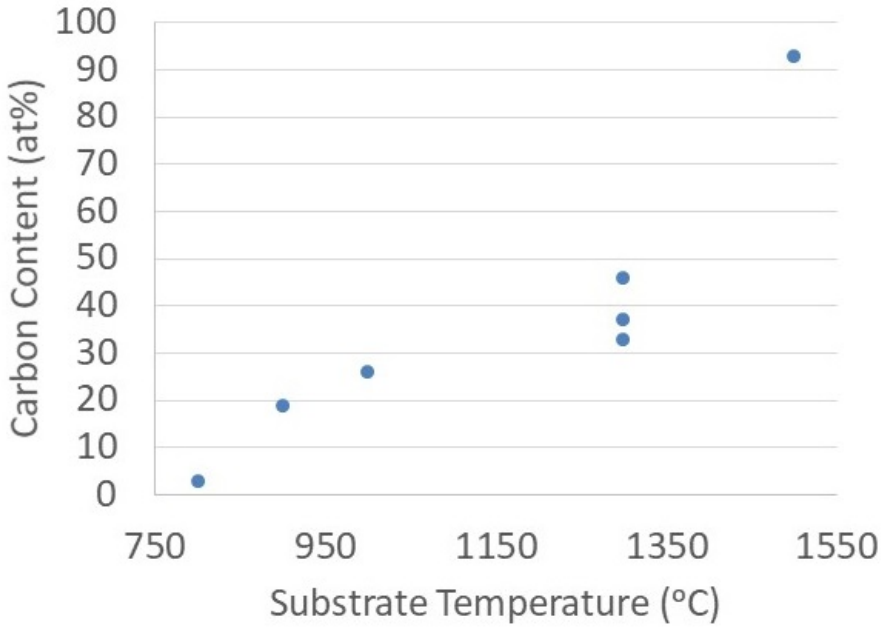

Figure 4.25: The ethyl tails in TEB strongly decompose at temperatures in excess of 800 °C. This decomposition introduces large amounts (6:1 C:B)of carbon into the BN film which must be chemically removed.

Ammonia requires higher temperatures for efficient cracking. As shown in Figure 4.26, substrate temperatures below 1000 °C result in very little incorporated nitrogen. Once temperatures exceed 1200 °C, there is sufficient ammonia cracking to to produce BN.

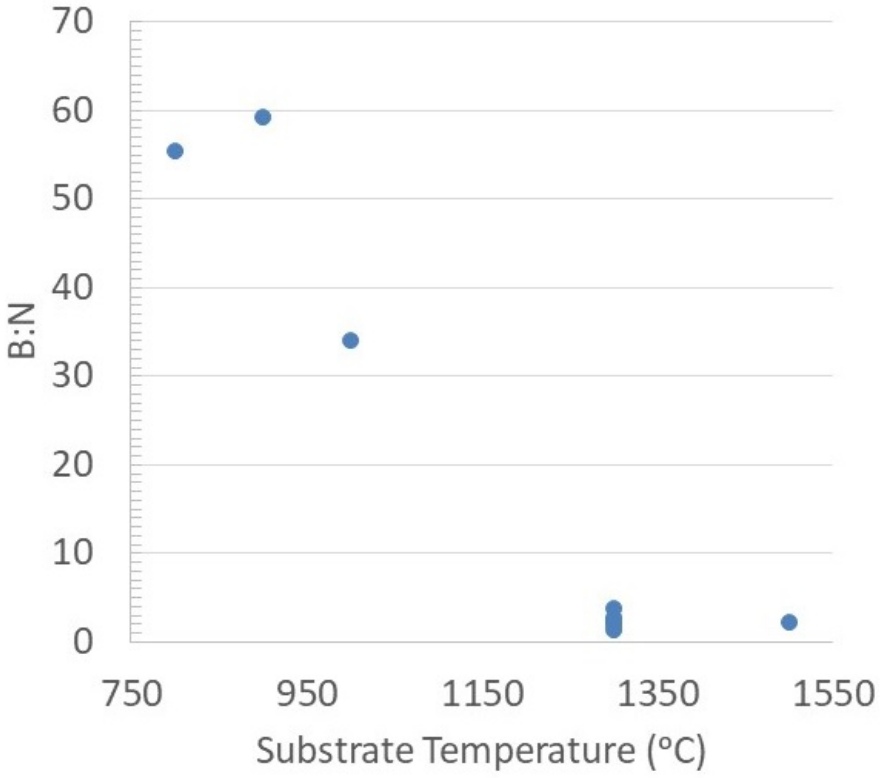

Figure 4.26: Ammonia requires substrate temperatures in excess of 1200 °C to incorporate sufficient nitrogen into the BN film.

Hydrogen is an effective carbon etcher due to production of methane (CH_4) vapor. The effect of hydrogen was compared to inert atmospheres, as shown in Figure 4.27. Under inert atmosphere (He or high vacuum) carbon content increased with temperature due to increasing decomposition of the TEB ethyl functional groups. In contrast, a hydrogen atmosphere showed a sharp reduction in carbon content as the substrate temperature exceeded 1000 °C.

The hBN growth rate on graphene was observed to be about 1/3 that as was observed on sapphire.[126] As described in Equation 1.28, Levy flight conditions occur for species with weak bonding to the surface, such as atomic species on graphene. Levy flight, not only

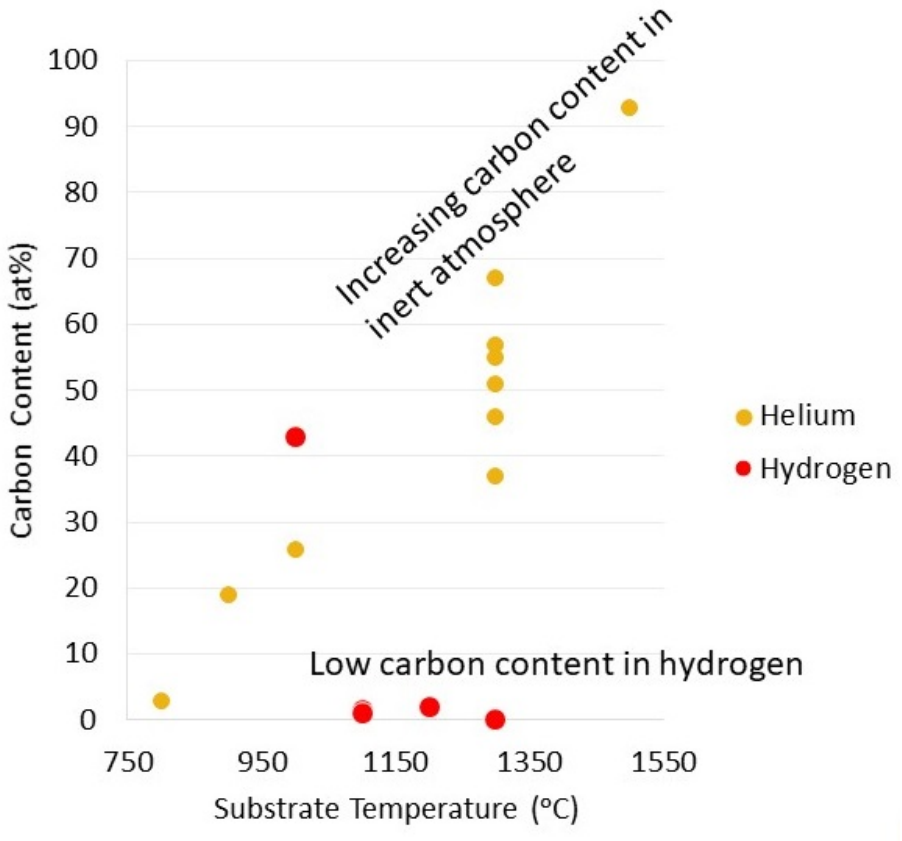

Figure 4.27: Carbon content was sharply reduced under high temperature hydrogen atmosphere compared to inert atmosphere. Under helium or high vacuum conditions, carbon content increased with substrate temperature due to TEB functional group decomposition. Hydrogen effectively etches nanoscale graphitic domains, reducing the carbon content to a few at% after the substrate temperature exceeds 1000 °C. The series at 1300 °C investigated ammonia dosage, another source of hydrogen. Increased ammonia dosage reduced carbon content.

enables long mean free paths (high adatom mobilities) but also enables species to glide over step edges and other reactive sites. Under these conditions, the mobile species can remain unpinned on the surface for enough time that they are likely to desorb, slowing growth rates. Therefore, a balance between long mean free paths, as is desired to uniformly coat larger structures, and growth rate must be determined. Higher temperatures will encourage faceted crystal growth, but growth rate is expected to sharply decline.

4.3.2 Stoichiometry

Additional runs must be conducted to understand both the nucleation and growth dynamics to improve the stoichiometry of the hBN film. In the growth process, the III/V ratio is controlled by the relative doses of the TEB and ammonia cycles. Dosing tests need to be conducted to determine the optimal III/V ratio to achieve the correct stoichiometry and maximize processing efficiency. The nitrogen deficiency should be corrected by increasing the V:III ratio or varying the temperature for each half cycle. As the metalorganic molecule decomposes well below the substrate temperature, it is likely that the process was overdosing TEB, resulting in several rows of boron per cycle which could not be completely nitridized. Thus, a reduced TEB dosage should be included in the increased V:III ratio. A higher temperature for the ammonia pulse will also create more active nitrogen, but would require an induction heater for sufficiently high cycle time to be practical.

The structure of the hBN film must also be improved, specifically after the first few layers and on the surface. To eliminate vapor phase reactions, sufficient purging time must be allowed between cycles and care must be taken to reduce the effects of precursor decomposition in the high temperature reactor. Nucleation studies will then be conducted to determine proper surface seeding and nucleation temperature dependence to reduce nucleation delay and aid in the growth of monolayer BN films.

Once proper growth conditions are established, drawing from the LPCVD results, high temperature annealing under high vacuum, forming gas, and nitrogen should be studied

to improve crystallinity and reverse intercalation. Graphene devices coated in BN can then be exposed to various environments, including air, oxygen, water vapor, and organic compounds at various temperatures to assess the efficacy of BN for protecting the graphene transport. These proposed studies will provide several pieces of information:

1. Can stoichiometric BN layers be deposited with an LAD?
2. Does the BN retard further SiC graphitization and can hydrogen intercalation be reversed?
3. Is BN a suitable high temperature dielectric for graphene?
4. Can the induced charge density in the underlying graphene be modulated with BN stoichiometry and can lateral composition gradients induce in-plane static electric fields?

4.3.3 Nucleation Control

Nucleation site control for self-assembled nanostructures is critically important. In typical processes, nucleation most often occurs at defect sites on the substrate including step edges, screw dislocations, vacancies, or impurities. With the exception of step edges, these are dispersed randomly which while suitable for blanket coatings, is not suitable for producing large arrays of self-assembled nanostructures.

In the epitaxial graphene system, there are two advantages: pristine, nearly defect free surfaces and sharp material interfaces. The pristine graphene surfaces largely eliminate island nucleation. On monolayer graphene sheets, nucleation sites have a density of < 1 μm^{-2} at a deposition temperature of 1270 °C, as seen in Figure 4.13. For nanostructures, no nucleation sites will be present besides the edges. Further, the lateral interfaces between graphene, buffer layer, and SiC act as heterogeneous nucleation sites. While the SiC and buffer layer surfaces do provide nucleation sites, the critical graphene surfaces support a

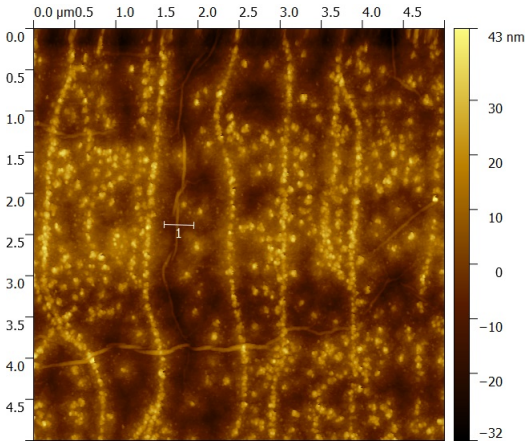

(a) On monolayer graphene films, the underlying topography reduces the local nucleation barrier leading to BN clusters decorating the step edges.

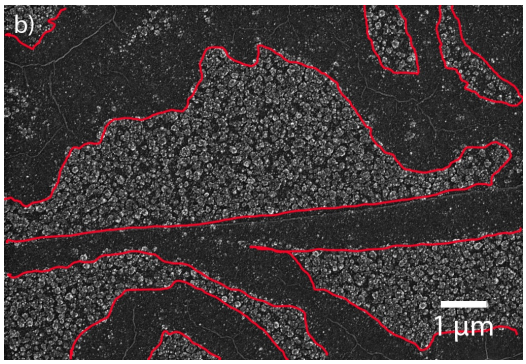

(b) The interface between graphene and buffer layer serves as a nucleation site for LAD processes. For small graphene domains, island nucleation is unlikely to occur. The graphene ribbon is outlined in red.

Figure 4.28: Surface topography and material interfaces serve as preferred nucleation sites for LAD processes. This make LAD ideally suited to coat nanostructures.

single lateral growth front. This important feature will enable controlled growth of lateral films with the option for atomically precise composition and material changes.

Graphene nanoribbons are an ideal platform for exploring this technology. Sharp interfaces between 2D BN layers and granular BN films are seen at the interface between graphene and buffer layer. As the technology progresses, patterned nucleation edges will need to be developed. Atomic layer etch (ALE) is the etching analog to ALD. Selective ALE processes enable direct etching of nanostructures with high precision and are a clear starting place for creating sharp nucleation edges. Lateral atomic etch chemistries must still be developed for 2D materials. The strong bonding may prove problematic, especially for etching sp^2 bonded materials, such as graphene and hBN. In such cases, pre-patterned structures, such as those used for graphene nanoribbon production could be used.

Precise control over the number of layers is also critical for electronic layers. Temperature is a well known control to transition between island nucleation and lateral growth.[174, 175] Higher temperatures enable adatoms to overcome the larger energy barrier associated with jumping a step edge, thus favoring equilibrium crystal shape. In the case of 2D mate-

rials this will favor lateral growth for low precursor fluxes. Therefore, a change in growth temperature can be used to tune the film thickness. An alternative method would be to reduce the precursor flux as grain size grows to ensure that stable nuclei are unlikely to form on the terrace.

4.3.4 High Speed LAD

Similar to the slow vertical growth rates in ALD, the previously presented LAD work has been conducted under slow lateral growth conditions. The cycle times used in this study are on the order of a few seconds, but as several thousand cycles are needed to cover an area of a few hundred nanometers (1 Å per half cycle), growth times were several hours resulting in only a few layers. Industrial applications would desire a high speed process.

Owed to the high temperatures accommodated by the graphene, SiC, and hBN used in this study, it is conceivable to ramp up the cycle rate to 10-100 Hz. High temperatures enable fast desorption of unused precursors and byproducts. This is far faster than ALD processing and will enable processing times on the order of a few seconds for monolayers. The following will present an overview of the underlying physics and a proposed apparatus to explore high speed LAD technology for industrial applications.

As described in Equation 1.28, the feature size to be coated will determine the feasibility of high speed LAD. Fortunately, nanostructures present ideal dimensions for high speed coating and, as such, a feature length scale, L, of 100 nm will be assumed. The deposition zone will be defined as an area of L^2. Smaller length scales relax the equipment requirements. Larger areas, such as several microns, demand very tight control over the maximum flux.

In order to guarantee that adatoms find their way to an edge before nucleating a cluster, only a single mobile adatom must be present on a deposition zone. Assuming a random walk, which will give a lower bound, a hopping frequency of 10^{14} Hz, and an average hopping distance of 10^6 lattice sites (assuming 1 Å per site and a random walk distance

of $\sqrt{N}$), a surface diffusion time of 10^{-8} s is found. A half cycle must have a dwell time longer than this.

Surface limited growth is not possible with metalorganic precursors due to decomposition of the ligands at high temperatures. As such, with current metalorganic precursors, the boron dosage must result in only partial edge saturation and the second half-cycle must provide a species which cannot over-saturate, such as nitrogen. It is convenient to consider fluxes in $\mu\mathrm{mol/s}$ which is controlled by a dosing system, so for the sake of discussion of a research scale apparatus, the total deposition area of the beam is on order of 1 cm^2. The maximum flux is then simply the product of the number of deposition zones and the maximum flux per zone (number of concurrent adatoms/hopping time). For the case of $L = 100$ nm, the maximum deposition flux is $1.66\,\mu\mathrm{mol/s}$. Naturally, the width of the molecular beam can be widened to relax this requirement.

From a practical standpoint, the total pulse time must also be reasonable. The source pressure and valve geometry determine the timing for the desired dosage. The flow through an orifice, Q (Nm^3/s), can be estimated by:

$$Q = \frac{1}{3600} * 4.17C(\frac{d_0}{4.654}^{\ 2})p_1(1 - \frac{\frac{p_1-p_2}{p_2}}{3F_\gamma x_T})\sqrt{\frac{\frac{p_1-p_2}{p_2}}{T_a + 273.15}} \tag{4.6}$$

where C is the discharge coefficient, p_1 is the pressure of the source, p_2 is the pressure of the chamber, T_a is the temperature, F_γ is the specific heat ratio, x_T is the differential pressure factor, and d_0 is the orifice diameter. For reasonable values for miniature high speed valves (d_0 =0.3 mm, C =0.25), and partial pressure of TEB at 20 °C (47 Torr), injecting into a vacuum chamber will yield a flow rate of about $0.5\,\mu\mathrm{mol/s}$ which is below the maximum limit established above. This gives pulse times of 76 $\mu\,\mathrm{sec}$ which is within the range of the pulse valves discussed in the next section. If large 1 $\mu\mathrm{m}$ features are desired, the pulse time drops to 7.6 $\mu\,\mathrm{sec}$ which will demand moving to a chilled or dilute precursor. Very small structures will require a larger valve to maintain high frequency operation.

The temperature dependence of the vapor pressure of TEB is determined by

$$\frac{P_1}{P_2} = \frac{H_{vap}}{R}\left(\frac{1}{273+T_2} - \frac{1}{273+T_1}\right) \tag{4.7}$$

where P and T are the pressure and temperatures of interest and H_{vap} is the heat of vaporization. For TEB, H_{vap}=36.9 $\mathrm{kJ/mol}$ and the vapor pressure at 25 °C is 53 Torr.

Supersonic Jet Epitaxy

When a high pressure source is exposed to a low pressure environment through a small aperture, a supersonic jet can be formed, as shown in Figure 4.29. Under such conditions, the velocity of the jet can approach a maximum, v_∞, of

$$v_\infty = \sqrt{\frac{2\gamma R T_0}{m(\gamma-1)}} \tag{4.8}$$

where γ is the heat capacity ratio given by C_p/C_v, R is the gas constant, T_0 is the nozzle temperature, and m is the molecular weight of the gas species.

As the jet expands, the pressure approaches the surrounding pressure and the flow becomes turbulent at the Mach disk. The size of the Mach disk, D_m will be related to the uniformity of deposition. It is clear that uniformity will be a challenge when operating with jets as opposed to effusion cells, as $D_m/D < 1$ under most pressure differential regimes.[176] However, due to the tight radial delivery of precursor, the use of precursor will be reduced and costs will be lower. Further, deposition onto the walls will be limited, reducing concerns related redeposition of reaction by-products.

Uniformity can be problematic in supersonic jets as the flux distribution is proportional to $\cos^x\theta$ where θ is the angle from the center of the source, as shown in Figure 4.30. For supersonic jets, the distribution is strongly dependent on θ such that $4 < x < 22$.[177, 178, 179] Typical effusion cells vary with $\cos\theta$. The higher values of x tend to arise from seeded jets as the heavier species tend to be focused tighter than in a pure jet.[180]

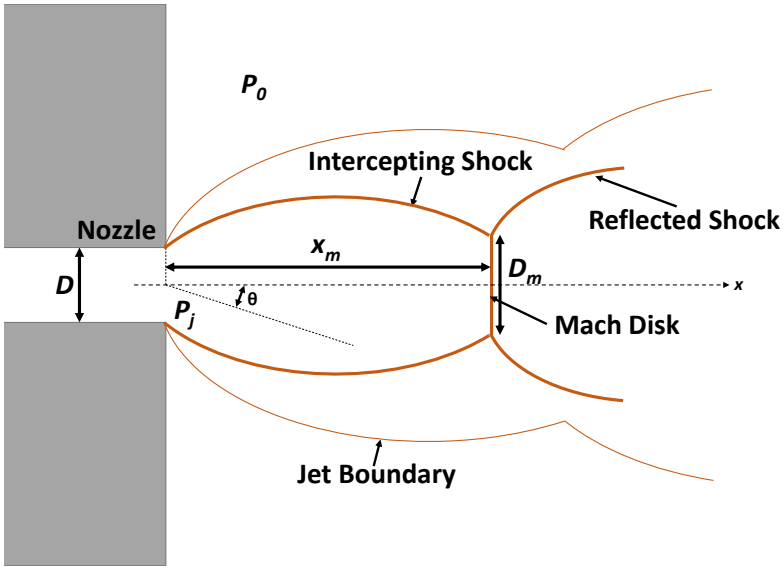

Figure 4.29: When a high pressure source, P_j, expands into a low pressure environment, P_0, through a small orifice of diameter, D, a supersonic jet can form. As the jet expands, the Mach disk, at distance x_m from the nozzle represents the region where P_j becomes comparable to P_0 and turbulent flow occurs.

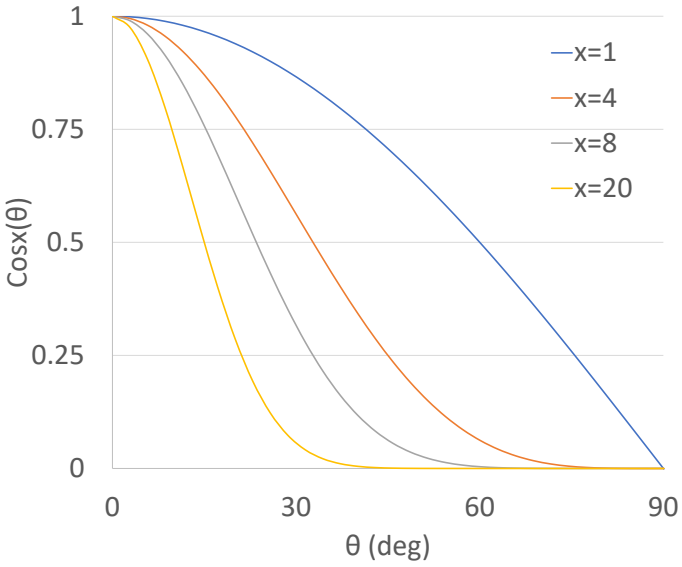

Figure 4.30: The angular dependence of beam density is proportional to $\cos^x(\theta)$, where $4 < x < 22$ is typical for jets, while $x = 1$ for effusion cells.

High fluxes demand high pumping speeds. As the ambient pressure increases, the jet will experience interference which can accelerate the transition to turbulent flow and introduce impurities into the beam. In order to limit the flux, small orifice diameters and low gas pressures are employed. For the case of high speed pulses, the pumping rate will also dictate the cycle time.

One advantage of employing supersonic jets is the ability to modulate the kinetic energy of precursor species and to achieve much higher energies than in effusion cells. The adiabatic expansion as molecules exit the nozzle into an evacuated chamber leads to significantly fewer collisions and provides a narrow energy spread.[181] The maximum kinetic energy, E, of the molecules in a pure gas is determined by

$$E = \frac{\gamma}{\gamma - 1} RT. \tag{4.9}$$

It has been shown that with increasing kinetic energy, the probability of adsorption also increases. By utilizing kinetic energy to supplement the thermal energy needed to overcome activation barriers such as ES barriers or chemisorption barriers, the substrate temperature can be reduced compared to other deposition techniques. It follows that the chemisorption temperature dependence is also reduced.[182] This offers two advantages for LAD technology:

1. Lower processing temperatures can be employed to retard graphitization, reduce intercalation, and limit decomposition of less stable 2D materials, such as the transition metal dichalcogenides.

2. The high kinetic energy leads to a dissociative pathway with limited temperature dependence (reduced carbon content)

Combined, these two points greatly expand the application space for pulsed supersonic jet LAD technology.

One way to tune the kinetic energy of the jet beyond geometric constraints is to seed the precursor in a carrier gas. If the carrier is of a lower molecular weight than the precursor, the kinetic energy, E_{p^∞}, will be increased, as described by

$$E_{p^\infty} = \frac{m_p}{< m >} < C_p > T_0, \tag{4.10}$$

where m_p is the precursor molecular weight and $< m >$ and $< C_p >$ are the average molecular weight and heat capacity of the mixture, respectively. This relation leads to kinetic energies of 1-10 eV which is 1-2 order of magnitude over thermal kinetic energy and is comparable to chemical bond strengths.[183, 184, 181] As an example, diluting in He compared to H_2 improved growth uniformity from $x = 20$ to $x = 8$.[185] One drawback to seeding a lighter carrier jet is a tighening of the angular spread leading to reduced uniformity.

Pulsed supersonic jets of trimethylgallium (TMG) have been explored with continuous AsH_3 sources for homoepitaxial growth of GaAs(100).[186, 184, 187, 188] Low concentrations of TMG (1%) in H_2 were necessary to access sub-monolayer per pulse control. Pulse widths were a few ms separated by 1 s purge. A further benefit to the high kinetic energy (4 eV) when heavily diluted was a reduction in carbon content due to improved dissociation of the TMG molecule.[184]

Equipment Specifications

It is clear that pulsed supersonic jet epitaxy holds promise for LAD technology. Short pulse times, seeded jets, reduced thermal activation, and improved purity compared to CVD processes lead to the following equipment considerations and specifications. Figure 4.31 outlines the plans for construction of a high speed, pulsed jet epitaxy system. The system is readily scalable to larger substrates, additional precursor injection ports, plasma sources, as well as in situ characterization.

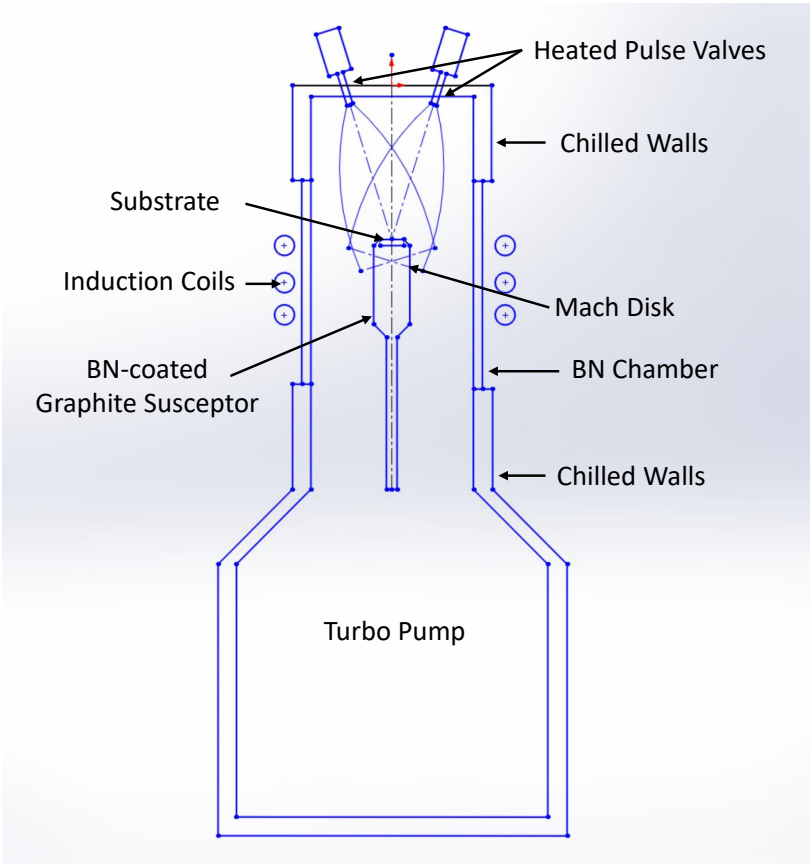

Figure 4.31: Schematic for a fast LAD system based on pulsed supersonic jet epitaxy. Multiple, high speed precursor valves inject gases into a carrier jet. The system is inductively heated and high vacuum capable.

Vacuum System

Tight control over the ambient conditions including background gases, redeposition, and base pressure is demanded for jet stability.

While the supersonic jet ensures that precursor molecules will arrive at the surface in a pure environment, they demand a low background pressure. As the ambient pressure, P_0 approaches the pressure within the jet P_j, turbulent flow occurs at the Mach disk. The Mach disc is located at x_m from the nozzle of diameter, D. This mixing will introduce ambient molecules into the jet and contamination into the film. As such, the location of the substrate should lie at $x < x_m$. Several experimental[189, 176, 190] and theoretical[191, 192] studies estimate x_m as

$$x_m = 0.67D\sqrt{\frac{P_j}{P_0}}. \tag{4.11}$$

Further, as precursors decompose once they interact with the surface, the high pressure of a supersonic jet will ensure that there is only a single interaction.

To maintain the jet stability, a high speed turbo pump (> 2000 l/s) backed by a mechanical pump is recommended to achieve base pressures $< 10^{-7}$ Torr and maintain constant P_j/P_0. Exhaust gases should be run through a gas reactor column to neutralize toxic fumes.

Precursor Sources: Boron

High purity precursors are vital, but even more vital is choosing chemistry which undergoes the optimal chemical pathways. Different precursor molecules can drastically affect the morphology of the heterostructure, even if the same material is grown. This is particularly true for 2D materials which can be readily intercalated with foreign molecules, even at moderate temperatures. Keeping with the example of BN-epigraphene, vapor and liquid boron sources and various methods of nitrogen production will be discussed, but similar arguments hold for other materials as well.

Typical sources of boron include metalorganics, such as trimethylboron (C_3H_9B; TMB),

triethylboron ($C_6H_{15}B$; TEB), and simple hydrides, such as diborane (B_2H_6). Most MOCVD and ALD processes use the metalorganic precursors. The vapor pressures are reasonable and can be modulated with temperature, dilution can be achieved through a bubbler, reasonable growth temperature are accessible, and growth rates are excellent. The added ligands are used in ALD processes to enable the self-limiting growth regime. Due to these reasons and ease in scaling MOCVD systems up to high volume manufacturing, metalorganic precursors have attracted much attention.

However, for BN growth, relatively high temperatures ($> 1000°$C) are required which is sufficient to break the C-B bond. At growth temperatures below 700 °C, self-limiting growth has been observed, but at the cost of reduced crystallinity. In general, with sufficient dosage control, thermally decomposing the precursor is not a problem; however, as growth temperatures rise, carbon from the ligands can also be incorporated into the film and released hydrogen begins etching graphene edges and intercalating beneath graphene layers leading to a blurred interface. Hydrogen will preferentially etch carbon as opposed to BN by producing volatile CH_4, until the temperature rises such that methyl also starts to decompose. The crystallinity of BN has been shown to improve up to temperatures of 1800 °C[193], so precursors which do not contain carbon (or any foreign species) would be preferred. The same conclusion has been reached for industrial UHV CVD systems, such as those for depositing strained silicon. Simple hydride precursors, such asSiH_4, GeH_4,and B_2H_6, are strongly preferred.

Diborane is a vapor source without any carbon-containing tails. While this will completely eliminate carbon incorporation, it will limit access to self-limiting conditions. As such, tight control over dosing must be maintained. Under-dosing the boron will be most effective for stoichiometric producing BN films. If bottom-up fabrication of nanostructures is desired, a self-limiting route may be preferred and may be achieved through pulsed supersonic jet lateral atomic deposition. Similar safety considerations must be followed for diborane as the pyrophoric metalorganic precursors.

Precursor Sources: Nitrogen

Nitrogen is often provided via thermal decomposition of ammonia (NH_3) or by activating atomic nitrogen. Ammonia is a convenient nitrogen source with reasonable cracking temperature.[194] No additional equipment is necessary, reducing apparatus cost and maintenance concerns. However, ammonia contains hydrogen which, even at the moderate decomposition temperature, presents the opportunity for graphene etching and, certainly, hydrogen intercalation. Intercalation transforms buffer layer into quasi-freestanding graphene, effectively modifying graphene nanoribbon structures. Reversal will be challenging under a BN capping layer. For these reasons, a pure nitrogen source is desired.

Activated nitrogen is often produced via ionization, electron-cyclotron-resonance (ECR) discharges, and RF plasmas. It is well known that ionic species are damaging to graphene and must be effectively screened if atomic nitrogen sources are to be used.

ECR sources are most common in the literature and are readily available. A solenoid couples the nitrogen gas to 2.45 GHz microwaves to produce a source of atomic, ionic, and molecular nitrogen. The dissociation efficiency can approach 10%.[195, 196] Growth from ECR-generated activated nitrogen must be maintained at low growth rates to limit ion induced damage.

RF (13.56 MHz) plasma activated nitrogen sources are common in commercial CVD and ALD systems. However, when used for graphene devices, ions must be effectively screened.

An RF discharge supersonic jet nozzle was demonstrated to produce atomic nitrogen jets.[197, 198] Dissociation efficiencies were up to 60% in 1% N_2 seeded He beams. The higher dissociation rates, compared to ECR, are related to the higher pressure than in effusion sources. Substrate biasing can be used to reduce damage from ion bombardment. It has been suggested that an Ar beam would have several benefits, namely, a lower first ionization potential and improved momentum transfer to the activated nitrogen to increase its kinetic energy. It has been shown that kinetic energies in excess of 10 eV can cause

surface damage providing an upper bound for the processing space.[199, 200]

Gas Delivery System

The response rate of mas flow controllers (MFC) is insufficient for high speed dosing. As such, a dual seeded jet design is recommended. Such a design has several advantages:

1. Readily tunable kinetic energy
2. The pressure at the substrate surface will always be higher than the ambient disallowing ambient contamination or desorbed species from the walls from reaching the film
3. Pulses can be lined up in the flow for ultra-fast cycle times without the need to purge
4. Addition of precursors for heterostructure production is simple

High speed pulses will be required for precursor injection. In this space, direct injection automotive valves offer competitive specifications at a significantly lower price point than scientific pulse valves, as outlined in Table 4.2. Parker Series 99 valves are industry standard for high speed injection into UHV chambers at moderate temperatures. Recently, automotive fuel injection is moving to direct injection into the cylinder. These valves are designed to function at high temperatures with all metal and ceramic construction, and, naturally, are suited to corrosive chemicals and tight timing tolerances. Gasoline combustion cylinder walls can reach temperatures of 200-300 °C.[201] The Bosch gasoline direct injection solenoid valve, shown in Figure 4.32, is one such product which compares favorably to Parker solenoids at a fraction of the cost. Further, the metal seals will provide much higher reliability and reduced downtime compared to the polymeric seals which must be regularly replaced.

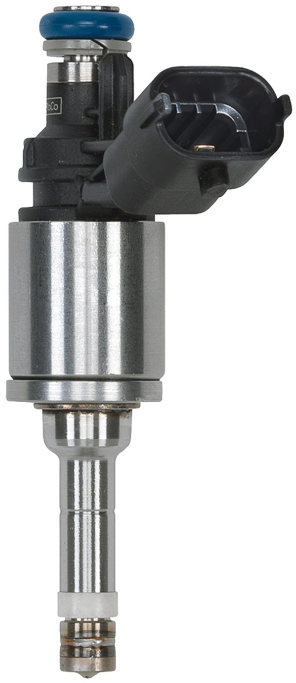

Figure 4.32: Bosch Gasoline Direct Injection valves are well suited to reliable high frequency injection of corrosive vapors. Image from Bosch.

Substrate Handling

Substrates will be inductively heated. A BN-coated graphite susceptor mounted to a rotary stage will improve reliability and uniformity. The surface of the sample will be the closest surface to the jet nozzle to ensure no reacted precursor molecules reach the surface.

The susceptor will raise into a BN or Al_2O_3 reaction chamber. The high thermal conductivity of these materials will enable radiative heat to be transported to the chilled metal chamber walls to minimize precursor decomposition on the walls. A viewport will enable pyrometer temperature measurement.

4.4 Future Materials

In order to become industrially relevant, the LAD material library must be expanded to include other 2D materials. An obvious first candidate is graphene. Vertical heterostructures of graphene-BN-graphene will enable various transistor geometries. Graphene and

Table 4.2: Specifications for Bosch HDEV 5.2 Gasoline Direct Injection Pulse Valve compared to Parker Series 99

Parameter	Parker Series 99	Bosch HDEV4
Injection time		70-5000 µs
Seal Material	Polymeric	Metal
Actuator	Solenoid	Piezo
Orifice Size	0.1-0.79 mm	
Pressure Rating	8.5 MPa	20 MPa
Operating Temperature	4-105 °C	-196-300 °C
Leak Rate	10^{-8} cc/s/atm He	4×10^{-5} cc/s/atm He
Cost	$700 ea	$100 ea

hBN fill the roles of conductor and insulator in the 2D material library. Transition metal dichalcogenides (TMDs), such as MoS_2 and WSe_2, are 2D semiconductors and provide the final pieces to create electronic devices. Most TMDs have a direct band gap of about 2 eV.

The thermal stability of these materials is significantly reduced compared to graphene and hBN which has made direct deposition of arbitrary stacks containing TMDs difficult. LAD technology offers a unique opportunity, through tuning the kinetic energy, to reduce the necessary substrate temperature to enable arbitrary stacking.

Sulfur and selenium are available as simple hydride gases, H_2S and H_2Se, respectively. Metalorganic precursors, such as $Mo(NMe_2)_4$[202, 203, 161] and $W(Co)_6$[202, 118] have been used in to grow MoS_2 and WSe_2, respectively.

CHAPTER 5
CONCLUSION

It has become clear that further advances in epitaxial graphene device performance and fundamental transport studies require integrating high quality dielectric materials into the epitaxial graphene system as a gate, tunneling barrier, and enviornmental protection layer. Despite decades of research, metal oxide growth on graphene surfaces always results in island formation leading to pinholes, electromigration pathways, and non-uniform electric fields. A promising avenue is epitaxial 2D dielectric materials, such as hBN, due to the inherit similarity in bonding character and lattice to graphene which will eliminate many of the problems with amorphous metal oxides.

Boron nitride offers the ideal platform for 2D heterostructure growth and has been shown to offer improved transport over metal oxide dielectric layers in graphene devices. However, transfered dielectric layers induce charge puddles due to trapped impurities and damage from the mechanical transfer process. Therefore, direct growth of 2D heterostructures has gained much attention in recent years; however, large scale, uniform van der Waals solids on epitaxial graphene has not been demonstrated.

This research is a pioneering study of a novel lateral atomic deposition technique, the 2D analog to ALD. As a proof-of-concept, multilayer oriented hBN, preferentially grown directly on epitaxial graphene surfaces was demonstrated. No observed difference was found between the morphology of BN grown on C-face or Si-face epitaxial graphene making it a suitable dielectric material for all epitaxial graphene studies. The growth was not influenced by the number of graphene layers; however, hBN grown directly on SiC and buffer layer exhibited higher densities of surface granules. AFM and SEM analysis of the surface morphology revealed a wrinkled structure similar to multilayer C-face graphene, a characteristic of van der Waals solids grown on traditional substrates at elevated tempera-

tures. The hBN layers on graphene exhibit a high degree of orientation along the c-axis as indicated by HRXRD and HRTEM and are of uniform chemical composition, as shown by XPS.

5.1 Future Work

5.1.1 2D Heterostructure Nanoelectronic Devices

Boron nitride epilayers will serve two functionalities for graphene nanoelectronics: graphene passivation and dielectric device layers. However, these functions lead to fabrication complications when it comes to contacting the underlying graphene. Ideal graphene passivation conditions involve coating the graphene in situ to avoid atmospheric moisture, oxygen, and hydrocarbon contamination. On the other hand, device fabrication necessitates contacting high quality graphene structures. There is no selective chemical etchant for BN, so plasma etching or mechanical lithography will be necessary to expose the graphene. Alternatively, it may be possible to deposit and pattern refractory metal contacts, such as tungsten, or amorphous carbon contacts prior to hBN growth. The observed hBN growth characteristics demonstrated a high degree of selectivity for 2D hBN on graphene surfaces adjacent to SiC and buffer layer regions. Care will be needed to ensure continued graphene quality throughout processing.

A dry etching process for patterning BN will be required to access the underlying graphene. The active species in BN etching are Ar, SF_6, and BCl_3, all large molecules that significantly contribute to physical bombardment, and therefore will not enable suitable selectivity between graphene and BN. This work will implement the recent demonstrations of improved charge carrier injection with one-dimensional contacts[204], which will also alleviate the etch selectivity problem. Dry etching via FIB or RIE will be used to access the edge of the graphene layer. Metal or amorphous carbon will then be deposited into the pits and annealed to establish a conductive pathway to the graphene, as shown in Figure 5.1.

Boron nitride lift-off would enable more traditional 2D graphene contact, but requires

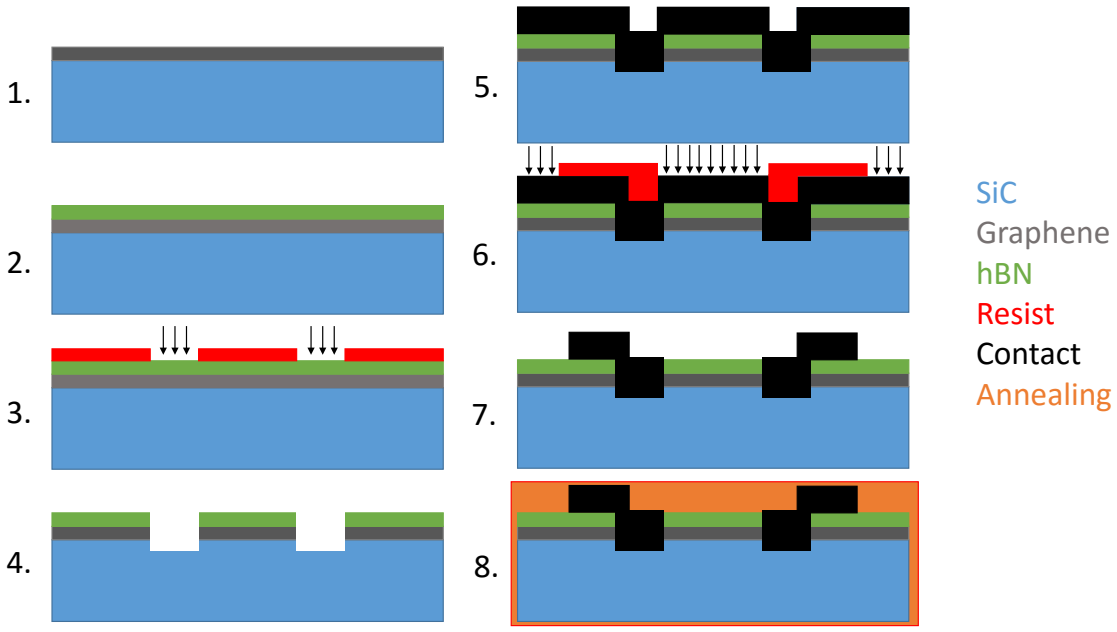

Figure 5.1: The 1D contact fabrication process. 1) Grow graphene structures. 2) Coat with hBN. 3-4) Pattern contact pits with RIE. 5) Deposit contact material. 6-7) Pattern contacts. 8) Anneal to form 1D contact to graphene.

extra processing to deposit a patterned mask on top of the graphene. As one of the motivating reasons for this research was the inability to deposit high quality oxides on graphene, and since photoresist residue is known to be particularly troublesome to completely remove, hydrogen silsesquioxane (HSQ) offers a possible solution. HSQ can be spin coated and cured into a SiO_2 glass layer. It can then be patterned with resist and cleanly etched with HF. Metal or amorphous carbon can then be deposited and patterned to contact the graphene surface.

The ultimate goal is to realize integrated graphene tunneling FETs (TFET) with ballistic leads. A split-gate geometry, as described in Figure 5.2, could be explored utilizing hBN as the gate and nanoselective area GaN growth to fill the gaps [18]. By tuning the density of states in the graphene leads, tunneling through the GaN could be modulated.

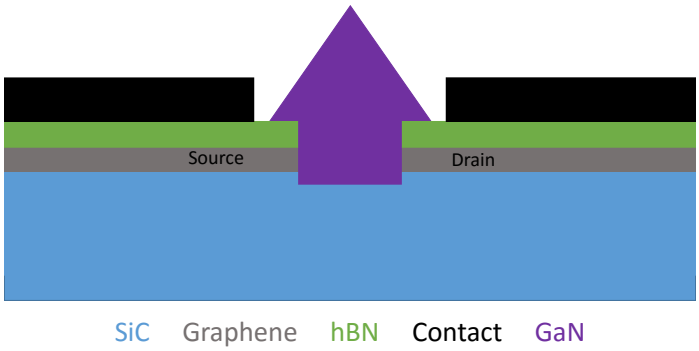

Figure 5.2: Schematic of a split-gate graphene nanoribbon FET.

Appendices

APPENDIX A

EXPERIMENTAL EQUIPMENT: LPCVD SYSTEM

A high vacuum, low pressure chemical vapor deposition (LPCVD) system was built to explore ammonia borane BN production. Earlier work in the de Heer lab had utilized an atmospheric pressure dual zone furnace, but results showed granular films without any crystalline order. Oxygen content was also high and processing times were long due to the slow temperature ramping. It is suspected that the thermal mass of the system contributed to parasitic reactions which polymerized BN chains in the vapor. A new system was designed, as shown in Figure A.1, to remedy these challenges and provide access to new processing space.

Film purity is critically important for electronic performance and epitaxial growth. Ammonia borane only contains boron and nitrogen. The terminating hydrogen atoms are unlikely to incorporate into the film and hydrogen intercalation can be reversed by subsequent vacuum annealing. As such, the purity of the films will be dominated by the atmosphere. Ultra high purity gas sources were used, but to further ensure low oxygen levels, the system was pumped down to $< 10^{-7}$ Torr by a turbo pump prior to deposition.

The reactor vessel itself was fabricated out of quartz glassware in a linear, two zone design, as shown in Figure A.2. The high temperature chamber contained a graphite susceptor, which was heated via external induction coils. This ensures that only carbon, silicon, and ammonia borane products are present within the high temperature zone. The induction heater enables temperatures up to 2000 °C before the quartz loses mechanical strength. Since ammonia borane is an excellent hydrogen source and since hydrogen readily attacks graphite, a quartz liner could be implemented to isolate the substrate from the susceptor. However, this geometry limits the temperature to about 1400 °C. It is important to note that as boron diffuses into the quartz surface, borosilicate glass is formed which has a sig-

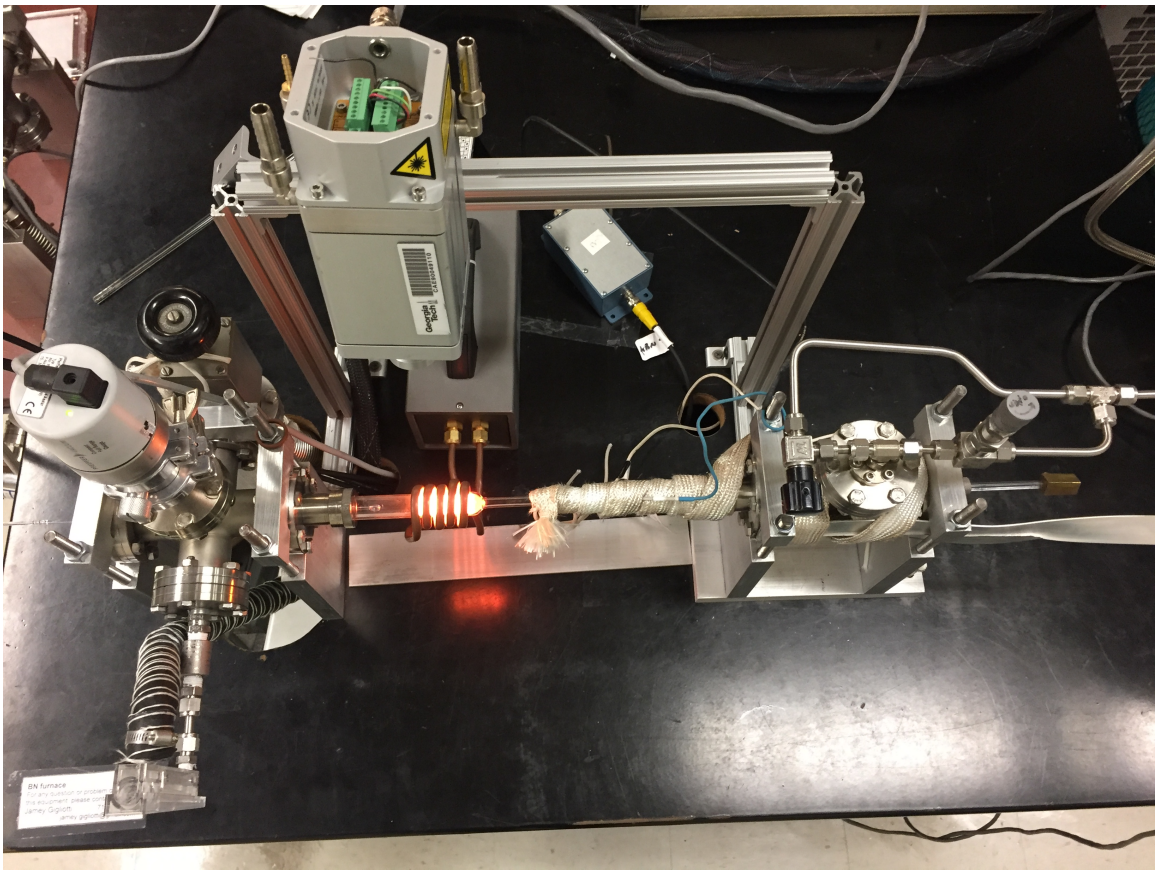

Figure A.1: The LPCVD system provides access to deposition pressures from 10^{-4} Torr up to atmospheric pressure in a ultra high purity environment. The dual chamber design connected by a diffusion tube limits particles in the film.

nificantly lower softening point (820 °C vs 1670 °C for fused quartz). If higher annealing temperature were desired, a separate annealing tube was used without the quartz liner, but would require breaking vacuum. As most metals have significant vapor pressures at these temperatures, an external pyrometer was used to control the temperature while ensuring purity.

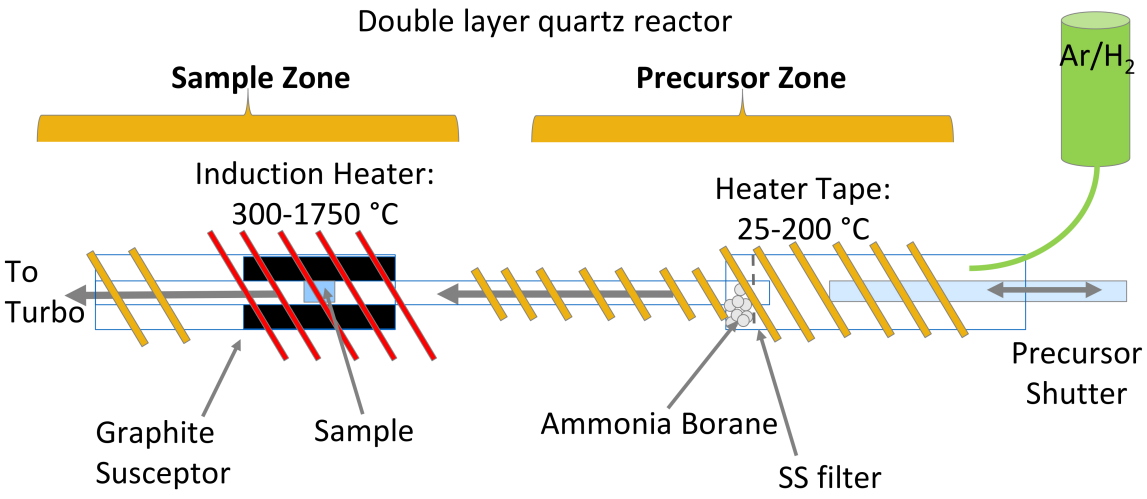

Figure A.2: Custom tube LPCVD reactor layout

The high temperature chamber was connected to an upstream chamber containing the ammonia borane precursor through a narrow, heated tube. As the ammonia borane precursor decomposed, the vapor pressure built up and was carried towards the substrate by a carrier gas of 5% H_2 balanced with Ar. The precursor chamber and connecting tube were heated with heater tape to 70-150 °C. The tube was heated to minimize deposition, and thereby desorption, from the walls. A stainless steel filter was in place to prevent ammonia borane grains from being carried toward the substrate.

APPENDIX B

EXPERIMENTAL EQUIPMENT: HIGH TEMPERATURE PULSED PRECURSOR SYSTEM

Commercially available ALD tools are limited in temperature to about 1000 °C, so a custom reactor was designed and built to provide fast precursor pulsing and substrate temperatures up to 1700 °C. The completed system is shown in Figure B.2. A quartz walled reaction chamber held a graphite susceptor which supported the substrate. As in the LPCVD system, a turbo pump enabled a base pressure of 10^{-7} Torr to combat oxygen contamination and a pyrometer controlled induction heater controlled the temperature.

In contrast to the LPCVD system, the boron and nitrogen sources were separated as triethylborane (Strem Chemicals, 98%) and electronic grade ammonia (Linde, 99.9995%) to eliminate vapor phase parasitic reactions. The ammonia was purified by a GateKeeper Hydride gas purifier which reduced O_2, CO_2, an H_2O levels to < 12 ppb. Gas lines were welded or fitted with VCR connections to ensure high purity to the reaction chamber. The gas lines and valves were heated to 120 °C to prevent precursor deposition and parastic reactions. The helium carrier gas was also purified to < 100 ppt O_2 and H_2O. A UHP H_2 source was also available.

The precursors were dosed into a carrier gas of He or H_2 by high speed ALD pulse valves (Swagelok), as shown in Figure B.3. The carrier was controlled via a mass flow controller (MFC) with downstream shutoff valve to enable high vacuum annealing and growth processes. Exhaust vapors were run through a molecular sieve to remove unreacted precursors.

Processing pressure was monitored via two pressure gauges: a Pirani gauge (Edwards APGX-H) to monitor the pressure during the deposition process and a cold cathode (Pfeiffer PKR 251) to determine base pressure and system cleanliness. The Pirani element was

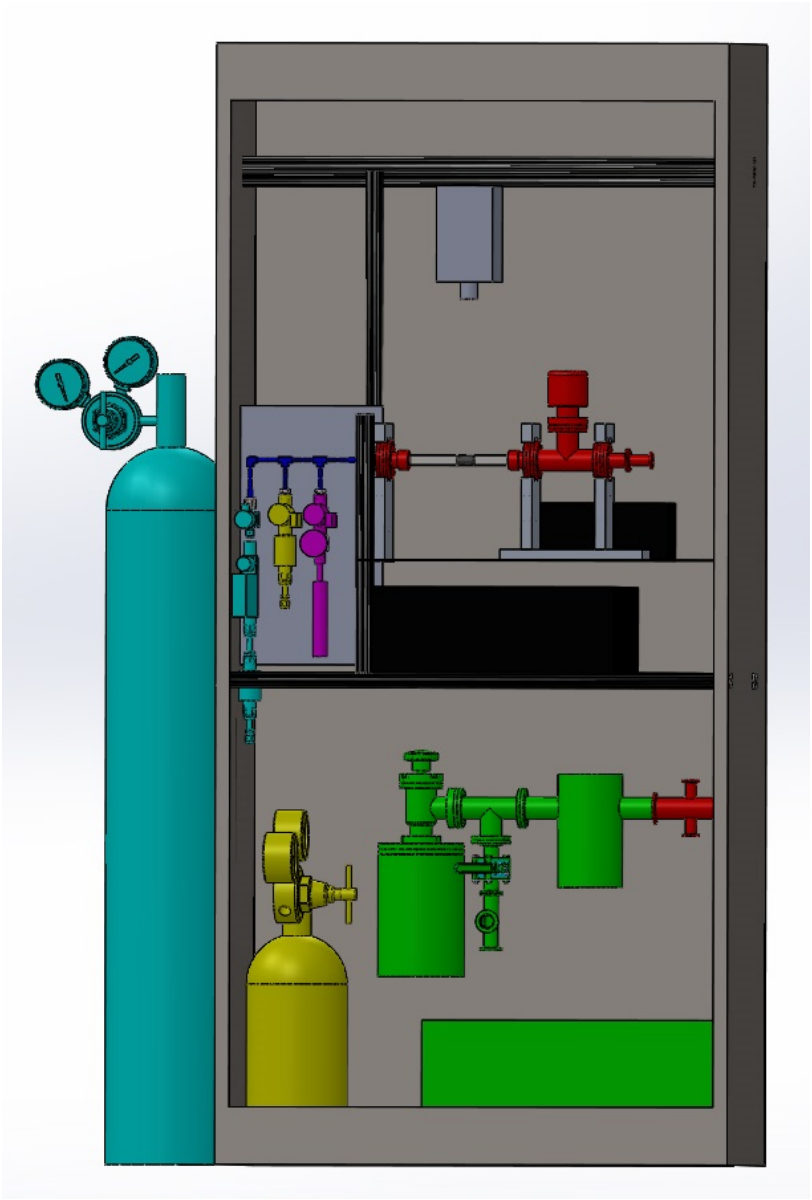

Figure B.1: A custom, high temperature ALD tool was designed to improve BN film nucleation reduce granular cluster formation. Elements in cyan are related to the He carrier gas, yellow are the NH_3 source, magenta are the TEB source, red are the processing chamber components, and green are the pumping components.

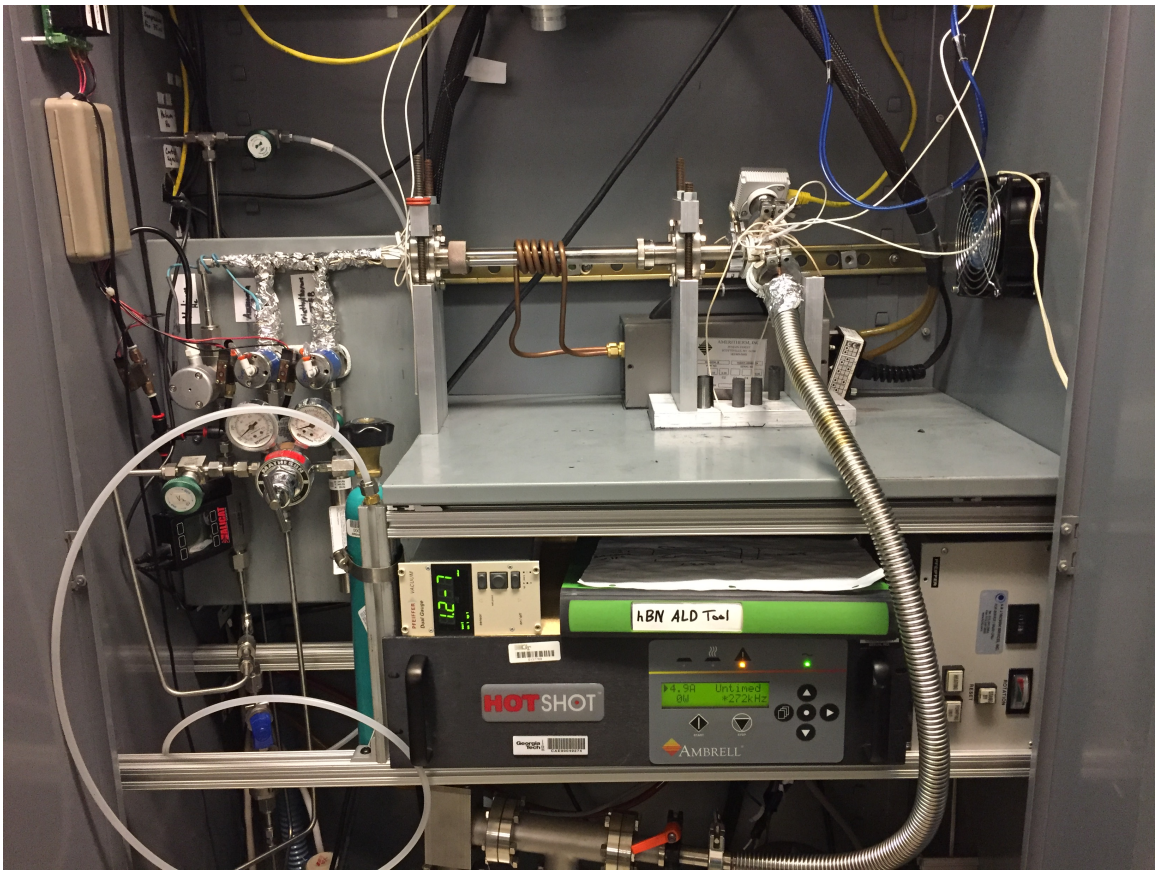

Figure B.2: The HT-ALD system provides access to substrate temperatures in excess of 1700 °C, temperature ramp rates of up to 100 °C/s, a base pressure of 10^{-7} Torr, and precursor pulse widths down to 10 ms.

Figure B.3: The precursors are dosed into a carrier flow of He or H_2 via ALD valves. The heated lines are welded or fitted with VCR fittings to ensure high purity.

heated to 100 °C which minimizes deposition and improves reliability. The cold cathode gauge was valved off during deposition.

The induction susceptor and sample holder was machined out of high purity (< 50 ppm ash) graphite (Graphtek LLC). A schematic is shown in Figure B.4. The design channeled flow over the hot sample surface and held the sample stationary during pulses with a reduced exit diameter. The recessed outer face lengthen quartz lifetime by minimizing contact points which tend to darken the quartz, and thus disrupt reliable readings by the two-color pyrometer. During experiments using H_2 as a carrier, the graphite was significantly damaged and had to be replaced every 2-3 runs. A welded molybdenum susceptor would be an improvement and would reduce turbulence due to the reduced cross section.

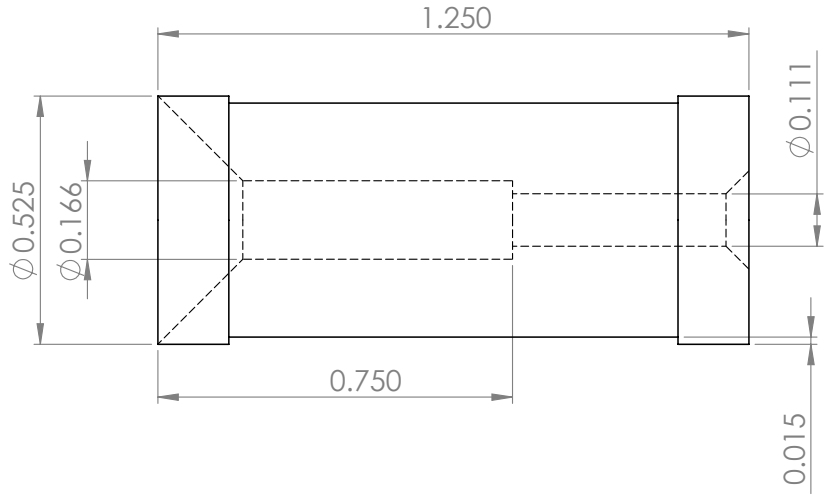

Figure B.4: Schematic of graphite susceptor for the high temperature LAD furnace. Dimensions are in inches. Flow is from left to right wit the substrate sitting in the larger diameter hole.

REFERENCES

[1] C. Berger, Z. M. Song, T. B. Li, X. B. Li, A. Y. Ogbazghi, R. Feng, Z. T. Dai, A. N. Marchenkov, E. H. Conrad, P. N. First, and W. A. de Heer, "Ultrathin epitaxial graphite: 2d electron gas properties and a route toward graphene-based nanoelectronics," *Journal of Physical Chemistry B*, vol. 108, no. 52, pp. 19 912–19 916, 2004.

[2] M. Orlita and M. Potemski, "Dirac electronic states in graphene systems: Optical spectroscopy studies," *Semiconductor Science and Technology*, vol. 25, no. 6, p. 063 001, 2010.

[3] P. R. Wallace, "The band theory of graphite," *Physical Review*, vol. 71, no. 9, pp. 622–634, 1947.

[4] K. S. Novoselov, A. K. Geim, S. V. Morozov, D. Jiang, Y. Zhang, S. V. Dubonos, I. V. Grigorieva, and A. A. Firsov, "Electric field effect in atomically thin carbon films," *Science*, vol. 306, no. 5696, pp. 666–669, 2004.

[5] Y. A. T. N. R. Gall E. V. Rutkov, "Two dimensional graphite films on metals and their intercalation," *International Journal of Modern Physics B*, vol. 11, no. 16, pp. 1865–1911, 1997.

[6] X. Li, W. Cai, J. An, S. Kim, J. Nah, D. Yang, R. Piner, A. Velamakanni, I. Jung, E. Tutuc, S. K. Banerjee, L. Colombo, and R. S. Ruoff, "Large-area synthesis of high-quality and uniform graphene films on copper foils," *Science*, vol. 324, no. 5932, pp. 1312–1314, 2009.

[7] H. P. Boehm, A. Clauss, G. Fischer, and U. Hofmann, "Surface properties of extremely thin graphite lamellae," in *Proceedings of the Fifth Conference on Carbon*. Pergamon, 1962, pp. 73–80, ISBN: 978-0-08-009707-7.

[8] M. S. Bresnehan, M. J. Hollander, M. Wetherington, M. LaBella, K. A. Trumbull, R. Cavalero, D. W. Snyder, and J. A. Robinson, "Integration of hexagonal boron nitride with quasi-freestanding epitaxial graphene: Toward wafer-scale, high-performance devices," *Acs Nano*, vol. 6, no. 6, pp. 5234–5241, 2012.

[9] Q. A. Khan, A. Shaur, T. A. Khan, Y. F. Joya, and M. S. Awan, "Characterization of reduced graphene oxide produced through a modified hoffman method," *Cogent Chemistry*, vol. 3, no. 1, p. 1 298 980, 2017.

[10] A. J. Van Bommel, J. E. Crombeen, and A. Van Tooren, "Leed and auger electron observations of the sic(0001) surface," *Surface Science*, vol. 48, no. 2, pp. 463–472, 1975.

[11] I. Forbeaux, J.-M. Themlin, and J. M. Debever, *Heteroepitaxial graphite on 6H-SiC(0001): Interface formation through conduction-band electronic structure*. 1998, vol. 58, pp. 1 456 495–16 406.

[12] C.-M. Lin, Y.-Y. Chen, and A. P. Pisano, "Theoretical investigation of lamb wave characteristics in aln/3c-sic composite membranes," *APPLIED PHYSICS LETTERS*, vol. 97, no. 19, 2010.

[13] T. Yager, A. Lartsev, R. Yakimova, S. Lara-Avila, and S. Kubatkin, "Wafer-scale homogeneity of transport properties in epitaxial graphene on sic," *Carbon*, vol. 87, pp. 409–414, 2015.

[14] M. Sprinkle, M. Ruan, Y. Hu, J. Hankinson, M. Rubio-Roy, B. Zhang, X. Wu, C. Berger, and W. A. de Heer, "Scalable templated growth of graphene nanoribbons on sic," *Nature Nanotechnology*, vol. 5, no. 10, pp. 727–731, 2010.

[15] J. Baringhaus, M. Ruan, F. Edler, A. Tejeda, M. Sicot, A. Taleb-Ibrahimi, A. P. Li, Z. G. Jiang, E. H. Conrad, C. Berger, C. Tegenkamp, and W. A. de Heer, "Exceptional ballistic transport in epitaxial graphene nanoribbons," *Nature*, vol. 506, no. 7488, pp. 349–354, 2014.

[16] Z. L. Guo, R. Dong, P. S. Chakraborty, N. Lourenco, J. Palmer, Y. K. Hu, M. Ruan, J. Hankinson, J. Kunc, J. D. Cressler, C. Berger, and W. A. de Heer, "Record maximum oscillation frequency in c-face epitaxial graphene transistors," *Nano Letters*, vol. 13, no. 3, pp. 942–947, 2013.

[17] B. Dlubak, M. B. Martin, C. Deranlot, B. Servet, S. Xavier, R. Mattana, M. Sprinkle, C. Berger, W. A. De Heer, F. Petroff, A. Anane, P. Seneor, and A. Fert, "Highly efficient spin transport in epitaxial graphene on sic," *Nature Physics*, vol. 8, no. 7, pp. 557–561, 2012.

[18] R. Puybaret, G. Patriarche, M. B. Jordan, S. Sundaram, Y. E. Gmili, J.-P. Salvestrini, P. L. Voss, W. A. de Heer, C. Berger, and A. Ougazzaden, "Nanoselective area growth of gan by metalorganic vapor phase epitaxy on 4h-sic using epitaxial graphene as a mask," *Applied Physics Letters*, vol. 108, no. 10, p. 103 105, 2016.

[19] G. Gui, J. Li, and J. Zhong, "Band structure engineering of graphene by strain: First-principles calculations," *Physical Review B*, vol. 78, no. 7, p. 075 435, 2008.

[20] R. Balog, B. Jorgensen, L. Nilsson, M. Andersen, E. Rienks, M. Bianchi, M. Fanetti, E. Laegsgaard, A. Baraldi, S. Lizzit, Z. Sljivancanin, F. Besenbacher, B. Hammer,

T. G. Pedersen, P. Hofmann, and L. Hornekaer, "Bandgap opening in graphene induced by patterned hydrogen adsorption," *Nat Mater*, vol. 9, no. 4, pp. 315–319, 2010.

[21] S. Y. Lee, D. L. Duong, Q. A. Vu, Y. Jin, P. Kim, and Y. H. Lee, "Chemically modulated band gap in bilayer graphene memory transistors with high on/off ratio," *ACS Nano*, vol. 9, no. 9, pp. 9034–9042, 2015.

[22] D. Svintsov, V. Vyurkov, A. Orlikovsky, V. Ryzhii, and T. Otsuji, "All-graphene field-effect transistor based on lateral tunnelling," *Journal of Physics D-Applied Physics*, vol. 47, no. 9, p. 094 002, 2014.

[23] R. Dong, Z. L. Guo, J. Palmer, Y. K. Hu, M. Ruan, J. Hankinson, J. Kunc, S. K. Bhattacharya, C. Berger, and W. A. de Heer, "Wafer bonding solution to epitaxial graphene-silicon integration," *Journal of Physics D-Applied Physics*, vol. 47, no. 9, p. 8, 2014.

[24] J. Yan and M. S. Fuhrer, "Correlated charged impurity scattering in graphene," *Phys Rev Lett*, vol. 107, no. 20, p. 206 601, 2011.

[25] D. Marchenko, A. Varykhalov, A. Rybkin, A. M. Shikin, and O. Rader, "Atmospheric stability and doping protection of noble-metal intercalated graphene on ni(111)," *Applied Physics Letters*, vol. 98, no. 12, p. 122 111, 2011.

[26] X. Wu, Y. Hu, M. Ruan, N. K. Madiomanana, J. Hankinson, M. Sprinkle, C. Berger, and W. A. de Heer, "Half integer quantum hall effect in high mobility single layer epitaxial graphene," *Applied Physics Letters*, vol. 95, no. 22, p. 223 108, 2009.

[27] Y. Yang, L.-I. Huang, Y. Fukuyama, F.-H. Liu, M. A. Real, P. Barbara, C.-T. Liang, D. B. Newell, and R. E. Elmquist, "Low carrier density epitaxial graphene devices on sic," *Small*, vol. 11, no. 1, pp. 90–95, 2015.

[28] D. Deniz, "Ballistic transport in epitaxial graphene nanoribbons," Proposal, 2016.

[29] H. Brune, "Epitaxial growth of thin films," in *Surface and Interface Science: Solid-State Interfaces and Thin Films*, K. Wandelt, Ed. Wiley-VCH, 2014, ch. 20.

[30] I. Markov, *Crystal Growth for Beginners: Fundamentals of Nucleation, Crystal Growth and Epitaxy*. WORLD SCIENTIFIC Publishing Company Incorporated, 2016, ISBN: 9789813143425.

[31] A. Zangwill, *Physics at surfaces*. Cambridge [Cambridgeshire] ; New York: Cambridge Cambridgeshire ; New York : Cambridge University Press, 1988.

[32] W. K. Burton, N. Cabrera, and F. C. Frank, "The growth of crystals and the equilibrium structure of their surfaces," *Philosophical Transactions of the Royal Society of London Series a-Mathematical and Physical Sciences*, vol. 243, no. 866, pp. 299–358, 1951.

[33] W. Kossel, "Extending the law of bravais," *Nachr. Ges. Wiss*, p. 143, 1927.

[34] I. Stranski, "Zur theorie des kristallwachstums," *Z. Phys. Chem*, vol. 136, pp. 259–278, 1928.

[35] J. H. van der Merwe, in *CRC Critical Reviews in Solid State and Materials Science*, R. Vancelow, Ed. Boca Raton, CRC Press, 1979, p. 209.

[36] N. L. Yoder, N. P. Guisinger, M. C. Hersam, R. Jorn, C. C. Kaun, and T. Seideman, "Quantifying desorption of saturated hydrocarbons from silicon with quantum calculations and scanning tunneling microscopy," *Physical Review Letters*, vol. 97, no. 18, p. 187 601, 2006.

[37] R. Zacharia, H. Ulbricht, and T. Hertel, "Interlayer cohesive energy of graphite from thermal desorption of polyaromatic hydrocarbons," *Physical Review B*, vol. 69, no. 15, p. 155 406, 2004.

[38] D. Wang, G. Chen, C. Li, M. Cheng, W. Yang, S. Wu, G. Xie, J. Zhang, J. Zhao, X. Lu, P. Chen, G. Wang, J. Meng, J. Tang, R. Yang, C. He, D. Liu, D. Shi, K. Watanabe, T. Taniguchi, J. Feng, Y. Zhang, and G. Zhang, "Thermally induced graphene rotation on hexagonal boron nitride," *Phys Rev Lett*, vol. 116, no. 12, p. 126 101, 2016.

[39] L. Royer, *Recherches exprimentales sur l'pitaxie ou orientation mutuelle des cristaux d'espces diffrentes*. St. Gnr. d'Imprimerie et d'Edition, 1928.

[40] D. Martoccia, P. R. Willmott, T. Brugger, M. Bjrck, S. Gnther, C. M. Schleptz, A. Cervellino, S. A. Pauli, B. D. Patterson, S. Marchini, J. Wintterlin, W. Moritz, and T. Greber, "Graphene on ru(0001): A 25x25 supercell," *Physical Review Letters*, vol. 101, no. 12, p. 126 102, 2008.

[41] F. Owman and P. Mrtensson, "The sic(0001)6v3 6v3 reconstruction studied with stm and leed," *Surface Science*, vol. 369, no. 1, pp. 126–136, 1996.

[42] H Mayer, "Advances in epitaxy and endotaxy," in, R. N. Mayer and H., Eds. Leipzig: EB Deutscher Verlag fur Grundstoffsindustrie, 1971.

[43] J. Hass, F. Varchon, J. E. Millan-Otoya, M. Sprinkle, N. Sharma, W. A. De Heer, C. Berger, P. N. First, L. Magaud, and E. H. Conrad, "Why multilayer graphene on

4h-sic(000(1)over-bar) behaves like a single sheet of graphene," *Physical Review Letters*, vol. 100, no. 12, p. 4, 2008.

[44] J. R. Arthur, "Molecular beam epitaxy," *Surface Science*, vol. 500, no. 1, pp. 189–217, 2002.

[45] J. Hornstra, "Dislocations in the diamond lattice," *Journal of Physics and Chemistry of Solids*, vol. 5, no. 1-2, pp. 129–141, 1958.

[46] D. B. Holt, "Misfit dislocations in semiconductors," *Journal of Physics and Chemistry of Solids*, vol. 27, no. 6-7, pp. 1053–+, 1966.

[47] B. L. Sharma and R. K. Purohit, *Semiconductor Heterojunctions*. Pergamon Press, 1974.

[48] W. Bollmann, "On the geometry of grain and phase boundaries," *Philosophical Magazine*, vol. 16, no. 140, pp. 383–399, 1967.

[49] A. Thomy, X. Duval, and J. Regnier, "Two-dimensional phase transitions as displayed by adsorption isotherms on graphite and other lamellar solids," *Surface Science Reports*, vol. 1, no. 1, pp. 1–38, 1981.

[50] G. Gilmer, "Computer models of crystal growth," *Science*, vol. 208, no. 4442, pp. 355–363, 1980.

[51] I. Markov and S. Stoyanov, "Mechanisms of epitaxial growth," *Contemporary Physics*, vol. 28, no. 3, pp. 267–320, 1987.

[52] I. Levine, A. Yoffe, A. Salomon, W. J. Li, Y. Feldman, and A. Vilan, "Epitaxial two dimensional aluminum films on silicon (111) by ultra-fast thermal deposition," *Journal of Applied Physics*, vol. 111, no. 12, p. 9, 2012.

[53] M. Bumer, J. Libuda, and H. J. Freund, "The temperature dependent growth mode of nickel on the basal plane of graphite," *Surface Science*, vol. 327, no. 3, pp. 321–329, 1995.

[54] W. C. Fan, J. Strozier, and A. Ignatiev, "Island formation of aluminum on the graphite (0001) surface: Leed and aes study," *Surface Science*, vol. 195, no. 12, pp. 226–236, 1988.

[55] C. Argile and G. E. Rhead, "Adsorbed layer and thin film growth modes monitored by auger electron spectroscopy," *Surface Science Reports*, vol. 10, no. 6-7, pp. 277–356, 1989.

[56] W. D. Luedtke and U. Landman, "Slip diffusion and lévy flights of an adsorbed gold nanocluster," *Physical Review Letters*, vol. 82, no. 19, pp. 3835–3838, 1999.

[57] M. S. Levine, A. A. Golovin, and V. A. Volpert, "Step-flow growth of a crystal surface by lvy flights," *EPL (Europhysics Letters)*, vol. 82, no. 2, p. 28 007, 2008.

[58] G. Ehrlich, "Atomic displacements in one and twodimensional diffusion," *The Journal of Chemical Physics*, vol. 44, no. 3, pp. 1050–1055, 1966.

[59] R. L. Schwoebel and E. J. Shipsey, "Step motion on crystal surfaces," *Journal of Applied Physics*, vol. 37, no. 10, pp. 3682–3686, 1966.

[60] X. Wende, K. Sunil Singh, and W. Xue-sen, "Nucleation and growth of aluminum on an inert substrate of graphite," *Journal of Physics: Condensed Matter*, vol. 20, no. 22, p. 225 002, 2008.

[61] V. Maurice and P. Marcus, "Stm study of sputter-deposited al clusters in chemical interaction with graphite (0001) surfaces," *Surface Science*, vol. 275, no. 1, pp. 65–74, 1992.

[62] R. Anton and I. Schneidereit, "In situ tem investigations of dendritic growth of au particles on hopg," *Physical Review B*, vol. 58, no. 20, pp. 13 874–13 881, 1998.

[63] C. M. Wayman and T. P. Darby, "Nucleation and growth of gold films on graphite," *Journal of Crystal Growth*, vol. 28, no. 1, pp. 53–67, 1975.

[64] R. Anton and P. Kreutzer, "In situ tem evaluation of the growth kinetics of au particles on highly oriented pyrolithic graphite at elevated temperatures," *Physical Review B*, vol. 61, no. 23, pp. 16 077–16 083, 2000.

[65] T. P. Darby and C. M. Wayman, "Nucleation and growth of gold-films on graphite .1. effects of substrate condition and evaporation rate," *Journal of Crystal Growth*, vol. 28, no. 1, pp. 41–52, 1975.

[66] E. L. Evans, O. P. Bahl, and J. M. Thomas, "The decoration of, and epitaxial growth of gold on, graphite surfaces," *Carbon*, vol. 5, no. 6, pp. 587–589, 1967.

[67] D. A. Steigerwald, I. Jacob, and W. F. Egelhoff, "Structural study of the epitaxial growth of fcc-fe films, sandwiches, and superlattices on cu(100)," *Surface Science*, vol. 202, no. 3, pp. 472–492, 1988.

[68] M. Kalff, G. Comsa, and T. Michely, *How Sensitive is Epitaxial Growth to Adsorbates?* 1998, vol. 81, pp. 1255–1258.

[69] R. F. Thompson, D. T. Clark, A. E. Murphy, E. P. Ramsay, D. A. Smith, R. A. R. Young, J. D. Cormack, J. McGonigal, J. Fletcher, C. Zhu, S. Finney, L. C. Martin, and A. B. Horsfall, "High temperature silicon carbide cmos integrated circuits," *Additional Conferences (Device Packaging, HiTEC, HiTEN, & CICMT)*, vol. 2011, no. HITEN, pp. 000 115–000 119, 2011.

[70] W. Norimatsu and M. Kusunoki, "Epitaxial graphene on sic(0001): Advances and perspectives," *Physical Chemistry Chemical Physics*, vol. 16, no. 8, pp. 3501–3511, 2014.

[71] S. G. Davis, D. F. Anthrop, and A. W. Searcy, "Vapor pressure of silicon and the dissociation pressure of silicon carbide," *The Journal of Chemical Physics*, vol. 34, no. 2, pp. 659–664, 1961.

[72] D. V. Badami, "Graphitization of [alpha]-silicon carbide," *Nature*, vol. 193, no. 4815, pp. 569–570, 1962.

[73] W. A. de Heer, C. Berger, M. Ruan, M. Sprinkle, X. Li, Y. Hu, B. Zhang, J. Hankinson, and E. Conrad, "Large area and structured epitaxial graphene produced by confinement controlled sublimation of silicon carbide," *Proceedings of the National Academy of Sciences*, vol. 108, no. 41, pp. 16 900–16 905, 2011.

[74] M. S. Nevius, M. Conrad, F. Wang, A. Celis, M. N. Nair, A. Taleb-Ibrahimi, A. Tejeda, and E. H. Conrad, "Semiconducting graphene from highly ordered substrate interactions," *Phys Rev Lett*, vol. 115, no. 13, p. 136 802, 2015.

[75] C. Riedl, C. Coletti, T. Iwasaki, A. A. Zakharov, and U. Starke, "Quasi-free-standing epitaxial graphene on sic obtained by hydrogen intercalation," *Physical Review Letters*, vol. 103, no. 24, p. 246 804, 2009.

[76] I. Palacio, A. Celis, M. N. Nair, A. Gloter, A. Zobelli, M. Sicot, D. Malterre, M. S. Nevius, W. A. de Heer, C. Berger, E. H. Conrad, A. Taleb-Ibrahimi, and A. Tejeda, "Atomic structure of epitaxial graphene sidewall nanoribbons: Flat graphene, miniribbons, and the confinement gap," *Nano Letters*, vol. 15, no. 1, pp. 182–189, 2015.

[77] J. Hass, W. A. de Heer, and E. H. Conrad, "The growth and morphology of epitaxial multilayer graphene," *Journal of Physics-Condensed Matter*, vol. 20, no. 32, p. 27, 2008.

[78] V. Borovikov and A. Zangwill, "Step bunching of vicinal 6h-sic(0001) surfaces," *Physical Review B*, vol. 79, no. 24, p. 9, 2009.

[79] C. elebi, C. Yank, A. G. Demirkol, and s. Kaya, "Control of the graphene growth rate on capped sic surface under strong si confinement," *Applied Surface Science*, vol. 264, no. 0, pp. 56–60, 2013.

[80] Y. V. Naidich and G. A. Kolesnichenko, "Study of the wetting of diamond and graphite by liquid metals," *Soviet Powder Metallurgy and Metal Ceramics*, vol. 2, no. 1, pp. 35–38, 1964.

[81] C. C. Landry and A. R. Barron, "Mocvd of alumina-silica oxidation-resistant coatings on carbon-fibers," *Carbon*, vol. 33, no. 4, pp. 381–387, 1995.

[82] Q. Ma and R. A. Rosenberg, "Interaction of ti with the (0001) surface of highly oriented pyrolitic graphite," *Physical Review B - Condensed Matter and Materials Physics*, vol. 60, no. 4, pp. 2827–2832, 1999.

[83] B. Dlubak, P. Seneor, A. Anane, C. Barraud, C. Deranlot, D. Deneuve, B. Servet, R. Mattana, F. Petroff, and A. Fert, "Are al2o3 and mgo tunnel barriers suitable for spin injection in graphene?" *Applied Physics Letters*, vol. 97, no. 9, p. 092 502, 2010.

[84] X. R. Wang, S. M. Tabakman, and H. J. Dai, "Atomic layer deposition of metal oxides on pristine and functionalized graphene," *Journal of the American Chemical Society*, vol. 130, no. 26, pp. 8152–+, 2008.

[85] B. Dlubak, P. R. Kidambi, R. S. Weatherup, S. Hofmann, and J. Robertson, "Substrate-assisted nucleation of ultra-thin dielectric layers on graphene by atomic layer deposition," *Applied Physics Letters*, vol. 100, no. 17, p. 173 113, 2012.

[86] H. Alles, J. Aarik, J. Kozlova, A. Niilisk, R. Rammula, and V. Sammelselg, "Atomic layer deposition of high-k oxides on graphene," in *Graphene - Synthesis, Characterization, Properties and Applications*, J. Gong, Ed. 2011, ch. 7, ISBN: 978-953-307-292-0.

[87] L. D. Wang, J. J. Travis, A. S. Cavanagh, X. H. Liu, S. P. Koenig, P. Y. Huang, S. M. George, and J. S. Bunch, "Ultrathin oxide films by atomic layer deposition on graphene," *Nano Letters*, vol. 12, no. 7, pp. 3706–3710, 2012.

[88] G. Hongwei, L. Yunlong, X. Yang, M. Nan, W. Hongtao, H. Tawfique, W. Xinran, L. Jikui, and Y. Bin, "Fluorinated graphene and hexagonal boron nitride as ald seed layers for graphene-based van der waals heterostructures," *Nanotechnology*, vol. 25, no. 35, p. 355 202, 2014.

[89] F. Miriam, W. Mirosaw, M. Andr, W. Stefan, D. Thorsten, W. Thomas, and J. A. Franz, "Versatile sputtering technology for al 2 o 3 gate insulators on graphene," *Science and Technology of Advanced Materials*, vol. 13, no. 2, p. 025 007, 2012.

[90] Z. Wang and Y. Liu, "Piezoelectric effect at nanoscale," in *Encyclopedia of Nanotechnology*, B. Bhushan, Ed. Springer Netherlands, 2012, ch. 273, pp. 2085–2099, ISBN: 978-90-481-9750-7.

[91] M.-B. Martin, B. Dlubak, R. S. Weatherup, H. Yang, C. Deranlot, K. Bouzehouane, F. Petroff, A. Anane, S. Hofmann, J. Robertson, A. Fert, and P. Seneor, "Sub-nanometer atomic layer deposition for spintronics in magnetic tunnel junctions based on graphene spin-filtering membranes," *ACS Nano*, vol. 8, no. 8, pp. 7890–7895, 2014.

[92] R. Rammula, L. Aarik, A. Kasikov, J. Kozlova, T. Kahro, L. Matisen, A. Niilisk, H. Alles, and J. Aarik, "Atomic layer deposition of aluminum oxide films on graphene," *International Conference on Functional Materials and Nanotechnologies 2013 (Fm&Nt2-13)*, vol. 49, p. 4, 2013.

[93] J. M. P. Alaboson, Q. H. Wang, J. D. Emery, A. L. Lipson, M. J. Bedzyk, J. W. Elam, M. J. Pellin, and M. C. Hersam, "Seeding atomic layer deposition of high-k dielectrics on epitaxial graphene with organic self-assembled monolayers," *ACS Nano*, vol. 5, no. 6, pp. 5223–5232, 2011.

[94] V. K. Sangwan, D. Jariwala, S. A. Filippone, H. J. Karmel, J. E. Johns, J. M. P. Alaboson, T. J. Marks, L. J. Lauhon, and M. C. Hersam, "Quantitatively enhanced reliability and uniformity of high- dielectrics on graphene enabled by self-assembled seeding layers," *Nano Letters*, vol. 13, no. 3, pp. 1162–1167, 2013.

[95] P. Wehrfritz, F. Fromm, S. Malzer, and T. Seyller, "Quasi-freestanding epitaxial graphene transistor with silicon nitride top gate," *Journal of Physics D: Applied Physics*, vol. 47, no. 30, p. 305 103, 2014.

[96] K. K. Kim, A. Hsu, X. T. Jia, S. M. Kim, Y. M. Shi, M. Dresselhaus, T. Palacios, and J. Kong, "Synthesis and characterization of hexagonal boron nitride film as a dielectric layer for graphene devices," *Acs Nano*, vol. 6, no. 10, pp. 8583–8590, 2012.

[97] R. M. Feenstra, D. Jena, and G. Gu, "Single-particle tunneling in doped graphene-insulator-graphene junctions," *Journal of Applied Physics*, vol. 111, no. 4, p. 10, 2012.

[98] P. M. Campbell, J. K. Smith, W. J. Ready, and E. M. Vogel, "Material constraints and scaling of 2-d vertical heterostructure interlayer tunnel field-effect transistors," *Ieee Transactions on Electron Devices*, vol. 64, no. 6, pp. 2714–2720, 2017.

[99] S. P. Ge, K. M. M. Habib, A. De, Y. Barlas, D. Wickramaratne, M. R. Neupane, and R. K. Lake, "Interlayer transport through a graphene/rotated boron nitride/graphene heterostructure," *Physical Review B*, vol. 95, no. 4, p. 045 303, 2017.

[100] M. Wang, S. K. Jang, W. J. Jang, M. Kim, S. Y. Park, S. W. Kim, S. J. Kahng, J. Y. Choi, R. S. Ruoff, Y. J. Song, and S. Lee, "A platform for large-scale graphene

electronics - cvd growth of single-layer graphene on cvd-grown hexagonal boron nitride," *Advanced Materials*, vol. 25, no. 19, pp. 2746–2752, 2013.

[101] L. A. Ponomarenko, R. V. Gorbachev, G. L. Yu, D. C. Elias, R. Jalil, A. A. Patel, A. Mishchenko, A. S. Mayorov, C. R. Woods, J. R. Wallbank, M. Mucha-Kruczynski, B. A. Piot, M. Potemski, I. V. Grigorieva, K. S. Novoselov, F. Guinea, V. I. Fal'ko, and A. K. Geim, "Cloning of dirac fermions in graphene superlattices," *Nature*, vol. 497, no. 7451, pp. 594–597, 2013.

[102] K. Nomura and A. H. MacDonald, "Quantum transport of massless dirac fermions," *Phys Rev Lett*, vol. 98, no. 7, p. 076 602, 2007.

[103] E. H. Hwang, S. Adam, and S. D. Sarma, "Carrier transport in two-dimensional graphene layers," *Phys Rev Lett*, vol. 98, no. 18, p. 186 806, 2007.

[104] H. Chen, M. B. Muller, K. J. Gilmore, G. G. Wallace, and D. Li, "Mechanically strong, electrically conductive, and biocompatible graphene paper," *Advanced Materials*, vol. 20, no. 18, pp. 3557–+, 2008.

[105] S. Das Sarma, S. Adam, E. H. Hwang, and E. Rossi, "Electronic transport in two-dimensional graphene," *Reviews of Modern Physics*, vol. 83, no. 2, pp. 407–470, 2011.

[106] M. Ishigami, J. H. Chen, W. G. Cullen, M. S. Fuhrer, and E. D. Williams, "Atomic structure of graphene on sio2," *Nano Lett*, vol. 7, no. 6, pp. 1643–8, 2007.

[107] M. I. Katsnelson and A. K. Geim, "Electron scattering on microscopic corrugations in graphene," *Philos Trans A Math Phys Eng Sci*, vol. 366, no. 1863, pp. 195–204, 2008.

[108] M. I. Morozov and D. Damjanovic, "Hardening-softening transition in fe-doped pb(zr,ti)o3 ceramics and evolution of the third harmonic of the polarization response," *Journal of Applied Physics*, vol. 104, no. 3, pp. 034 107–1–8, 2008.

[109] T. Ando, "Screening effect and impurity scattering in monolayer graphene," *Journal of the Physical Society of Japan*, vol. 75, no. 7, p. 074 716, 2006.

[110] P. Vogt, P. De Padova, C. Quaresima, J. Avila, E. Frantzeskakis, M. C. Asensio, A. Resta, B. Ealet, and G. Le Lay, "Silicene: Compelling experimental evidence for graphenelike two-dimensional silicon," *Physical Review Letters*, vol. 108, no. 15, p. 155 501, 2012.

[111] M. E. Dvila, L. Xian, S. Cahangirov, A. Rubio, and G. L. Lay, "Germanene: A novel two-dimensional germanium allotrope akin to graphene and silicene," *New Journal of Physics*, vol. 16, no. 9, p. 095 002, 2014.

[112] Z. Y. Al Balushi, K. Wang, R. K. Ghosh, R. A. Vila, S. M. Eichfeld, J. D. Caldwell, X. Qin, Y.-C. Lin, P. A. DeSario, G. Stone, S. Subramanian, D. F. Paul, R. M. Wallace, S. Datta, J. M. Redwing, and J. A. Robinson, "Two-dimensional gallium nitride realized via graphene encapsulation," *Nat Mater*, vol. advance online publication, 2016.

[113] J. A. Miwa, M. Dendzik, S. S. Gronborg, M. Bianchi, J. V. Lauritsen, P. Hofmann, and S. Ulstrup, "Van der waals epitaxy of two-dimensional mos2-graphene heterostructures in ultrahigh vacuum," *Acs Nano*, vol. 9, no. 6, pp. 6502–6510, 2015.

[114] A. A. Koos, P. Vancso, G. Z. Magda, Z. Osvath, K. Kertesz, G. Dobrik, C. Hwang, L. Tapaszto, and L. P. Biro, "Stm study of the mos2 flakes grown on graphite: A model system for atomically clean 2d heterostructure interfaces," *Carbon*, vol. 105, pp. 408–415, 2016.

[115] Q. F. Liu, Y. P. Gong, T. Wang, W. L. Chan, and J. Wu, "Metal-catalyst-free and controllable growth of high-quality monolayer and ab-stacked bilayer graphene on silicon dioxide," *Carbon*, vol. 96, pp. 203–211, 2016.

[116] G. V. Bianco, M. Losurdo, M. M. Giangregorio, A. Sacchetti, P. Prete, N. Lovergine, P. Capezzuto, and G. Bruno, "Direct epitaxial cvd synthesis of tungsten disulfide on epitaxial and cvd graphene," *Rsc Advances*, vol. 5, no. 119, pp. 98 700–98 708, 2015.

[117] J.-K. Huang, J. Pu, C.-L. Hsu, M.-H. Chiu, Z.-Y. Juang, Y.-H. Chang, W.-H. Chang, Y. Iwasa, T. Takenobu, and L.-J. Li, "Large-area synthesis of highly crystalline wse2 monolayers and device applications," *ACS Nano*, vol. 8, no. 1, pp. 923–930, 2014.

[118] S. M. Eichfeld, L. Hossain, Y. C. Lin, A. F. Piasecki, B. Kupp, A. G. Birdwell, R. A. Burke, N. Lu, X. Peng, J. Li, A. Azcatl, S. McDonnell, R. M. Wallace, M. J. Kim, T. S. Mayer, J. M. Redwing, and J. A. Robinson, "Highly scalable, atomically thin wse2 grown via metal-organic chemical vapor deposition," *Acs Nano*, vol. 9, no. 2, pp. 2080–2087, 2015.

[119] Y. C. Lin, C. Y. S. Chang, R. K. Ghosh, J. Li, H. Zhu, R. Addou, B. Diaconescu, T. Ohta, X. Peng, N. Lu, M. J. Kim, J. T. Robinson, R. M. Wallace, T. S. Mayer, S. Datta, L. J. Li, and J. A. Robinson, "Atomically thin heterostructures based on single-layer tungsten diselenide and graphene," *Nano Letters*, vol. 14, no. 12, pp. 6936–6941, 2014.

[120] Y.-C. Lin, N. Lu, N. Perea-Lopez, J. Li, Z. Lin, X. Peng, C. H. Lee, C. Sun, L. Calderin, P. N. Browning, M. S. Bresnehan, M. J. Kim, T. S. Mayer, M. Terrones, and J. A. Robinson, "Direct synthesis of van der waals solids," *ACS Nano*, vol. 8, no. 4, pp. 3715–3723, 2014.

[121] J. Kim, C. Bayram, H. Park, C.-W. Cheng, C. Dimitrakopoulos, J. A. Ott, K. B. Reuter, S. W. Bedell, and D. K. Sadana, "Principle of direct van der waals epitaxy of single-crystalline films on epitaxial graphene," *Nat Commun*, vol. 5, 2014.

[122] T. Pham, A. P. Goldstein, J. P. Lewicki, S. O. Kucheyev, C. Wang, T. P. Russell, M. A. Worsley, L. Woo, W. Mickelson, and A. Zettl, "Nanoscale structure and superhydrophobicity of sp2-bonded boron nitride aerogels," *Nanoscale*, vol. 7, no. 23, pp. 10 449–10 458, 2015.

[123] S. N. Grinyaev and V. V. Lopatin, "Electronic structure of graphite-like and rhombohedral boron nitride," *Russian Physics Journal*, vol. 35, no. 2, pp. 122–126, 1992.

[124] B. Arnaud, S. Lebegue, P. Rabiller, and M. Alouani, "Huge excitonic effects in layered hexagonal boron nitride," *Physical Review Letters*, vol. 96, no. 2, p. 4, 2006.

[125] K. Watanabe, T. Taniguchi, and H. Kanda, "Direct-bandgap properties and evidence for ultraviolet lasing of hexagonal boron nitride single crystal," *Nature Materials*, vol. 3, no. 6, pp. 404–409, 2004.

[126] X. Li, S. Sundaram, Y. El Gmili, T. Ayari, R. Puybaret, G. Patriarche, P. L. Voss, J. P. Salvestrini, and A. Ougazzaden, "Large-area two-dimensional layered hexagonal boron nitride grown on sapphire by metalorganic vapor phase epitaxy," *Crystal Growth & Design*, 2016.

[127] CassaboisG, ValvinP, and GilB, "Hexagonal boron nitride is an indirect bandgap semiconductor," *Nat Photon*, vol. 10, no. 4, pp. 262–266, 2016.

[128] M. Son, H. Lim, M. Hong, and H. C. Choi, "Direct growth of graphene pad on exfoliated hexagonal boron nitride surface," *Nanoscale*, vol. 3, no. 8, pp. 3089–3093, 2011.

[129] C. R. Dean, A. F. Young, I. Meric, C. Lee, L. Wang, S. Sorgenfrei, K. Watanabe, T. Taniguchi, P. Kim, K. L. Shepard, and J. Hone, "Boron nitride substrates for high-quality graphene electronics," *Nat Nanotechnol*, vol. 5, no. 10, pp. 722–6, 2010.

[130] K. H. Lee, H. J. Shin, J. Lee, I. Y. Lee, G. H. Kim, J. Y. Choi, and S. W. Kim, "Large-scale synthesis of high-quality hexagonal boron nitride nanosheets for large-area graphene electronics," *Nano Letters*, vol. 12, no. 2, pp. 714–718, 2012.

[131] M. Corso, W. Auwrter, M. Muntwiler, A. Tamai, T. Greber, and J. Osterwalder, "Boron nitride nanomesh," *Science*, vol. 303, no. 5655, pp. 217–220, 2004.

[132] A. B. Preobrajenski, A. S. Vinogradov, and N. Mrtensson, "Monolayer of h-bn chemisorbed on cu(1 1 1) and ni(1 1 1): The role of the transition metal 3d states," *Surface Science*, vol. 582, no. 13, pp. 21–30, 2005.

[133] C. Bjelkevig, Z. Mi, J. Xiao, P. A. Dowben, L. Wang, W. N. Mei, and J. A. Kelber, "Electronic structure of a graphene/hexagonal-bn heterostructure grown on ru(0001) by chemical vapor deposition and atomic layer deposition: Extrinsically doped graphene," *Journal of Physics-Condensed Matter*, vol. 22, no. 30, p. 6, 2010.

[134] Y. Shi, C. Hamsen, X. Jia, K. K. Kim, A. Reina, M. Hofmann, A. L. Hsu, K. Zhang, H. Li, Z.-Y. Juang, M. S. Dresselhaus, L.-J. Li, and J. Kong, "Synthesis of few-layer hexagonal boron nitride thin film by chemical vapor deposition," *Nano Letters*, vol. 10, no. 10, pp. 4134–4139, 2010.

[135] A. Ismach, H. Chou, D. A. Ferrer, Y. P. Wu, S. McDonnell, H. C. Floresca, A. Covacevich, C. Pope, R. Piner, M. J. Kim, R. M. Wallace, L. Colombo, and R. S. Ruoff, "Toward the controlled synthesis of hexagonal boron nitride films," *Acs Nano*, vol. 6, no. 7, pp. 6378–6385, 2012.

[136] K. K. Kim, A. Hsu, X. T. Jia, S. M. Kim, Y. S. Shi, M. Hofmann, D. Nezich, J. F. Rodriguez-Nieva, M. Dresselhaus, T. Palacios, and J. Kong, "Synthesis of monolayer hexagonal boron nitride on cu foil using chemical vapor deposition," *Nano Letters*, vol. 12, no. 1, pp. 161–166, 2012.

[137] J. D. Ferguson, A. W. Weimer, and S. M. George, "Atomic layer deposition of boron nitride using sequential exposures of bcl3 and nh3," *Thin Solid Films*, vol. 413, no. 1-2, pp. 16–25, 2002.

[138] J. Olander, L. M. Ottosson, P. Heszler, J. O. Carlsson, and K. M. E. Larsson, "Laser-assisted atomic layer deposition of boron nitride thin films," *Chemical Vapor Deposition*, vol. 11, no. 6-7, pp. 330–337, 2005.

[139] N. R. Glavin, M. L. Jespersen, M. H. Check, J. Hu, A. M. Hilton, T. S. Fisher, and A. A. Voevodin, "Synthesis of few-layer, large area hexagonal-boron nitride by pulsed laser deposition," *Thin Solid Films*, vol. 572, pp. 245–250, 2014.

[140] C. L. Tsai, Y. Kobayashi, T. Akasaka, and M. Kasu, "Molecular beam epitaxial growth of hexagonal boron nitride on ni(1 1 1) substrate," *Journal of Crystal Growth*, vol. 311, no. 10, pp. 3054–3057, 2009.

[141] S. Nakhaie, J. M. Wofford, T. Schumann, U. Jahn, M. Ramsteiner, M. Hanke, J. M. J. Lopes, and H. Riechert, "Synthesis of atomically thin hexagonal boron nitride films on nickel foils by molecular beam epitaxy," *Applied Physics Letters*, vol. 106, no. 21, p. 213 108, 2015.

[142] S. Frueh, R. Kellett, C. Mallery, T. Molter, W. S. Willis, C. Kingondu, and S. L. Suib, "Pyrolytic decomposition of ammonia borane to boron nitride," *Inorganic Chemistry*, vol. 50, no. 3, pp. 783–792, 2011.

[143] M. Wang, M. Kim, D. Odkhuu, N. Park, J. Lee, W.-J. Jang, S.-J. Kahng, R. S. Ruoff, Y. J. Song, and S. Lee, "Catalytic transparency of hexagonal boron nitride on copper for chemical vapor deposition growth of large-area and high-quality graphene," *ACS Nano*, vol. 8, no. 6, pp. 5478–5483, 2014.

[144] J. H. Park, J. C. Park, S. J. Yun, H. Kim, D. H. Luong, S. M. Kim, S. H. Choi, W. Yang, J. Kong, K. K. Kim, and Y. H. Lee, "Large-area monolayer hexagonal boron nitride on pt foil," *Acs Nano*, vol. 8, no. 8, pp. 8520–8528, 2014.

[145] A. Hemmi, C. Bernard, H. Cun, S. Roth, M. Klockner, T. Kalin, M. Weinl, S. Gsell, M. Schreck, J. Osterwalder, and T. Greber, "High quality single atomic layer deposition of hexagonal boron nitride on single crystalline rh(111) four-inch wafers," *Review of Scientific Instruments*, vol. 85, no. 3, p. 4, 2014.

[146] A. Andrieux, N. Dorval, F. Fossard, L. Schue, P. Lavenus, and A. Loiseau, "Cvd synthesis and characterization of hexagonal boron nitride thin films," in *18th International Microscopy Congress*.

[147] N. D. Zhigadlo, "Crystal growth of hexagonal boron nitride (hbn) from mgbn solvent system under high pressure," *Journal of Crystal Growth*, vol. 402, no. Supplement C, pp. 308–311, 2014.

[148] S. Roth, F. Matsui, T. Greber, and J. Osterwalder, "Chemical vapor deposition and characterization of aligned and incommensurate graphene/hexagonal boron nitride heterostack on cu(111)," *Nano Letters*, vol. 13, no. 6, pp. 2668–2675, 2013.

[149] H. Sediri, D. Pierucci, M. Hajlaoui, H. Henck, G. Patriarche, Y. J. Dappe, S. Yuan, B. Toury, R. Belkhou, M. G. Silly, F. Sirotti, M. Boutchich, and A. Ouerghi, "Atomically sharp interface in an h-bn-epitaxial graphene van der waals heterostructure," *Scientific Reports*, vol. 5, p. 16 465, 2015.

[150] G. Liu, E. Deguns, L. Lecordier, G. Sundaram, and J. Becker, "Atomic layer deposition of aln with tris(dimethylamido)aluminum and nh3," *ECS Transactions*, vol. 41, no. 2, pp. 219–225, 2011.

[151] Z. Liu, L. Song, S. Z. Zhao, J. Q. Huang, L. L. Ma, J. N. Zhang, J. Lou, and P. M. Ajayan, "Direct growth of graphene/hexagonal boron nitride stacked layers," *Nano Letters*, vol. 11, no. 5, pp. 2032–2037, 2011.

[152] Y. Miyata, E. Maeda, K. Kamon, R. Kitaura, Y. Sasaki, S. Suzuki, and H. Shinohara, "Fabrication and characterization of graphene/hexagonal boron nitride hybrid sheets," *Applied Physics Express*, vol. 5, no. 8, p. 3, 2012.

[153] Y. Song, C. Zhang, B. Li, D. Jiang, G. Ding, H. Wang, and X. Xie, "Triggering the atomic layers control of hexagonal boron nitride films," *Applied Surface Science*, vol. 313, pp. 647–653, 2014.

[154] R. M. F. Patrick. C. Mende Jun Li, "Growth and characterization of hexagonal boron nitride on graphene on sic(0001)," *Acs Nano*, 2015.

[155] D. P. Gopalan, P. C. Mende, S. C. de la Barrera, S. Dhingra, J. Li, K. Zhang, N. A. Simonson, J. A. Robinson, N. Lu, Q. Wang, M. J. Kim, B. D'Urso, and R. M. Feenstra, "Formation of hexagonal boron nitride on graphene-covered copper surfaces," *arXiv:1509.04531v2*, 2016.

[156] T. Q. P. Vuong, G. Cassabois, P. Valvin, E. Rousseau, A. Summerfield, C. J. Mellor, Y. Cho, T. S. Cheng, J. D. Albar, L. Eaves, C. T. Foxon, P. H. Beton, S. V. Novikov, and B. Gil, "Deep ultraviolet emission in hexagonal boron nitride grown by high-temperature molecular beam epitaxy," *2D Materials*, vol. 4, no. 2, p. 021 023, 2017.

[157] A. R. Jang, S. Hong, C. Hyun, S. I. Yoon, G. Kim, H. Y. Jeong, T. J. Shin, S. O. Park, K. Wong, S. K. Kwak, N. Park, K. Yu, E. Choi, A. Mishchenko, F. Withers, K. S. Novoselov, H. Lim, and H. S. Shin, "Wafer-scale and wrinkle-free epitaxial growth of single-orientated multilayer hexagonal boron nitride on sapphire," *Nano Letters*, vol. 16, no. 5, pp. 3360–3366, 2016.

[158] Y. Zhang, W. Ren, Z. Jiang, S. Yang, W. Jing, P. Shi, X. Wu, and Z.-G. Ye, "Low-temperature remote plasma-enhanced atomic layer deposition of graphene and characterization of its atomic-level structure," *Journal of Materials Chemistry C*, vol. 2, no. 36, pp. 7570–7574, 2014.

[159] A. Valdivia, D. J. Tweet, and J. F. Conley, "Atomic layer deposition of two dimensional mos2 on 150mm substrates," *Journal of Vacuum Science & Technology A: Vacuum, Surfaces, and Films*, vol. 34, no. 2, p. 021 515, 2016.

[160] B. Robert, K. Neal, S. Raj, K. Vasily, and R. Sergei, "Large area growth of layered wse 2 films," *Semiconductor Science and Technology*, vol. 31, no. 9, p. 095 002, 2016.

[161] T. Jurca, M. J. Moody, A. Henning, J. D. Emery, B. Wang, J. M. Tan, T. L. Lohr, L. J. Lauhon, and T. J. Marks, "Low-temperature atomic layer deposition of mos2 films," *Angewandte Chemie International Edition*, vol. 56, no. 18, pp. 4991–4995, 2017.

[162] M. Chubarov, H. Pedersen, H. Hgberg, J. Jensen, and A. Henry, "Growth of high quality epitaxial rhombohedral boron nitride," *Crystal Growth & Design*, vol. 12, no. 6, pp. 3215–3220, 2012.

[163] S. Majety, J. Li, W. P. Zhao, B. Huang, S. H. Wei, J. Y. Lin, and H. X. Jiang, "Hexagonal boron nitride and 6h-sic heterostructures," *Applied Physics Letters*, vol. 102, no. 21, p. 213 505, 2013.

[164] M. Snure, Q. Paduano, and A. Kiefer, "Effect of surface nitridation on the epitaxial growth of few-layer sp(2) bn," *Journal of Crystal Growth*, vol. 436, pp. 16–22, 2016.

[165] A. Mircea, A. Ougazzaden, and R. Mellet, "Very uniform epitaxy," *Progress in Crystal Growth and Characterization of Materials*, vol. 19, no. 1-2, pp. 39–49, 1989.

[166] W. Pan, J. L. Xiao, J. W. Zhu, C. X. Yu, G. Zhang, Z. H. Ni, K. Watanabe, T. Taniguchi, Y. Shi, and X. R. Wang, "Biaxial compressive strain engineering in graphene/boron nitride heterostructures," *Scientific Reports*, vol. 2, p. 6, 2012.

[167] N. Mishra, V. Miseikis, D. Convertino, M. Gemmi, V. Piazza, and C. Coletti, "Rapid and catalyst-free van der waals epitaxy of graphene on hexagonal boron nitride," *Carbon*, vol. 96, pp. 497–502, 2016.

[168] Y. Guo, L. W. Guo, W. Lu, J. Huang, Y. P. Jia, W. Sun, Z. L. Li, and Y. F. Wang, "Influence of defects in sic (0001) on epitaxial graphene," *Chinese Physics B*, vol. 23, no. 8, 2014.

[169] H. Wang, C. Zhao, L. Liu, Z. Xu, J. Wei, W. Wang, X. Bai, and E. Wang, "Towards the controlled cvd growth of graphitic bcn atomic layer films: The key role of bc delivery molecular precursor," *Nano Research*, vol. 9, no. 5, pp. 1221–1235, 2016.

[170] J. D. Emery, V. D. Wheeler, J. E. Johns, M. E. McBriarty, B. Detlefs, M. C. Hersam, D. Kurt Gaskill, and M. J. Bedzyk, "Structural consequences of hydrogen intercalation of epitaxial graphene on sic(0001)," *Applied Physics Letters*, vol. 105, no. 16, p. 161 602, 2014.

[171] I. Caretti and I. Jimenez, "Point defects in hexagonal bn, bc3 and bcxn compounds studied by x-ray absorption near-edge structure," *Journal of Applied Physics*, vol. 110, no. 2, p. 9, 2011.

[172] S. P. Huber, E. Gullikson, R. W. E. van de Kruijs, F. Bijkerk, and D. Prendergast, "Oxygen-stabilized triangular defects in hexagonal boron nitride," *Physical Review B*, vol. 92, no. 24, p. 245 310, 2015.

[173] P. Plochocka, C. Faugeras, M. Orlita, M. L. Sadowski, G. Martinez, M. Potemski, M. O. Goerbig, J. N. Fuchs, C. Berger, and W. A. de Heer, "High-energy limit of massless dirac fermions in multilayer graphene using magneto-optical transmission spectroscopy," *Physical Review Letters*, vol. 100, no. 8, p. 087 401, 2008.

[174] A. A. Baski and H. Fuchs, "Epitaxial growth of silver on mica as studied by afm and stm," *Surface Science*, vol. 313, no. 3, pp. 275–288, 1994.

[175] H. Galinski, T. Ryll, P. Reibisch, L. Schlagenhauf, I. Schenker, and L. J. Gauckler, "Temperature-dependent 2-d to 3-d growth transition of ultra-thin pt films deposited by pld," *Acta Materialia*, vol. 61, no. 9, pp. 3297–3303, 2013.

[176] T. Irie, T. Yasunobu, H. Kashimura, and T. Setoguchi, "Characteristics of the mach disk in the underexpanded jet in which the back pressure continuously changes with time," *Journal of Thermal Science*, vol. 12, no. 2, pp. 132–137, 2003.

[177] K. A. Pacheco, B. A. Ferguson, C. Li, S. John, S. Banerjee, and C. B. Mullins, "Epitaxial silicon growth using supersonic jets of disilane - a model study of energetic jet deposition," *Applied Physics Letters*, vol. 67, no. 20, pp. 2951–2953, 1995.

[178] S. E. Roadman, N. Maity, J. N. Carter, and J. R. Engstrom, "Study of thin film deposition processes employing variable kinetic energy, highly collimated neutral molecular beams," *Journal of Vacuum Science & Technology a-Vacuum Surfaces and Films*, vol. 16, no. 6, pp. 3423–3433, 1998.

[179] D Eres, "Surface chemistry and beam-solid interactions," Pittsburgh, PA (USA); Materials Research Society, Report, 1991.

[180] J. Fernandez de la Mora and J. RosellLlompart, "Aerodynamic focusing of heavy molecules in seeded supersonic jets," *The Journal of Chemical Physics*, vol. 91, no. 4, pp. 2603–2615, 1989.

[181] S. A. Ustin, K. A. Brown, and W. Ho, "An apparatus for supersonic jet epitaxy of thin films," *Review of Scientific Instruments*, vol. 71, no. 3, pp. 1479–1487, 2000.

[182] D. Kelly, R. W. Verhoef, and W. H. Weinberg, "Effect of internal energy on the dissociative chemisorption of oxygen on ir(110)," *Surface Science*, vol. 321, no. 1, pp. L157–L163, 1994.

[183] D. R. Miller, in *Atomic and Molecular Beam Methods*. New York: Oxford University Press, 1988, vol. 2.

[184] S. Zhang, J. Cui, and Y. Aoyagi, "Growth control of gaas using short-pulse supersonic beam epitaxy," *Journal of Crystal Growth*, vol. 164, no. 1, pp. 28–33, 1996.

[185] K. A. Pacheco, B. A. Ferguson, S. Banerjee, and C. B. Mullins, "Surface morphology of homoepitaxial silicon thin films grown using energetic supersonic jets of disilane," *Applied Physics Letters*, vol. 69, no. 8, pp. 1110–1112, 1996.

[186] S. Zhang, J. Cui, A. Tanaka, and Y. Aoyagi, "Shortpulse supersonic nozzle beam epitaxy: A new approach for submonolayer controlled growth," *Applied Physics Letters*, vol. 64, no. 9, pp. 1105–1107, 1994.

[187] J. Cui, S. Zhang, A. Tanaka, and Y. Aoyagi, "Millisecond timeresolved reflectance difference measurements of gaas grown by shortpulse supersonic nozzle beam epitaxy," *Applied Physics Letters*, vol. 64, no. 24, pp. 3285–3287, 1994.

[188] R. Malik and E. Gulari, "Pulsed supersonic jet epitaxy: A nonthermal approach to silicon growth," *Applied Physics Letters*, vol. 68, no. 22, pp. 3156–3158, 1996.

[189] W. Davidor and S. S. Penner, "Shock standoff distances and mach-disk diameters in underexpanded sonic jets," *AIAA Journal*, vol. 9, no. 8, pp. 1651–1653, 1971.

[190] M. M. Orescanin and J. M. Austin, "Exhaust of underexpanded jets from finite reservoirs," *Journal of Propulsion and Power*, vol. 26, no. 4, pp. 744–753, 2010.

[191] D. W. Eastman and L. P. Radtke, "Location of the normal shock wave in the exhaust plume of a jet," *AIAA Journal*, vol. 1, no. 4, pp. 918–919, 1963.

[192] D. Edgington-Mitchell, D. R. Honnery, and J. Soria, "The underexpanded jet mach disk and its associated shear layer," *Physics of Fluids*, vol. 26, no. 9, p. 096 101, 2014.

[193] S. Bernard and P. Miele, "Polymer-derived boron nitride: A review on the chemistry, shaping and ceramic conversion of borazine derivatives," *Materials*, vol. 7, no. 11, p. 7436, 2014.

[194] A. H. White and W. Melville, "The decomposition of ammonia at high temperatures," *Journal of the American Chemical Society*, vol. 27, no. 4, pp. 373–386, 1905.

[195] T. D. Moustakas, T. Lei, and R. J. Molnar, "Growth of gan by ecr-assisted mbe," *Physica B: Condensed Matter*, vol. 185, no. 1, pp. 36–49, 1993.

[196] R. J. Molnar, R. Singh, and T. D. Moustakas, "Operation of a compact electron cyclotron resonance source for the growth of gallium nitride by molecular beam epitaxy (ecr-mbe)," *Journal of Electronic Materials*, vol. 24, no. 4, pp. 275–281, 1995.

[197] J. E. Pollard, "Radiofrequency discharge source for beams of atomic nitrogen and oxygen," *Review of Scientific Instruments*, vol. 63, no. 2, pp. 1771–1776, 1992.

[198] D. C. Jordan, C. T. Burns, and R. B. Doak, "Corona discharge supersonic free-jet for iiiv nitride growth via ał3u+ metastable nitrogen molecules," *Journal of Applied Physics*, vol. 89, no. 2, pp. 883–892, 2000.

[199] G. H. Gilmer and C. Roland, "Simulations of crystal growth: Effects of atomic beam energy," *Applied Physics Letters*, vol. 65, no. 7, pp. 824–826, 1994.

[200] M. Koster and H. M. Urbassek, "Damage production in a-si under low-energy self-atom bombardment," *Journal of Applied Physics*, vol. 90, no. 2, pp. 689–695, 2001.

[201] C. D. Rakopoulos, E. G. Giakoumis, and D. C. Rakopoulos, "Study of the short-term cylinder wall temperature oscillations during transient operation of a turbo-charged diesel engine with various insulation schemes," *International Journal of Engine Research*, vol. 9, no. 3, pp. 177–193, 2008.

[202] K. Kang, S. Xie, L. Huang, Y. Han, P. Y. Huang, K. F. Mak, C.-J. Kim, D. Muller, and J. Park, "High-mobility three-atom-thick semiconducting films with wafer-scale homogeneity," *Nature*, vol. 520, no. 7549, pp. 656–660, 2015.

[203] M. Marx, S. Nordmann, J. Knoch, C. Franzen, C. Stampfer, D. Andrzejewski, T. Kmmell, G. Bacher, M. Heuken, H. Kalisch, and A. Vescan, "Large-area mos2 deposition via movpe," *Journal of Crystal Growth*, vol. 464, pp. 100–104, 2017.

[204] L. Wang, I. Meric, P. Y. Huang, Q. Gao, Y. Gao, H. Tran, T. Taniguchi, K. Watanabe, L. M. Campos, D. A. Muller, J. Guo, P. Kim, J. Hone, K. L. Shepard, and C. R. Dean, "One-dimensional electrical contact to a two-dimensional material," *Science*, vol. 342, no. 6158, pp. 614–617, 2013.

VITA

Jamey Gigliotti began his tenure at Georgia Tech studying the growth of nanoscale piezoelectric films before joining the Epitaxial Graphene Lab where he worked in close collaboration with researchers at Georgia Tech Lorraine in Metz, France. Before coming to Georgia Tech, Jamey completed his undergraduate education at Penn State University, a few hours from his hometown of Harrisburg, Pa. While at Penn State, he worked on piezoelectric micromachined ultrasonic transducers for medical imaging and sonotweezing applications. This research took him to Germany to work with ultrasound simulation experts. While the focus of his research has changed several times, a unifying theme has been the deposition and characterization of nanoscale material systems. He plans to continue along this theme, but with a new focus in the semiconductor industry after graduation.

Outside of the lab, Jamey was avid skier, fitness enthusiast, amateur photographer, and abstract painter. He was a co-leader for November Project Atlanta, a grassroots, free community fitness movement.